Cable Trays and EMC: Modelling and Measurement

Nolan Wade Ebertsohn

Supervisors:

Dr. R.H. Geschke

Prof. H.C. Reader

This thesis presented in partial fulfilment for the requirements of the degree of Master of Engineering at the University of Stellenbosch.

December 2005

Declaration

I, the undersigned, hereby declare that the work contained in this thesis is my own original work, unless stated otherwise, and that it has not previously in its entirety or in part been submitted at any university for a degree.

N.W. Ebertsohn:

Abstract

Common mode currents are a major source of interference in electrical and electronic systems. A universal solution to counteract common mode interference is to introduce an electromagnetic shield with known characteristics. Cable trays are often used to shield cables from unwanted electromagnetic interference (*EMI*) and its shielding characteristics are defined in terms of its transfer impedance. This thesis pursues the modelling and measurement of the transfer impedance and mutual inductance of non-magnetic cable trays. Theoretical analysis is firstly employed by means of Maxwell's equations after which method of moments (*MoM*) simulations are performed in order to determine the transfer impedance and mutual inductance within the interior region of a cable tray. The results obtained through simulation are then validated with measurements conducted with an automatic network analyser (*ANA*). The computational and measured data are in good agreement and the developed model can be used to predict the transfer impedance in the cross-section of non-magnetic cable trays.

Opsomming

Gemenemodus strome is 'n bron van interferensie in elektriese en elektroniese stelsels. 'n Universele oplossing om hierdie gemenemodus interferensie teen werk is om 'n elektromagnetiese skerm met bekende eienskappe te implementeer. Geleier leikanale word dikwels gebruik om kabels teen elektromagnetiese interferensie te beskerm en die afskermings eienskappe word in terme van die kanaal se oordragsimpedansie gedefinieer. Hierdie tesis ondersoek die modelering en meting van die wedersydse induktansie en oordragsimpedansie van nie-magnetiese geleier leikanale. 'n Teoretiese analise word eers uitgevoer deur middel van Maxwell se vergelykings waarna metode van momente (*MvM*) simulasies uitgevoer word om die oordragsimpedansie en wedersydse induktansie in die interne gebied van 'n leikanaal te bepaal. Die resultate verkry deur simulasie word dan bevestig deur meting wat uitgevoer word met behulp van 'n automatiese netwerk analiseerder (*ANA*). Die numeriese en gemete data stem goed ooreen en die ontwikkelde model kan deurgaans gebruik word om die oordragsimpedansie in die deursnit area van nie-magnetiese geleier leikanale te voorspel.

Acknowledgements

Special thanks must be given to:

God, my family and friends for love, patience, and support over the course of my academic career.

Prof. Howard Reader and Dr. Riana Geschke for your guidance and passion, your leadership is inspirational.

Special thanks must also go to the staff at Central Electronic Services for their work of superb quality and Martin Siebers who is always eager to assist in any situation. Danie le Roux of EMSS is also thanked for his input and advice with regard to *FEKO*®. Finally, I would like to thank ESKOM and the NRF for financial support over the past two years.

Table of Contents

List of Figures

List of Tables

List of Abbreviations and Symbols

μ_r	*Relative Permeability*
μ_0	*Permeability of free space* = $4\pi \times 10^{-7}$ $[H/m]$
μ	$\mu_r\ \mu_0$
ε_r	*Relative Permittivity*
ε_0	*Permittivity of free space* = 8.85415×10^{-12} $[F/m]$
ε	$\varepsilon_r\ \varepsilon_0$ *[F/m]*
λ	*Wavelength [m]*
σ	*Conductivity [S/m]*
π	*pi* = $\frac{22}{7}$ *[ratio of a circles circumference to its radius]*
ω	*Angular frequency* = $2\pi f$ *[radians]*
AC	*Alternating Current [A]*
ANA	*Automatic Network Analyzer*
B	*Magnetic Flux Density [Tesla]*
BEM	*Boundary Element Method*
BW	*Bandwidth [Hz]*
C	*Capacitance [H]*
c	*Speed of light = 2.99 x 10^8 m/s [this value is an approximation]*
CEM	*Computational Electromagnetics*
CES	*Central Electronic Services*
CM	*Common Mode*
CUT	*Circuit under test*
D	*Distance [m]*
DC	*Direct Current [A]*
DM	*Differential Mode*
DUT	*Device Under Test*
E	*Electric Field [V/m]*
EM	*Electromagnetic*
EMC	*Electromagnetic Compatibility*
EMI	*Electromagnetic Interference*

f	*Frequency [Hz]*
GS	*Grounding Structure*
H	*Magnetic Field Strength [A/m]*
HF	*High Frequency*
I	*Current [A]*
I_{CM}	*Common Mode Current [A]*
I_{DM}	*Differential Mode Current [A]*
IEC	*International Electrotechnical Commission*
IF	*Intermediate Frequency*
J	*Current Density[A/m^2]*
L	*Inductance [H]*
l	*Length [m]*
LF	*Low Frequency*
ln	*Natural Logarithm (base e)*
Log_{10}	*Logarithm (base 10)*
M	*Mutual Inductance [nH/m]*
m	*milli (10^{-3})*
MMCX	*MicroMiniature Connector*
MoM	*Method of Moments*
n	*nano (10^{-9})*
PEC	*Parallel Earth Conductor*
R	*Resistance [ohm]*
r	*Radius*
S	*Bounded Surface*
SE	*Shielding Effectiveness [dB]*
SMA	*Standard Military Adapter*
TL	*Transmission Line*
V	*Voltage [V]*
V_{DM}	*Differential Mode Voltage [V]*
Z	*Impedance [ohm]*
Z_t	*Transfer Impedance [ohm/m]*

Chapter 1
Introduction

1.1 Background

Electromagnetic compatibility (*EMC*) is the branch of science and engineering concerned with the proper functioning and co-existence of electrical and electronic devices, equipment, or systems in all electromagnetic (*EM*) environments. The official *IEC* (*International Electrotechnical Commission*) definition of *EMC* is [*IEC* 50(161-01-07)]:

> *The ability of a device, equipment, or system to function satisfactory in its electromagnetic environment without introducing intolerable electromagnetic disturbances in that environment.*

Due to advances in communication and digital technology in recent years, the co-existence of sub-systems has become more prevalent. Components being utilized with faster switching times increases the risk of surrounding equipment and cables being subject to unwanted electromagnetic interference (*EMI*). Power cables, control cables and sensor cables currently all form part of modern-day electronic systems. Signals, analog and digital, are conveyed from one point to another with shielded or non-shielded conductors. Interference from external sources can induce unwanted currents in these conductors, which result in unwanted voltages at their terminals.

Several techniques exist to minimize interference created by unwanted electromagnetic (*EM*) sources and ensure *EMC* in its immediate environment. One option is to use a shield with known characteristics. Magnetic and non-magnetic metallic shields are used to shield sensitive systems or cables. A simple example of shielding is the co-axial cable. The outer, braided or solid, conductor shields the inner conductor and its shielding property is often referred to as transfer impedance. *U*-shaped cable trays or conduits are also commonly used to protect cable from unwanted interference and are often referred to as parallel-earthing conductors (*PEC*) or grounding structures (*GS*) [1]. Metallic spray paint

can also be used to cover non-metallic surfaces of boxes to shield the contents from *EMI* [4].

Van Helvoort [1] and van Deursen [2] describe *U, L* and *H*-shaped cable trays. The transfer impedance is determined mathematically with Maxwell's equations as well as conformal transformations proposed by Darwin [2]. The boundary element method (*BEM*) is implemented by [1] and [2] to determine numerically the transfer impedance of these topologies. Measurements conducted by [1] and [2] utilise a sinusoidal signal generator to inject a *CM* current (400 mA peak-peak), at *5 Hz – 100 kHz.* A lock-in amplifier, placed in an *EMC* cabinet, was used to measure the *DM* interference voltage. Above *100 kHz,* a network analyser was used to measure the *DM* voltage. These measurements were conducted manually at several frequency points and an automated measurement system and *S*-parameter set was not available at the time [1]. No detailed or graphic description in terms of the mutual inductance in the interior region of a cable tray is presented by [1] or [2].

1.2 Summary

The main objective of this thesis is to model and measure the transfer impedance of non-magnetic cable trays with different height-to-width ratios. The first step in our approach is to gain a thorough understanding of different circuit configurations from an *EMC* perspective. This enables us to understand how it relates to different shielding mechanisms and how it can be applied to reduce *EMI.* The next step is to describe analytically the transfer impedance of non-magnetic cable trays by implementing Maxwell's equations, after which a suitable numerical simulation model is developed with Method of Moments (*MoM*) code with *FEKO*®.

The computational electromagnetics (*CEM*) model should enable us define a two-port network and inject a common mode current into a cable tray in order to acquire the magnetic fields and *S*-parameters. Lines of constant mutual inductance can be obtained from the calculated magnetic field. We then go on to develop a measurement setup in order to measure the transfer impedance with an Automatic Network Analyser (*ANA*). The

measured data is then compared to simulations. The final objective is to suggest effective installation guidelines for cable trays according to the preceding details.

1.3 Thesis Layout

The next chapter presents background knowledge and differentiates between different coupling mechanisms and techniques to minimize or avoid coupling. The transfer impedance concept is introduced and understanding is gained in how this relates to mutual inductance, common mode currents, the skin effect, material properties, and the geometry of three-wire systems. Chapter 3 introduces the theoretical equations for non-magnetic cable trays derived with Maxwell's equations. Special attention is given to the direct current (*DC*) and high frequency (*HF*) analysis of the transfer impedance and mutual inductance. These expressions are used for comparison against the measured and numerically calculated mutual inductance to validate the accuracy of the engineering expressions.

Chapter 4 describes the development of a *CEM* simulation model with *FEKO*®, which makes use of the *MoM*. The transfer impedance is calculated by means of *S*-parameters, and the interior magnetic fields of cable trays with different height-to-width ratios (*h/w = 1/2, 1, 3/2, 2*) are obtained in order to derive lines of constant mutual inductance.

Chapter 5 presents the measurement configuration and setup for the validation of the simulation results. *EMC* metrology techniques are highlighted here. Measured data is then compared to its simulated *CEM* counterpart and the results discussed appropriately.

In chapter 6, installation guidelines for cable trays are suggested for optimal shielding. General rules regarding cable trays, their installation and placement of cables within trays are discussed. Finally, chapter 7 contains the conclusions, of work done in this thesis, and recommendations for future work.

Chapter 2

Cable Trays, EMC and Transfer Impedance

2.1 Introduction

A cable tray is used to shield cables from *EMI* generated by unwanted common mode *CM* currents and is described as a grounding structure by [1], with the following definition for grounding:

> *Grounding provides a set of interconnected paths for currents, designed to have low transfer impedance, in order to keep the interference voltages at the terminals of sensitive equipment low.*

The focus of this thesis is to investigate the transfer impedance of non-magnetic cable trays as well as the *B*-field in the interior region. The shielding efficiency of a cable tray is defined in terms of its transfer impedance, which relates the differential mode (*DM*) interference voltage to the unwanted interference *CM* current. Transfer impedance is defined as:

$$Z_t / l = \left. \frac{V_{DM}}{I_{CM}} \right|_{I_{DM}=0} \quad [\Omega / m] \tag{2.1}$$

where l is the length of the DM circuit. The *CM* current gives rise to a *B*-field, which couples with the closed surface between the tray and conductor, along its length l, resulting in the *DM* voltage. One would then consider the mutual inductance between such a conductor and the tray to be important. Additionally, we are interested in the physical and material properties of a cable tray that can be changed in order to reduce the mutual inductance and consequently the transfer impedance. The physical or geometrical property that can be changed is the height-to-width ratio, which relates the height of the sidewall to the width of the floor, if the total cross-sectional length is kept constant. Material properties that can be altered include the relative permeability and conductivity. Because

we are studying non-magnetic cable trays, the relative permeability is limited to $\mu_r = 1$. The only material property that can be altered is the conductivity. The conductivity together with the thickness of the metal will determine the frequency response of the tray, which is directly related to the skin depth and skin effect. In order to gain understanding on how a cable tray relates to *EMC* and how it reduces *EMI* the following sections introduce different coupling mechanisms and ways to reduce them. Furthermore, aspects like the skin effect and the geometry, circuit configurations; transfer impedance and mutual inductance of three-wire systems are discussed to exemplify how it relates to cable trays.

In all the discussions to follow, we assume that the frequency of the interference is low. In other words we follow a quasi-static approach that implies that the wavelength of the disturbing current signal, $\lambda = c / f$, is such that $\lambda >> d$, where d is a typical dimension of the overall source-victim configuration. If this approach is not followed, we have to make use of transmission line (*TL*) models. The quasi-static approach would also eliminate wave effects and resonances during computational modelling and measurement.

2.2 Electric Field Coupling

From a two-port network approach, Figure 2.1(a) depicts a source-victim coupling configuration. In this specific configuration, the coupling is primarily due to the *E*-field. The *EMC* source voltage V_1 can induce large charge densities on the coupling elements. This is because there is no low impedance or closed path (loop) from one conductor to the other. The resulting current I_1 and its magnetic field will be small. However, both *E* and *B* fields exist, and both contribute to the total field coupling with the *E*-field being the predominant factor. The two-port equivalent circuit model for this coupling is depicted in Figure 2.1(b). In this circuit, C_1 and C_2 represent the self-capacitances of the conductors responsible for coupling at ports 1 and 2.

The capacitance C_0 on the other hand, represents the mutual capacitance between the two circuits and is assumed much larger than C_1 and C_2. Stray and mutual inductances exist, but these are generally negligible in this case as the capacitances are the dominant parameters associated with electric field coupling. A grounded metallic barrier of any kind or metal constitutes an efficient way of reducing C_0 between the source and the victim

circuits [4]. The main goal of the barrier is to reduce the mutual capacitance C_0 between the two circuits. Charges terminate on the barrier forming a low impedance path.

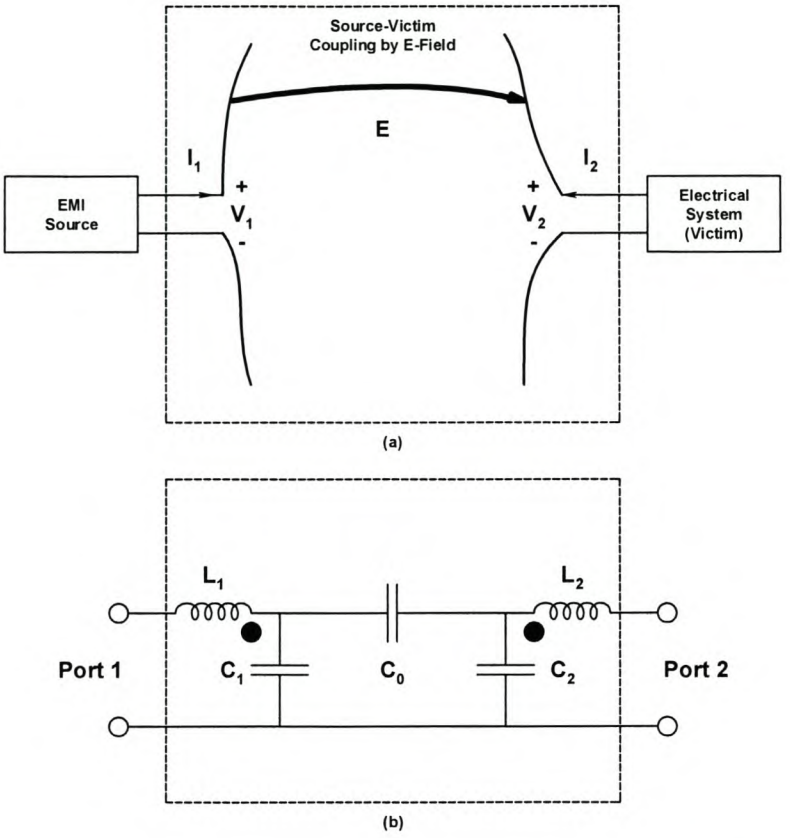

Figure 2.1: *Low-frequency E-field coupling of source and victim circuits: (a) circuit geometry; (b) two-port representation of E-field coupling (after [4]).*

2.3 Magnetic Field Coupling

As an example of coupling that is due primarily to the *B*-field, Figure 2.2(a) shows an *EMI* source and victim, both represented by single port equivalent circuits. The portions of the circuits responsible for the coupling appear as two loops. The source within the *EMI* enclosure induces a current I_1 in the exposed circuit loop shown in Figure 2.2(a).

This current creates a *B*-field that links the pickup loop in the victim circuit. If there is a time variation of this *B*-field, by Lenz's law a resulting voltage is induced in the pickup loop. Coupling between the source and victim circuit, is known as *inductive coupling* and

leads to induced voltages within the victim's circuitry. Again, both E and B fields exist, and both contribute to the total field coupling with the B-field being the predominant factor the E-field contribution negligible. This coupling can be represented by a two-port network of exposed loops as shown in Figure 2.2(b).

The exposed circuit at port 1 (the *EMI* source) has a self-inductance L_1 and a parasitic capacitance C_1.

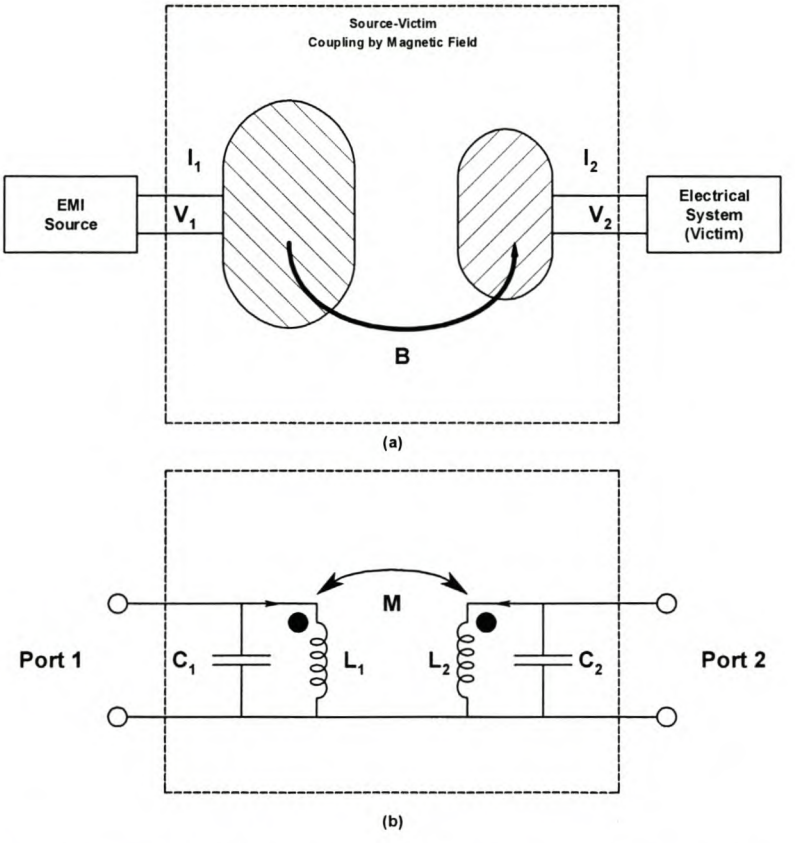

Figure 2.2: *Low-frequency B-field coupling of source and victim circuits: (a) circuit geometry (b) two-port representation of B- field coupling (after [4]).*

The exposed circuit at the victim has similar parameters, L_2 and C_2. The B-field linking the two circuits is represented by the mutual inductance, M, and the coupling capacitance between the two circuits C_0 is negligible. All of these parameters are dependent on the geometry and environment surrounding the circuits and are typically found by measurements or by computational models. For low frequencies, the effects of the

parasitic capacitances C_1 and C_2 are usually negligible [4]. Cable trays are used to minimize *EMI* generated through inductive coupling by reducing the mutual inductance *M*.

2.3.1 Specific measures to reduce magnetic field coupling

Protecting a circuit against the effects of magnetic (inductive) coupling is more challenging than for electric (capacitive) coupling. Magnetic field shielding is frequency and material property dependent [5]. An efficient approach to reduce conducted *EMI* is by minimizing the mutual inductance *M* of the source and victim circuits. For the simplified two-wire line configuration in Figure 2.3, the victim wire can be repositioned closer to the conducting ground. By doing so, the area of the victim loop is reduced and consequently the mutual inductance and induced voltage.

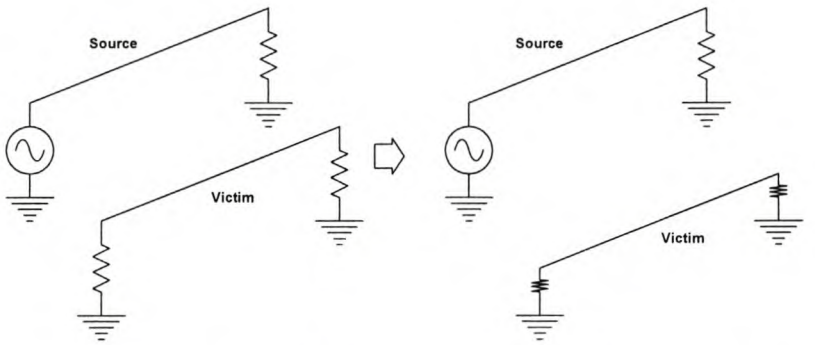

Figure 2.3: *Simplified two-wire line circuit (after [4]).*

Alternatively, it is possible to position the victim circuit farther away to reduce the exposure to the *B*-field created by the source circuit. Either or both techniques can reduce the magnetic field coupling in a cost effective manner. This technique often employs the use of grounding structures (cable trays) in order to minimize the surface area of closed loops exposed to *EM* fields.

2.4 Shielding

Electromagnetic shielding is a technique that reduces or prevents the coupling of unwanted electromagnetic energy into equipment and so enabling it to operate compatibly in its *EM* environment. *EM* shielding is effective in varying degrees over a large part of the *EM* spectrum, from *DC* to microwave frequencies and is accomplished by placing a magnetic

or non-magnetic metallic barrier in the path of *EM* waves between the culprit emitter (source) and receptor (victim).

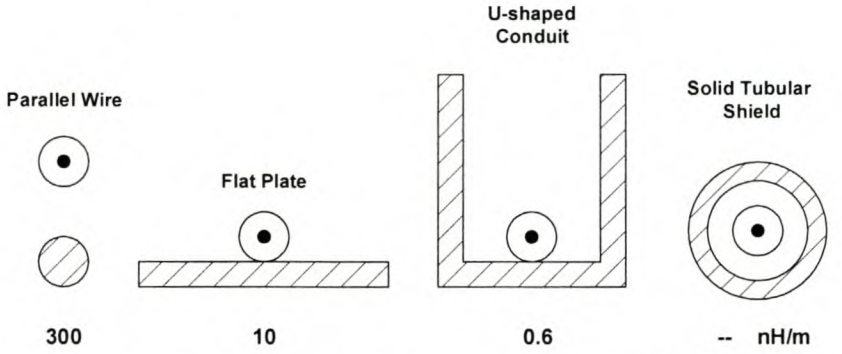

Figure 2.4: *Cross-sectional view of four commonly used PEC's (after [6]).*

The shielding technique used depends on the type of *EM* field to which the victim circuit is exposed. Van Helvoort [1], [2], [3] describes different conduit configurations named parallel earthing conductors (*PEC's*), which can be used as shields for magnetic field shielding. Figure 2.4 illustrates four different topologies that can be used, with the mutual inductance indicated accordingly for conductors at the relevant positions. The solid tubular shield offers better shielding, but it is tedious and difficult to install cables in these shields. From a practical perspective, the better alternative is the *U*-shaped conduit or cable tray.

2.4.1 Magnetic field shielding

Magnetic field shielding refers to the shielding of near-field *B*-fields [5]. For a more in-depth description of near and far fields, as well as plane waves, refer to [4]. An important point to remember is that near-field *B*-fields are not plane waves and that their field distribution is typically complex and source dependent [5]. The shielding of magnetic fields at low frequencies is normally difficult and expensive because of the field penetration depth. Factors that primarily influence the shielding capability of a magnetic shield include:

- Frequency of the disturbance signal(*CM* current in our case)
- Metal thickness
- Metal permeability
- Metallic properties
- Shape and geometry of the shield

The material properties all influence the skin depth and consequently the *SE* of magnetic shields. The most important phenomenon that plays a role in magnetic field shielding is the skin effect. The following section provides an overview of the skin effect and skin-depth. Moreover, it explains how this phenomenon establishes eddy current shielding in order to protect wires or circuits from inductive coupling.

2.5 Shielding of time-varying magnetic fields

2.5.1 Eddy Currents

Eddy currents result from time varying magnetic fields inside a conductor. These currents are not present for *DC* fields or currents. When the term eddy current is used, it is assumed that the magnetic field that induces these currents is from an external source. In theory, the eddy currents can be determined through one of Maxwell's equations, referred to as Faraday's law [5]:

$$\nabla \times \boldsymbol{E} = -\frac{d\boldsymbol{B}}{dt} \tag{2.2}$$

where $\boldsymbol{E}$ is the E-field and $\boldsymbol{B}$ the magnetic flux density. A "first-order" explanation of this equation is that a time-varying *B*-field produces a time-varying *E*-field. This time-varying electric field produces a current, which is a function of the medium's conductivity. The current density, $\boldsymbol{J}$, is related to the electric field via the conductivity, σ as;

$$\boldsymbol{J} = \sigma \boldsymbol{E} \tag{2.3}$$

The skin effect, covered shortly, is described as the total sum of interaction between the current in a conductor and its self-induced eddy currents. This interaction is summarized by [5] as follows:

1. A time varying current in the conductor induces a time-varying *B*-field in the conductor itself.
2. This time-varying *B*-field produces a time-varying *E*-field in the conductor, and
3. The time-varying *E*-field produces a time varying current in the conductor.

This time-varying current, although self-induced, is an eddy current. This eddy current generates a *B*-field that then produces a counter *B*-field and counter current. This sequence continues until a steady-state condition is reached. The summation of the applied current and all of the induced currents results in a non-uniform distribution of the current along the cross-section of the conductor. As the frequency of the current increases, the current spreads toward the skin, or surface of the conductor. The depth of the penetration of the current into the conductor is related to the skin effect and skin depth of the conductor.

2.5.2 The skin effect and skin depth

When a direct current is carried in a conducting wire, the charges move uniformly over the entire cross-section of the conductor. If the amplitude of this current varies over time, the charges are forced out toward the surface of the conductor, as depicted in Figure 2.5.

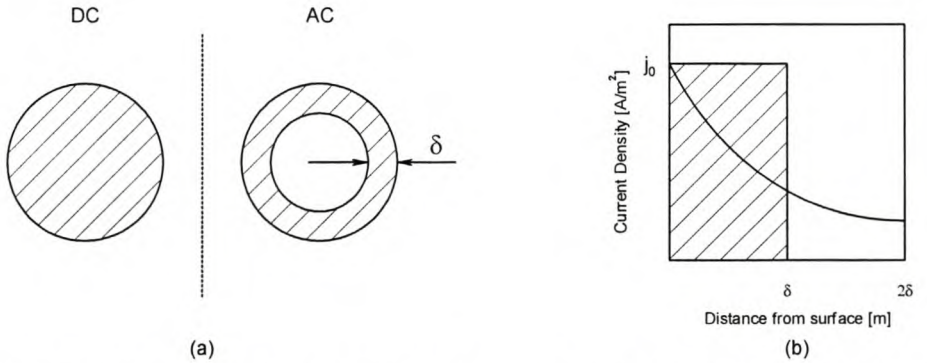

Figure 2.5: *(a) Cross-sectional view of a cylindrical conductor at DC and HF to highlight the skin depth and skin effect (b) Internal current density in a plate.*

This phenomenon, which is called current displacement or the skin effect, will become more evident if the frequency increases. Skin depth is given by [7] as:

$$\delta = \sqrt{\frac{1}{\pi f \mu_r \mu_0 \sigma}} \quad [\text{m}] \tag{2.4}$$

where:

$\mu_0 = 4\pi \times 10^{-7}$ *[H/m]* , σ *(conductivity)[S/m]*, f *(frequency)[Hz]* and $\mu_r = 1$*(relative permeability)*

The internal impedance of a round conductor given by [1] is:

$$Z_w = \begin{cases} R_0 & \text{for } r < \delta \\ R_0(1+j)(\frac{r_w}{2\delta}+\frac{1}{4}) & \text{for } r > \delta \end{cases} \quad (2.5)$$

Where $R_0 = \frac{1}{\pi r_w^2 \sigma}$ is the *DC* resistance per unit length, r_w the radius and δ the skin depth.

The skin effect consequently causes the effective resistance of a conductor to increase with an increase in frequency of the current, as seen in equation 2.5.

Even at frequencies as low as *50* or *60 Hz*, this effect can play an important role in engineering. Power distributors, for example, can reduce the weight and cost of power transmission lines by utilizing tubular-shaped conductors without significantly impairing the resistance of the lines, since most of the current is carried close to the outer surface. The skin effect can also be applied to conductors with a non-cylindrical shape, for example a metal plate. For a metal plate, the induced current density decreases exponentially inward from the surface as [4]:

$$J(x) = J_0 e^{-x/\delta} \quad [\text{A/m}^2] \quad (2.6)$$

where δ is the skin depth of the material given by equation 2.4.

Figure 2.5(b) illustrates the behaviour of the current density. Under many circumstances, it is useful to approximate the exponential distribution with a constant current density, extending down to the depth δ, as shown by the shaded rectangle in Figure 2.5(b). In this manner, the total current in the conductor is the same and only the current distribution is changed.

It also becomes clear that the skin depth is less in materials having a higher conductivity and permeability. For planar shields that are many skin depths thick, the thickness expressed in the number of skin depths gives an indication of the shielding aptitude of the material, due to the exponentially decreasing current density. Moreover, the shape of the shield can have an effect on the current distribution; so that the simple exponential form is not always appropriate neither accurate [4]. It would therefore be difficult to predict the current distribution in a cable tray and one would need to perform simulations or relative

measurements in order to measure the current distribution. A plot of the skin depth for different materials is presented in Figure 2.6. Values of the skin depth for some materials relative to copper are given in appendix A.

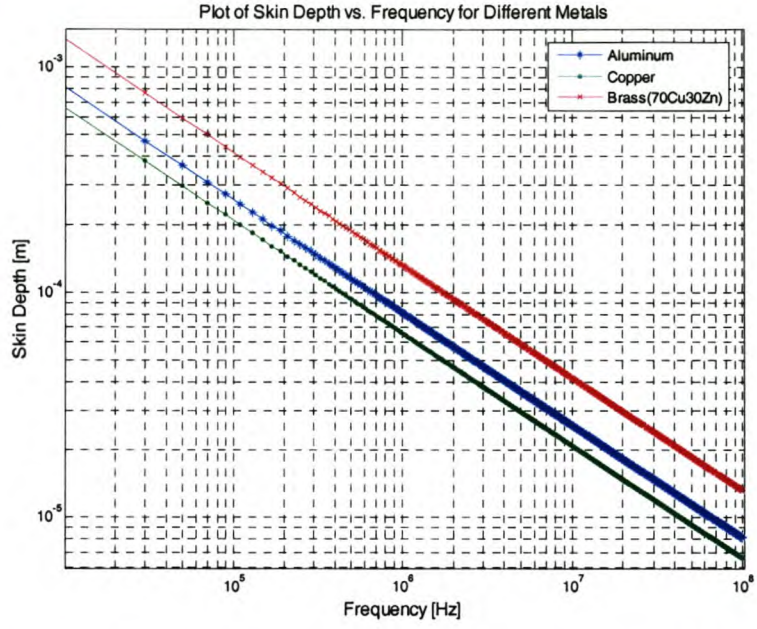

Figure 2.6: *Skin depth as a function of frequency for various metals that could be used as magnetic shields.*

The main purpose of a cable tray is to shield cables in the interior region from *B*-fields generated by a *CM* current flowing through the tray. We then expect the current to flow predominantly on the outer surface of the tray. However, at lower frequencies the current may be homogenously spread through the cross-section resulting in equal values for the *B*-fields interiorly and exteriorly. It is therefore important to keep the skin effect in mind, as it would influence the cross over frequency between *DC* and *HF*. If the crossover frequency is not adequate, the material properties can be changed to suit the shielding specifications.

2.6 The Transfer impedance concept

Transfer impedance (discussed early) Z_t is defined as the ratio of the differential mode voltage and a disturbance current causing it [1]. Z_t can be experimentally determined if a common mode current is injected and the resulting differential mode voltage measured. Values of Z_t depend on the three-dimensional geometry of both the injection and *DM* circuits.

2.6.1 Signal connections

Amperes law states that signal currents have to flow in closed loops. In Figure 2.7(a) a voltage source V_S is connected to a load R_L via a single signal lead (1). The ground lead (g), always present in some form or another, closes this loop. However, the area of this loop is unknown and may be large. Thus, even a small time-varying magnetic field can induce a large disturbance voltage across the load. One way of solving this problem is to introduce a second lead (2). A cable tray could represent this lead and would reduce the area of the original loop as depicted in Figure 2.7(b). The result of this procedure produces a second loop, closed by the ground conductor, which is often referred to as the *CM* loop.

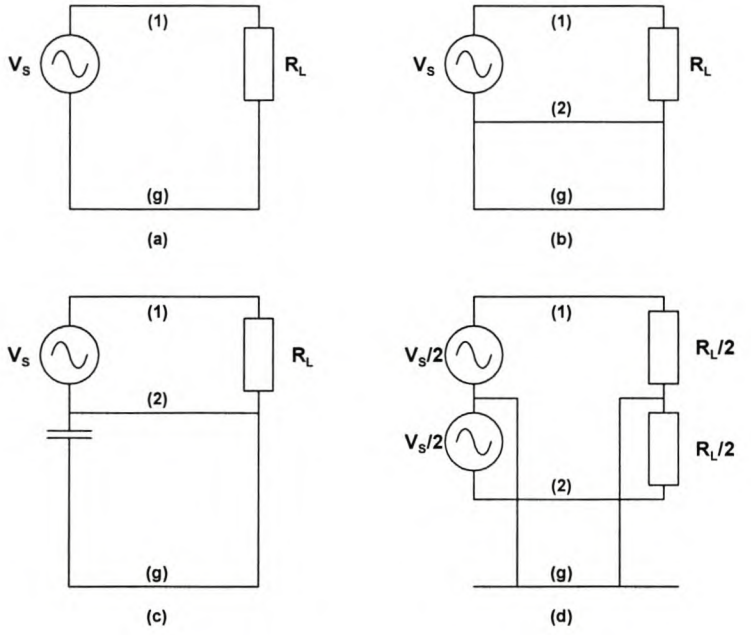

Figure 2.7: *Three-conductor topology for signal transport (after [1]).*

It can be attempted to open the *CM* loop (regulations often prescribe at least one connection to safety ground). If the loop is opened, large voltages can be induced over the interruptions. This can result in flashovers in extreme cases, which causes additional disturbances and a closing of the loop.

At high frequencies, parasitic capacitances close the loop as in Figure 2.7(c). These capacitances may resonate with the self-inductance of the *CM* loop at certain frequencies,

which result in large *CM* currents inducing large *DM* voltages over the terminals of the load. Figure 2.7(d) depicts a balanced configuration considering the ground conductor, whereas Figure 2.7(b) contains the unbalanced configuration. Figure 2.7(b) will form the basis of this thesis and all circuits and assumptions are made based on this circuit configuration.

2.6.2 Topology

The more general case of Figure 2.7 is illustrated in Figure 2.8 where the source and load are replaced by black boxes. Signal flow between the two black boxes is established by the three conductors. Figure 2.8 is valid for balanced and unbalanced signals. If all currents between the two black boxes flow via two signal leads (1) and (2) and one ground lead (g), the following holds:

$$i_1 + i_2 + i_g = 0 \tag{2.7}$$

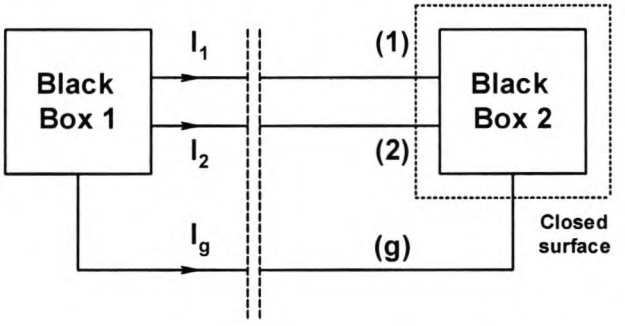

Figure 2.8: *Three-conductor topology for signal transport (after [1]).*

This is a direct consequence of the continuity equation for currents, applied to the closed surface in Figure 2.8. The continuity equation can be derived form Maxwell's equations and is the foundation of Kirchhoff's current law. From an *EMC* perspective, this is important, as it is desired to identify current loops. In general, for an ***n***-conductor system $(n - 1)$ current loops can be identified. In the case of the three-conductor topology, there are two independent current loops. It is also important to define how I_{CM} flows over leads (1) and (2). The second loop, or *DM* loop, in the three-conductor system determines

whether the system is balanced or unbalanced. The next section explains how the geometry of a three-wire system can influence the transfer impedance.

2.6.3 Geometrical properties

To determine a mathematical relationship between the *CM* current and transfer impedance the geometrical relationship between the three conductors must be carefully investigated.

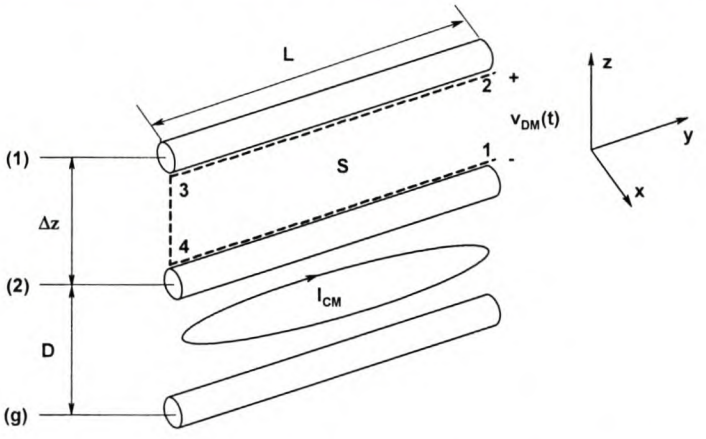

Figure 2.9: *Illustration of the coupling mechanism between differential mode voltage and common mode current. I_{CM} causes an electric field along path 1-4 and a magnetic flux threading loop 1-2-3-4 (after [1]).*

Two loops exist in Figure 2.9, and one would consider the mutual inductance *M* between these two loops important, as it would give an indication of the coupling between them. The mutual inductance will mainly be a function of the geometrical orientation of the loops in relation to each other. The magnetic field created by the *CM* current in Figure 2.9 gives rise to a magnetic field that is mainly responsible for the *DM* voltage $v_{dm}(t)$. From Figure 2.9 $v_{dm}(t)$ is the line integral of the Electric field $\boldsymbol{E}$ along the direct path between point 2 (positive) and 1 (negative) and is given by [1] as:

$$v_{dm} = -\int_1^2 \boldsymbol{E} \cdot d\boldsymbol{l} \qquad = \mu_0 \int_S \frac{d\boldsymbol{H}}{dt} \cdot d\mathbf{a} \; + \; \int_4^1 \boldsymbol{E} \cdot d\boldsymbol{l} \tag{2.8}$$

The first term in equation (2.8) is due to the external magnetic field coupling with loop *1-2-3-4*, the second term originates from the fact that conductor (*2*) has finite conductivity. Therefore, a potential difference will exist between points *1-4* along the surface of the

dotted line of conductor (*2*) as depicted in Figure 2.9. ***S*** is the surface enclosed by loop *1-2-3-4*, ***H*** is the magnetic field strength and $\mu_0 = 4\pi \times 10^{-7}$ H/m, the permeability of a vacuum. For linear systems, the transfer impedance $Z_t(\omega)$ can be defined as the ratio of $V_{DM}(\omega)$ and $I_{CM}(\omega)$ per unit length of the conductor. $V_{DM}(\omega)$ and $I_{CM}(\omega)$ are the Fourier transforms of $v_{dm}(t)$ and $i_{cm}(t)$ respectively. Keeping this in mind Z_t becomes:

$$Z_t / l = \frac{V_{DM}}{I_{CM}} = \frac{\left[\frac{\boldsymbol{J}_y}{\sigma} + j\omega\mu_0 \int_1^2 \boldsymbol{H}_x dz\right]}{I_{CM}} = \frac{\boldsymbol{E}_y}{I_{CM}} + \frac{j\omega\mu_0 \int_1^2 \boldsymbol{H}_x dz}{I_{CM}} \quad [\Omega/\text{m}] \tag{2.9}$$

where σ = *conductivity of conductor* (2), and J_z = Surface current along the dotted line of conductor (2).

Equation 2.9 can be rewritten as the combination of impedance $Z_S = \frac{\boldsymbol{E}_y}{I_{CM}}$, which is related to the local internal field in the metal, and a mutual inductance M, per unit length, related to the outside magnetic field. Equation (2.9) reduces to:

$$Z_t / l = Z_{S,E-field} + j\omega M_{B-field} \qquad [\Omega/m] \tag{2.10}$$

From equation 2.10, it becomes clear that the transfer impedance is a function of both the electric field and magnetic field. The contribution from the electric field is valid at low frequencies; whereas the second part of equation 2.10 illustrates that the mutual inductance is the foremost contributor in the high frequency regime. To solve equation 2.10, one needs to derive an equation for the mutual inductance between the CM and DM circuits.

2.7 Mutual Inductance

The mutual inductance is derived here for the redrawn three-conductor configuration of Figure 2.9 When the radii r_1, r_2 and r_3, are small compared to D and Δz, the mutual inductance M for solid cylindrical shaped conductors can be derived from the magnetic field [8] given as:

$$H = \frac{I}{2\pi r} \quad [A/m] \tag{2.11}$$

where I is the current [A] and r the radius [m].

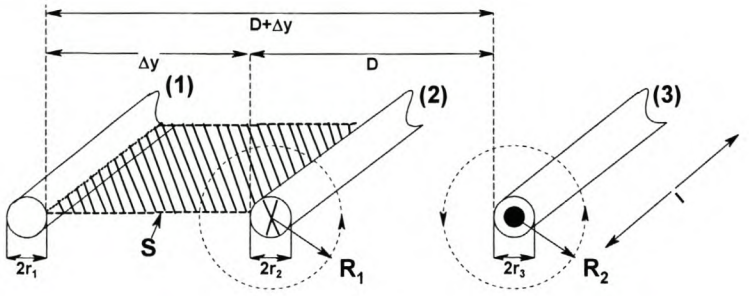

Figure 2.10: *Graphical illustration of three-wire configuration to determine the mutual inductance between the two loops formed by conductors 1-3. S is the surface threaded by the magnetic fields generated by conductors 2 and 3.*

The currents, in conductors (*2*) and (*3*), flow in opposite directions, resulting in the *H*-field of these conductors to rotate in opposite directions. Superposition is implemented to determine the total magnetic flux threading surface ***S*** as illustrated in Figure 2.10. The mutual inductance defined by [8] is:

$$M = \frac{\int_S \mu_0 H da}{I} = \frac{\int_{r_2}^{\Delta y + r_2} \int_0^l \mu_0 H dl dR_1 - \int_D^{D+\Delta y} \int_0^l \mu_0 H dl dR_2}{I} \tag{2.12}$$

$$= \frac{\mu_0 l}{2\pi}\left[\int_{r_2}^{\Delta y} \frac{1}{r_1} dR_1 - \int_{r_3+D}^{D+\Delta y} \frac{1}{r_2} dR_2\right] \tag{2.13}$$

By solving the integrals in equation (2.13), the simplified equation (2.14) is obtained.

$$M = \frac{\mu_0 l}{2\pi}\left\{\ln\left(\frac{\Delta y}{r_2}\right) - \ln\left(\frac{D+\Delta y}{D}\right)\right\} \tag{2.14}$$

If $\Delta y << D$ (equation 2.14), the second logarithm in this equation becomes *ln (1) = 0* and the equation reduces to:

$$M = \frac{\mu_0 l}{2\pi} \ln(\frac{\Delta y}{r_2}) \quad \text{for } \Delta y > r_2 \tag{2.15}$$

It is therefore important to maximize the distance *D* of the return conductor from conductor (2) and the pickup loop as the magnetic field decreases by a factor *1/r*. If this is accomplished, one can assume that the fields generated by conductor (3) are negligible and do not influence the transfer impedance of the system. Substitution of (2.15) into (2.8) gives:

$$Z_t / l = \frac{J_y}{\sigma} + \frac{j\omega\mu_0}{2\pi} \ln(\frac{\Delta z}{r_2}) \quad (\text{for } \Delta z > r_2) \ [\Omega/\text{m}] \tag{2.16}$$

Note that Δy is replaced with Δz as in Figure 2.10. From equation (2.16), it becomes clear that Z_t is dominated by *M* at high frequencies. The mutual inductance of a three-wire system is thus mainly a function of the geometrical properties of conductor 2 and the distance between conductor (1) and (2).

The fact that the transfer impedance is a function of both the *E* (*LF*)-and-*H* (*HF*) fields raises the question of where the transition form *LF* to *HF* takes place. If the geometrical properties, of conductor 2, are altered, the total magnetic flux threading surface ***S*** can be manipulated in order to ensure lower transfer impedance assuming that the *CM* current remains constant. The term r_2 is the radius of conductor (2), this is for a round conductor. However, the conductor can be rectangular with an effective radius, which will be determined by the geometry of the conductor. Therefore, if we change certain geometrical properties of a cable tray, the mutual inductance and transfer impedance can be altered.

2.8 Conclusions

This chapter presented the most important aspects to be considered when defining the transfer impedance of cable trays. Cable trays are used not only for mechanical support,

but for also for shielding cables and wiring. The shielding property of a cable tray is defined in terms of the transfer impedance Z_t, which in turn is a function of the skin depth (material properties), geometry, and mutual inductance of three-wire systems. If these aspects are clearly understood we can move on to develop a theoretical and numerical model followed by measurements to validate our findings.

Chapter 3

Theoretical Analysis of Non-Magnetic Cable Trays

3.1 Introduction

Chapter 2 introduced the general transfer impedance concept applied to a three-wire system. It was noted that conductor (*2*) in the configuration of Figure 2.9 influences the magnitude of the mutual inductance between the *CM* and *DM* circuits, and consequently the transfer impedance of three wire configurations. This chapter presents the case where conductor (*2*) is replaced by a non-magnetic cable tray, as depicted in Figure 3.1. The cross-section in the yz-plane is made at x = 0 and the total width of the tray is equal to *2w*.

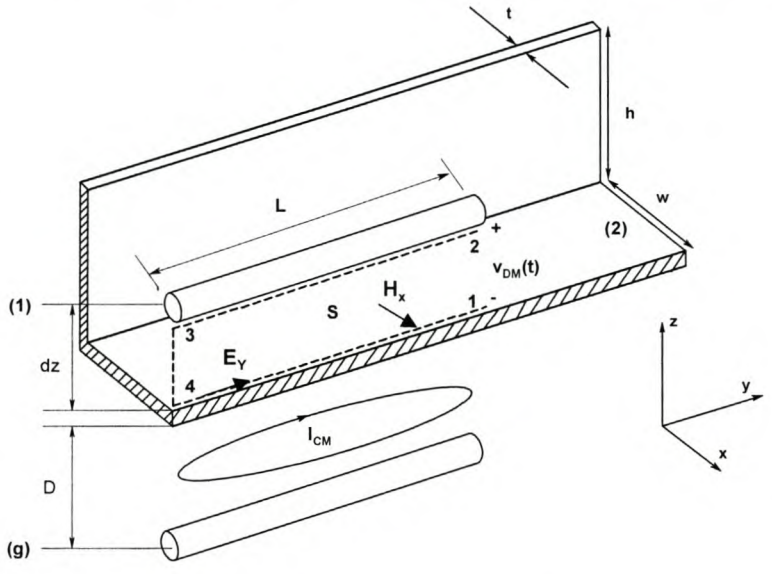

Figure 3.1: *Illustration of the coupling mechanism between differential mode voltage and common mode current for non-magnetic cable tray. I_{CM} causes an electric field along path 1-4 and a magnetic flux threading loop 1-2-3-4.*

Conductor (*1*) can be placed at any *xz* position within the tray, as seen in Figure 3.1, in order to measure the transfer impedance. The *DM* voltage V_{DM} due to the *CM* current I_{CM} is measured between points *1* and *2*. The transfer impedance is the ratio of the *DM* voltage and *CM* current and consists of two contributions as seen in equation 3.1. The first term in

equation 3.1 is due to E_y, the E-field on the floor of the conduit between *1* and *4* and is dominant at low frequencies. The end of the wire at point 3 should be attached to the floor of tray in order to create a closed loop in the *yz* plane. The second term of equation 3.1 arises from a time-varying field H_x, threading the surface formed by *1-2-3-4*, and is dominant at high frequencies. The transfer impedance is defined as a per unit length quantity by [1] as:

$$Z_t(x,z)/l = \frac{V_{DM}}{I_{CM}} = \frac{E_y}{I_{CM}} + \frac{j\omega\mu_0 \int_1^2 H_x(x,z)dz}{I_{CM}} \quad [\Omega/\text{m}] \qquad (3.1)$$

Z_t is dependent on the *xz* position of conductor with respect to the tray and depends on the current distribution through the tray. The latter is mainly a function of the shape of the tray, the frequency, and return current [1]. Material properties will only influence Z_t at low frequencies, which is discussed later.

3.2 Cable tray shape factors

In order to determine the transition point from low frequency to high frequency, we have to consider the skin effect and height-to-width ratios of different cable trays. The term high frequency is used here for $\delta \leq t$ and quasi-static rules still apply. At low frequencies, the current distribution through the cross-sectional area will be homogenous and at higher frequencies, the current will accumulate at the surface of the tray near the edges due to the skin effect [1]. There are five distinct frequency points that are identified, namely:

- $f < f_0$ $(\delta >> t)$, this is where the current is homogenously distributed over the tray and the transfer impedance Z_t equals the *DC* resistance of the cable tray
- $f = f_1$, this is where the current starts to concentrate near the edges of the tray and decreases above the central line of the cable tray
- $f = f_2$: at this frequency the decrease introduced by f_1 stabilizes and reaches its high frequency value
- $f = f_3$ $(\delta = t)$: at this frequency the skin depth is equal to the thickness of the metal of the tray

- $f > f_4 = 25 f_3 \quad (\delta < \frac{t}{5})$: for frequencies above f_4 the current is treated as a surface current predominantly flowing on the outside of the tray

Table I contains the different crossover frequencies for four different cable trays with a total cross-sectional length equal to $2w+2h = 250\ mm$; the height-to-width ratios are indicated accordingly.

Table I: *Crossover frequencies for different cable trays ($t=0.56$ mm, $\sigma = 1.74 \times 10^{14}$, $\mu_r = 1$).*

Frequency	*h/w = 1/2*	*h/w = 1*	*h/w = 3/2*	*h/w = 2*
$f_0 = \frac{1}{\mu_0 \sigma t \sqrt{h^2 + w^2}}$ [Hz]	874.2	921.5	903.6	874.2
$f_1 = \frac{f_0}{c(0)}$ [Hz]	1373.2	1447.4	1419.3	1373.2
$f_2 = \frac{u_r f_0}{c(h/w)}$ [Hz]	1507.2	2194.0	3475.4	5142.4
$f_3 = \frac{1}{\pi \mu_0 \mu_r \sigma t^2}$ [kHz]	46.2	46.2	46.2	46.2
$f_4 = 25 f_3$ [MHz]	1.1	1.1	1.1	1.1

The data in Table I illustrates where the transition from *DC* to *HF* is made for cable trays with different height-to-width ratios. For all frequencies below f_0, ideal conductivity can be assumed as the current is homogenously spread throughout the cross-section of the cable tray. For frequencies above f_3, the current tends to flow closer to the surface as the skin effect starts playing a role.

It is important to know these frequencies as shielding specifications will vary with the frequency of the *EMI*. One can design a cable tray accordingly by choosing the material properties to be used to offer sufficient shielding at frequencies as low as *50 Hz*. The three main properties that can be altered to shift f_3 are the conductivity, relative permeability, and metal thickness. We are studying non-magnetic ($\mu_r = 1$) cable trays and the relative

permeability remains constant. In Table I, f_1 and f_2, are defined in terms of *c(h/w)*, respectively.

The constant *c(h/w)* is defined by [1] as the ratio of the high frequency *B*-field to the *DC* or low frequency *B*-field and is given as:

$$c(h/w) = \frac{H(\omega \to \infty)}{H(\omega = 0)} = \frac{2}{\pi - \ln[1 + (h/w)^2]} g(h/w) \tag{3.2}$$

On the other hand, $g(h/w)$ is defined as the ratio of the *B*-field calculated close to the surface above the centre of a flat plate to the calculated *B*-field of a specified cable tray at the same position.

The main emphasis here is that the shape factors can be calculated as long as the *B*-fields are known and assumed correct. Van Helvoort [1] makes use of the *BEM* to calculate the *B*-fields above the surface of a plate and cable tray. Although our numerical model is only presented in chapter 4, the same approach was followed to determine *g(h/w)* with *MoM* code in order to validate the values obtained by [1]. The results of the *MoM* versus *BEM* calculations are plotted in Figure 3.2.

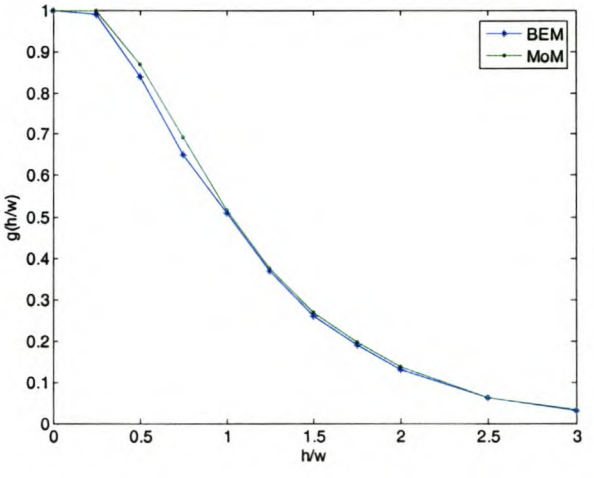

Figure 3.2: *Comparison of BEM [1] and MoM data to determine the height-width factor g(h/w) for cable trays.*

The two techniques utilized are in good agreement with regard to *g(h/w)*. The shape factor *c(h/w)* will therefore also agree. Table II contains the shape factors for several height-to-width ratios and are used in the engineering expressions to calculate the magnetic field and transfer impedance for $f > f_3$.

Table II: *Values of the shape factor c(h/w) and g(h/w) for different height-to-width ratios(after [1]).*

h/w	g(h/w)	c(h/w)	h/w	g(h/w)	c(h/w)
0	1	$\frac{2}{\pi}$	7/4	0.19	0.22
1/4	0.99	0.64	2	0.13	0.17
1/2	0.84	0.58	5/2	0.63	0.11
3/4	0.65	0.48	3	0.031	0.074
1	0.51	0.42	5	0.0017	-0.029
5/4	0.37	0.34	10	9e-7	-1e-6
3/2	0.26	0.26			

3.3 Current distribution

The prediction of the current distribution through a cable tray at *LF* and *HF* can be simplified by observing the configuration shown in Figure 3.3. If the cable tray is closed at the ends and current is injected by means of a voltage source at point (*C*), the current has two paths it can travel at *HF*, as depicted in Figure 3.3.

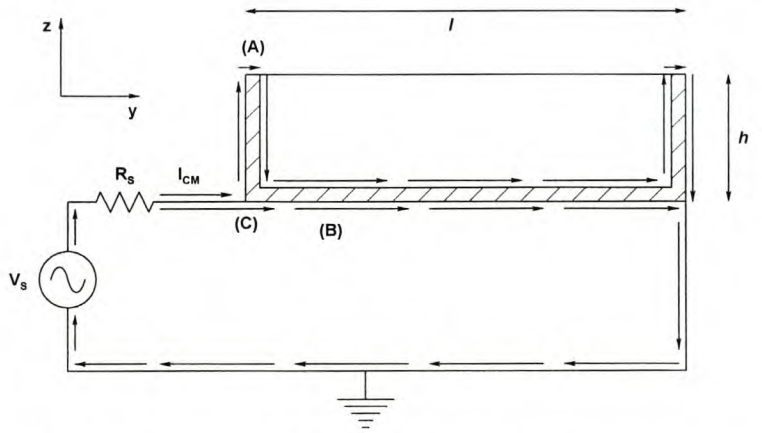

Figure 3.3: *Cross-sectional view to illustrate two current paths at HF.*

At *DC*, we expect the current distribution to be homogenous resulting in equal values for the current density in the interior and exterior regions. However, at high frequencies the current distribution in the two regions will differ. Path (*A*) in the figure is longer than path (*B*) and at high frequencies the current will tend to follow the path with lowest inductance. The impedance at high frequencies will be dominated by the inductive component of the tray, which is a function of the length of the path the current has to travel. At high frequencies, the amplitude of the current should be greater on the outside than on the inside of the tray because path (*B*) is shorter than (*A*). This is additionally a consequence of the skin effect. At high frequencies, we therefore assume that the current predominantly flows on the outer surface.

In order to determine the current density above the floor of the tray at x = 0, the tray is replaced with a plate as depicted in Figure 3.4. The plate extends infinitely in both the *x* and *y* directions and has finite thickness *t*. The sidewalls are ignored, as the *x* component of the *B*-field here should be equal to zero at *HF*.

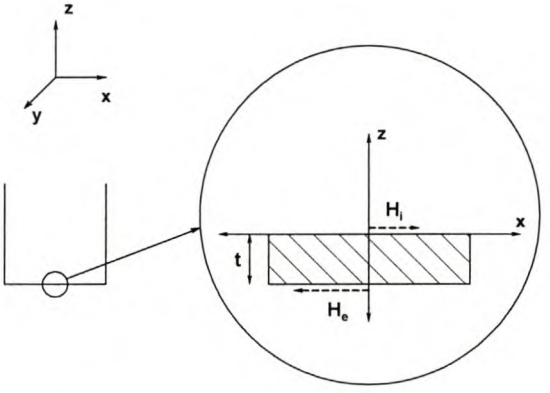

Figure 3.4: *Cross-section to illustrate the calculation of the current density in terms of the internal H-field* H_i *and external H-field* H_e.

The current is determined by the *H*-field above and below the plate. If the *H*-fields are close to the surface, we can assume that the fields will consist only of an *x* component parallel to the surface. The *H*-field above the plate is denoted by H_i and below the plate by H_e. In order to obtain a solution for the current density, a solution for the *x*-component

of the *H*-field is necessary. A one-dimensional differential equation inside the plate given by [1] is:

$$\frac{d^2H_x}{dz^2} = k^2 H_x \tag{3.3}$$

Where $k = \frac{1+j}{\delta}$ with δ = skin depth.
Equation 3.3 has the general solution in the form of equation 3.4.

$$H_x(z) = Ae^{kz} + Be^{-kz} \tag{3.4}$$

The coefficients *A* and *B* are solved by imposing the boundary conditions on both surfaces of the plate, thus at $z = 0$ and $z = -t$. This leads to:

$$H_x(z=0) = H_i \tag{3.5}$$

$$H_x(z=-t) = -H_e \tag{3.6}$$

Substitution of 3.5 and 3.6 into 3.4, and after algebraic manipulation, leads to:

$$A = H_i - B \tag{3.7}$$

$$B = -\frac{H_e - H_i e^{-kt}}{e^{kt} - e^{-kt}} \tag{3.8}$$

The magnetic field inside the plate can then be described by the following equation:

$$H_x(z) = \left(H_i + \frac{H_e - H_i e^{-kt}}{e^{kt} - e^{-kt}} \right) e^{kz} - \frac{H_e - H_i e^{-kt}}{e^{kt} - e^{-kt}} e^{-kz} \tag{3.9}$$

In order to calculate the current density inside the plate, we make use of Ampere's law in differential form, given as:

$$\boldsymbol{J} = \nabla \times \boldsymbol{H} \tag{3.10}$$

The current density is then described by:

$$J_y(z) = (\nabla \times \boldsymbol{H})_y = \frac{dH_x}{dz} = k\left\{\left(H_i + \frac{H_e - H_i e^{-kt}}{e^{kt} - e^{-kt}}\right)e^{kz} + \frac{H_e - H_i e^{-kt}}{e^{kt} - e^{-kt}} e^{-kz}\right\} \tag{3.11}$$

We are mainly interested in the current density at the floor of the plate where $z = 0$. By substituting $z = 0$ in equation 3.11, the formula for the current density at the floor of the tray then becomes:

$$J_y(0) = kH_i + 2k\left(\frac{H_e - H_i e^{-kt}}{e^{kt} - e^{-kt}}\right) \tag{3.12}$$

Equation 3.12 is valid for $f > f_3$. In the high frequency approximation, the magnetic field is calculated assuming surface currents due to the skin effect. The high frequency referred to here is where $\delta \leq t$ and quasi-static rules still apply. The eddy current constant k, which is a function of the skin depth, increases with frequency. Above f_4, the second term of equation 3.12 becomes negligible. Thus:

$$J_y = kH_i \tag{3.13}$$

At *LF* ($f < f_3$), the current density is determined by:

$$J_y = J_{DC}\left(\frac{j\omega\tau_1 + 1}{j\omega\tau_0 + 1}\right) \tag{3.14}$$

where $J_{DC} = \frac{I_{CM}}{2(h+w)t}$, $\tau_0 = \mu_0 \sigma t\sqrt{h^2 + w^2}\,/2\pi$ and $\tau_1 = \frac{2}{\pi}\tau_0$ [1].

Equation 3.12 can be solved for a cable tray by computing the fields H_i and H_e with *FEKO*® (as described in the next chapter) and substituting the solutions into 3.12, assuming that the numerical values are correct and that the current is kept constant versus frequency. A plot of equations 3.13 and 3.14 for the cable tray with $h/w = 2$ is presented in Figure 3.5.

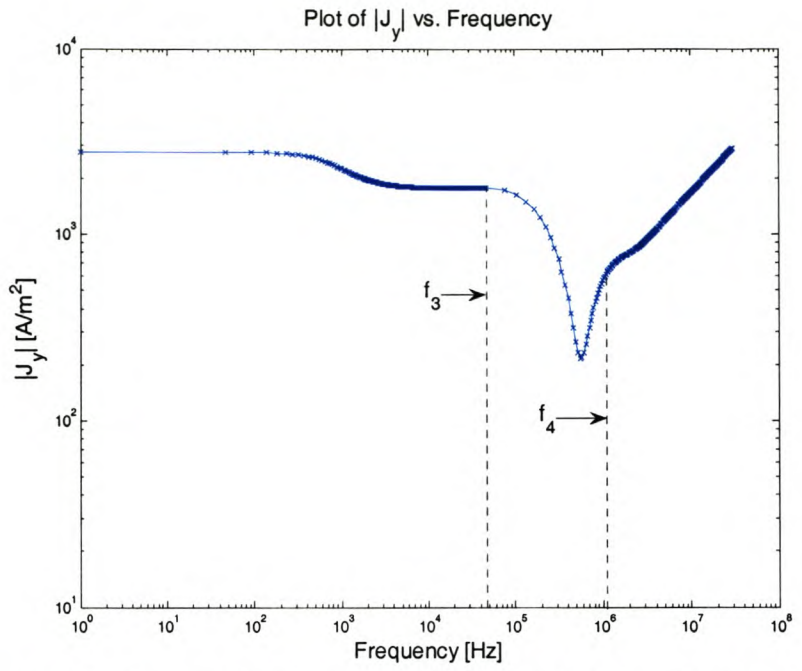

Figure 3.5: *Current density versus frequency for h/w = 2 at (x=0,z=0).*

The dip in current density for $f_3 < f < f_4$ can be attributed to the skin effect as $\delta \leq t$ for $f > f_3$. The dip in the current density is not important with respect to the transfer impedance because the magnetic flux will mainly contribute to Z_t for frequencies above f_3. However, it is important to note the change in the current density for frequencies below f_3, as it suggests that the total current through the tray remains the same and that it concentrates at the outside edges [1].

3.4 Transfer impedance

3.4.1 DC Approximation

For low frequencies ($f < f_3$) the current density in the cable tray can be approximated as homogeneous and is determined by the total *DC* current through the total cross-sectional area of the tray and is given by [1] as:

$$J_{yDC}(x,z) = \frac{I_{CM}}{2(h+w)t} \tag{3.15}$$

The magnetic field at an arbitrary point (x,z) inside the tray can be determined by the superposition of an infinite number of line currents [1]. The derivations and complete solution for the entire xz region are presented in appendix B. The magnetic field is used to determine the transfer impedance in equation 3.1. For low frequencies, the transfer impedance above the centre of the tray floors is given by [1] as:

$$Z_{tDC}(0,\Delta z) = \frac{1}{2\sigma(h+w)t} + j\omega\frac{\Delta z}{4(h+w)}\left\{1-\frac{1}{\pi}\ln[1+(\frac{h}{w})^2]\right\} \tag{3.16}$$

The second term is also a function of Δz, this is the distance of the lead above the floor of a tray. For $f < f_3$ the first term in equation 3.8 is dominant whereas the second term is negligible. The transfer impedance is thus equal to the *DC* resistance of the tray at low frequencies.

3.4.2 HF Approximation

At high frequencies, the skin depth is small compared to the thickness of the tray. For $f > f_4$ it is sufficient to assume surface currents on the tray floor and sidewalls. The magnetic fields outside any metallic regions can then be calculated by solving the scalar Laplace equation in two dimensions.

$$\nabla^2\varphi(x,z) = \frac{\partial^2\varphi(x,z)}{\partial x^2} + \frac{\partial^2\varphi(x,z)}{\partial z^2} = 0 \tag{3.17}$$

The solution for equation 3.17 results in equation 3.18, which represents the magnetic field in the interior region of a cable tray. The derivation is shown in appendix *B*.

$$H_{xHF}(x,z) = \frac{\gamma\pi I_{cm}}{2w}\cosh\left(\frac{\pi z}{2w}\right)\cos\left(\frac{\pi x}{2w}\right) \quad for\ z \le z_c = h - 0.8w \tag{3.18}$$

where $\gamma = \dfrac{wg(h/w)}{\pi^2(h+w)}$ with w = width, $g(h/w)$ the shape factor and h = height [1].

Van Helvoort [1] states that this equation is valid for positions far away from the rim of the tray. This is because boundary conditions are imposed in order to calculate the magnetic field. A cable tray only has three boundaries, the two sidewalls, and the tray floor. The equation is therefore only valid for positions far away from the top rim of a cable tray. Substitution of 3.18 into 3.1 leads to the formula for the transfer impedance in the *xz* plane:

$$Z_{tHF}(x,z) = \frac{g(h/w)\cos(\frac{\pi x}{2w})\left\{ j\omega\mu_0 \frac{2w}{\pi}\sinh(\frac{\pi z}{2w})\right\}}{2\pi(h+w)} \tag{3.19}$$

The mutual inductance $M(x,z) = Z_{tHF}(x,z)/2\pi f$ in the *xz* plane is plotted in Figure 3.6 for four cable trays. The horizontal lines indicate regions where $z \leq z_c = h - 0.8w$ [1], which implies that equation *3.19* is not accurate for trays with a height-width-ratio *h/w*≤ *4/5*. The *x* and *z*-axes are normalized.

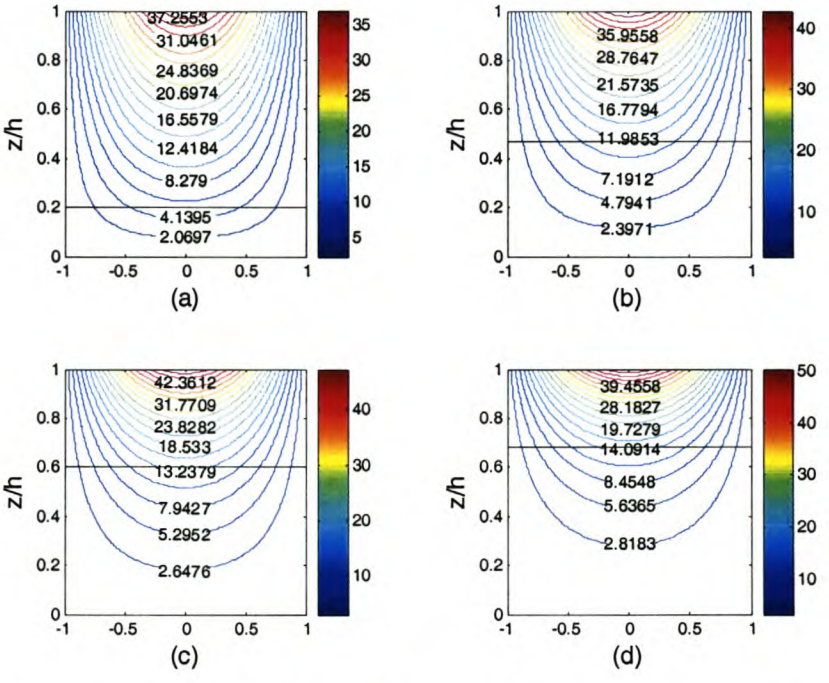

Figure 3.6: *Theoretical plot of M [nH/m] for cable trays with height-to-width ratios of (a) h/w=1 (b) h/w=1/2 (c) h/w=2 (d) h/w=5/2.*

From Figure 3.6 the mutual inductance within a cable tray is thus not a fixed value but indeed a function of position (*x,z*) within the tray. One would expect the transfer impedance to be a maximum in the top centre of the tray and a minimum at the bottom

corners near the sidewalls. For shallow trays $h/w \leq 1$, the mutual inductance is constant over more than *50%* of the width below the horizontal black line. The deeper trays offer a greater region of protection with reduced transfer impedance and mutual inductance.

This can be observed by noticing the bigger area beneath the lowest line of constant M in Figure 3.6. The theoretical values do not consider the actual current distribution throughout the total cross-section of the tray and the engineering expressions are limited to a certain region within a cable tray. The mutual inductance at the floor of each tray is presented in a normalized plot in Figure 3.7 to emphasize the fact the transfer impedance is lower for trays with a greater height-to-width ratio.

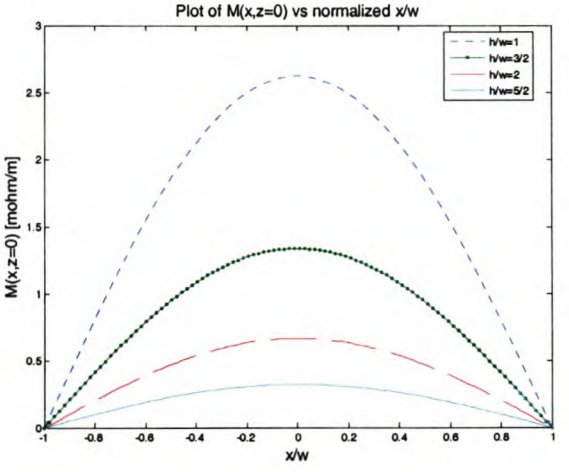

Figure 3.7: *Theoretical plot of M [mH/m] for cable trays with height-to-width ratios of (a) h/w=1 (b) h/w=1/2 (c) h/w=2 (d) h/w=5/2 at (x,z = 0).*

The theoretical frequency response of the *HF* $Z_t(x = 0, z = 5)$ is plotted in Figure 3.8(a). Once more, we see that the transfer impedance differs for the different cable trays. The transfer impedance decreases with an increase in height-to-width ratio.

The gradient, $\left.\frac{dZ_t}{df}\right|_{x=0,z=5}$ for the different trays is the mutual inductance M, which suggests that deep trays provide better shielding. Figure 3.8(b) contains the mutual inductance, which proves that cables in a shallow tray are more prone to couple with the B-fields produced by the *CM* current.

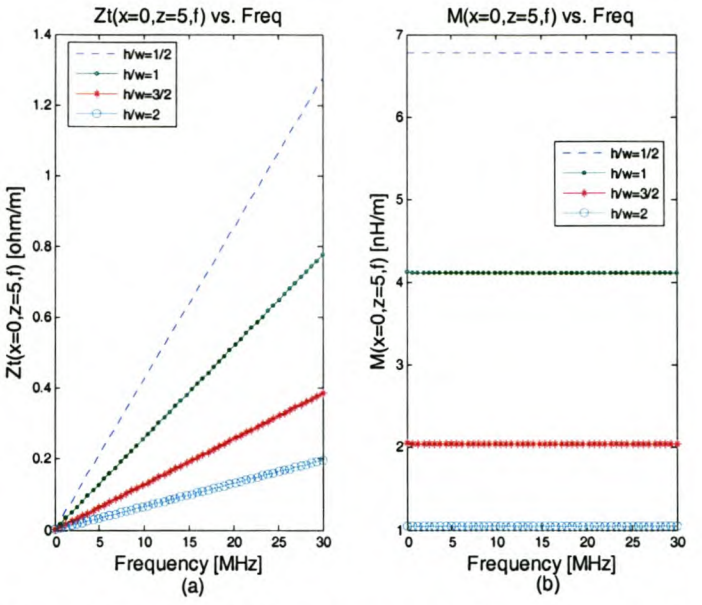

Figure 3.8: *(a) Plot of $Z_t(x=0,z=5,f)$ vs. frequency for different cable trays (b) Plot of $M(x=0,z=5,f)$ vs. frequency for different cable trays.*

3.5 Conclusions

The theory and engineering expressions presented in this chapter bring forth a better understanding on how cable tray shielding works. Different frequency regions were identified which allows us to distinguish between *LF* and *HF*. The most important factors that determine the crossover frequencies are material properties, conductivity, relative permeability and thickness of the metal. Additionally, we get the impression that deep trays provide better shielding in a greater cross-sectional area than shallow trays. The cable tray constants, *c(h/w)* and *g(h/w)*, calculated by [1] have also been verified with *MoM*. The results presented here are based on certain approximations and the next chapter introduces the development of a numerical model to obtain a more accurate analysis of non-magnetic cable trays.

Chapter 4

Computational Modelling Of Cable Trays

4.1 Introduction

With the theoretical background of chapter 3 in place, we now move on to develop a numerical model for non-magnetic cable trays. The main limitation of the theory is that the transfer impedance is only defined for a certain region within the interior region of a cable tray close to the tray floor.

A logical method of analysis, design, and measurement would most often include a simulation model. The advantages of defining an *EMC* software model are numerous in the sense that several geometrical, material, and output parameters can be changed rapidly and without difficulty to save time and monetary resources.

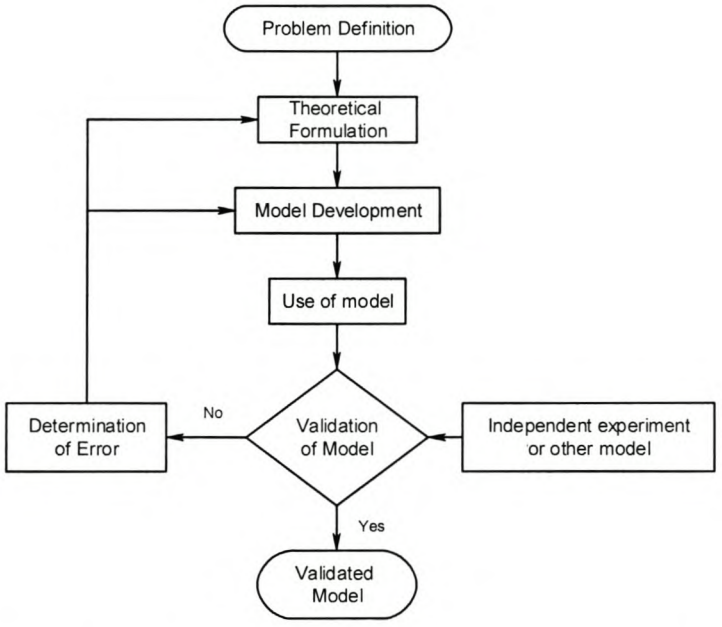

Figure 4.1: *Development of a numerical model (after [4])].*

Figure 4.1 depicts the method of model development for *EMC* problems. This method of model development relies on independent experiments or observations to validate the

overall model, which consists of both the theoretical and numerical implementation of the solution. The focus of this chapter is to develop a computational model for non-magnetic cable trays of different height-to-width ratios in order to determine the transfer impedance $Z(x,z)$ and mutual inductance $M(x,z)$ from numerically calculated magnetic fields $H_x(x,z)$. The results of the simulations are then compared against measurements in the following chapter. The numerical model will be developed according to the circuit configuration portrayed in Figure 3.3.

4.2 Overview of computational electromagnetics

Computational electromagnetics is concerned with the numerical approximation of Maxwell's equations. Maxwell's equations are not presented here as they can be found readily in the literature [7]. The case where no initial physical approximations are made is known as full wave *CEM*. Currently the three most popular "full-wave" methods are the Finite Difference Time Domain (*FDTD*) Method, Method of Moments (*MoM*), and the Finite Element Method (*FEM*). All these methods have strengths and weaknesses and it is up to the analyst to decide which technique would best suit his needs.

The numerical code chosen to analyse our problem at hand makes use of the *MoM*. The software package is known as *FEKO*® and is mainly used to solve problems of arbitrary shape. It allows the user to define structures using metallic triangles, wire segments, dielectric cuboids or tetrahedrons. The electromagnetic fields are obtained by calculating the electric surface currents on conducting surfaces.

4.3 Numerical model specifications

Before embarking on model development, the specifications of the model need to be stipulated thoroughly. The numeric model of the cable tray should allow:

- the model to represent the real world circuit configuration as realistically as possible
- the use of the skin effect
- Simulations to be done at multiple frequency points
- A two-port network representation in order to obtain *S*-parameters

- The calculation of the interior and exterior magnetic field as closely as possible to the metallic surface of the cable tray

These specifications enable us to determine the transfer impedance of cable trays at specific points within the *xz* plane, together with the magnetic fields within the inner and outer boundaries of the conduit close to the metallic surface.

4.4 Defining the Geometry

A simple *U*-shaped cable tray is a flat metallic plate with the sides bent upward. The boundaries of the cable tray are defined using *PREFEKO* by defining points at the appropriate coordinates with the *DP* (Define Point) card. The metallic surfaces are then created with surface triangles. This process is referred to as meshing or discretization. The meshing is automatically performed by *PREFEKO* following pre-defined rules, which are set with the *IP* card.

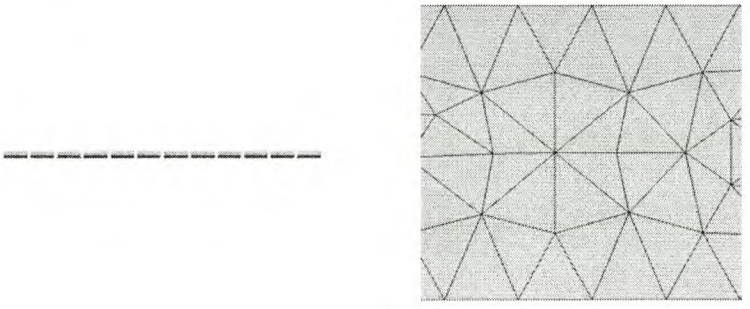

Figure 4.2: *Discretization of (a) wire segments and (b) surface triangles.*

There are several rules that need to be adhered to regarding to the ohmic connections between segments, etc. Details about these rules are not presented here and can be found in the *FEKO*® user manual. However, it is important and not necessarily obvious, that the discretization should be an optimal size to produce accurate results. Figure 4.2 portrays an illustration of the meshing of wire segments and metallic surfaces. The *MoM* code computes the wire and surface currents by setting up a matrix equation for each frequency step. Depending on the matrix size and available computer resources, this may take a considerable amount of time. Optimal discretization not only improves results but also

reduces computation time. It is the user's responsibility to confirm the convergence of the solution produced by *FEKO*®. The easiest way to accomplish this is to increase and decrease the discretization of the surface triangles and wire segments and see if the same results are achieved. If the results differ, the meshing can be adjusted appropriately to achieve convergence and subsequently more accurate results.

From the theory presented in chapter three, and the cross-section of the tray depicted in Figure 3.1, it is clear that $x = 0$ (yz plane), is a plane of symmetry if we assume that the current flows symmetrically through the tray. Computation time and memory usage can further be reduced by specifying the symmetry of the geometry, if applicable. Three main symmetries can be implemented using *FEKO*®. The *SY* geometry card fulfils this function and the three different types of symmetry are listed below:

- Geometric symmetry
- Electric symmetry
- Magnetic symmetry

The latter is of greatest importance here because we are interested in the magnetic field distribution. A magnetic symmetry plane is a plane that can be replaced by an ideal magnetically conducting wall without changing the field distribution. Figure 4.3 depicts the plane of magnetic symmetry. It is observed that the ***E***-field's normal component and the ***H***-field's tangential component disappear. In addition, the magnetic current density ***M*** is asymmetric and the electric current distribution ***J*** symmetric.

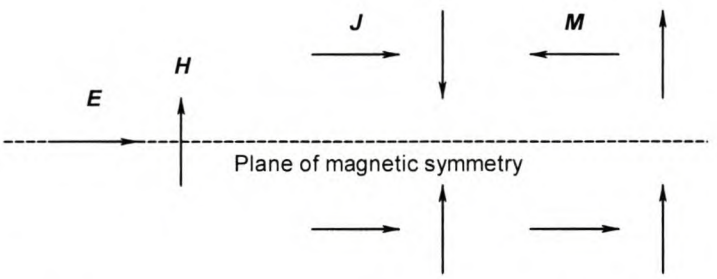

Figure 4.3: *Illustration of a magnetic symmetry plane (after [9]).*

By defining a plane of symmetry, *FEKO®* calculates the unknown values on one side of the symmetry plane and then mirrors it around the same plane. This is useful when dealing with large structures.

Due to our quasi-static approach, the field along the y-axis will be equal in amplitude along the entire length of the structure, if end-effects are ignored. One would then argue that this is a two-dimensional problem. This is true only if the magnetic fields in the cross-section are to be determined. In contrast, if we are interested in the *S*-parameters, the problem becomes three-dimensional, as the total length of the structure will influence the impedance seen by any of the two ports. The area of the pickup loop described in chapter 3 is also a function of the total length of the tray.

Since the conduit is symmetrical around the $x = 0$ plane one can expect the current distribution and hence magnetic field also to be symmetrical around the same axis if we assume a symmetrical current distribution. The solution is therefore defined to be magnetically symmetrical around the $x = 0$ axis by selecting the magnetic symmetry option of the *SY* geometry card in *PREFEKO*.

In order to determine the length of the tray one has to consider the upper frequency limit of the simulation or experiment. The upper frequency bound used by [1] is *10 MHz*. Van Helvoort [1] presumably used test equipment less sensitive than an *ANA*. The length of the loop used by [1] had to be a minimum length to ensure a detectable signal and therefore the frequency of *10 MHz*. It was decided to choose the upper bound for this specific task to be *30 MHz*. Transfer impedance, in general, is denoted as a per metre quantity. Due to the quasi-static nature of this experiment, it is important to limit the electrical length of the *CUT* to about at least a tenth of a wavelength of the maximum frequency ($\lambda/10$) in order to keep it "electrically short" and minimize the effects of resonance and wave effects as explained in chapter 2. If this rule is adhered to, the length can be calculated as:

$$\lambda = \frac{c}{f} = \frac{2.997\times10^{8}}{30\times10^{6}} \approx 10\ m \tag{4.1}$$

where $c = 2.99\times10^{8}$, the speed of light (*m/s*), f the frequency (*Hz*) and λ the wavelength (*m*).

$$\Rightarrow l = \frac{\lambda}{10} = 1\,m \tag{4.2}$$

Figure 4.4 shows the discretized cable tray as defined in *FEKO*®. However, the primary purpose of a conduit is to shield cables in the interior region and if current flows on the inside of the tray, shielding is ineffective.

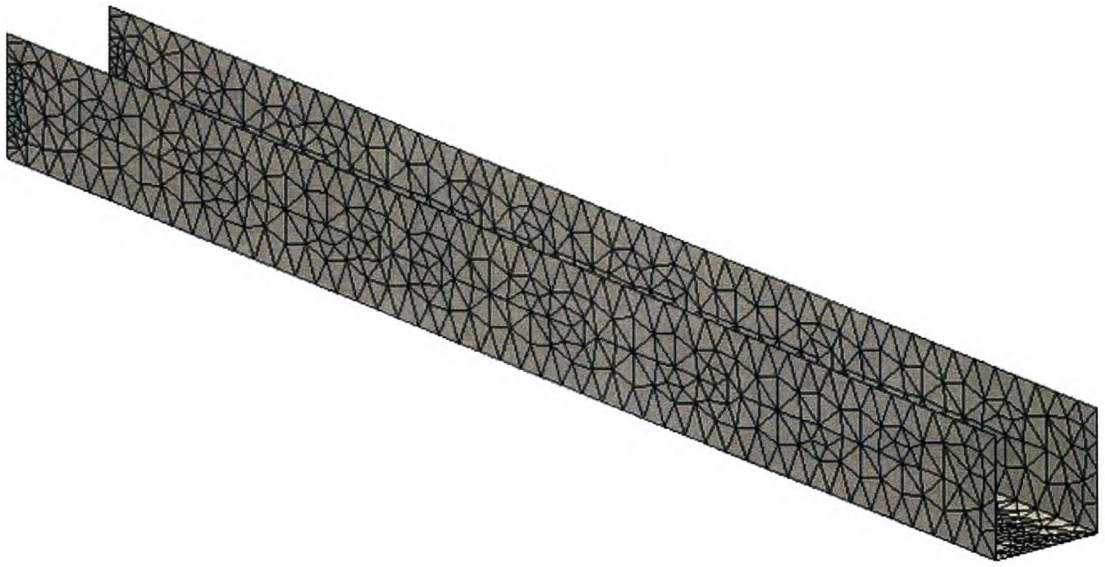

Figure 4.4: *Geometry of discretized cable tray.*

To assure that the current flows predominantly on the outside surface of the tray, the open edges need to be closed off. In addition, an appropriate technique to inject the current, define the return-and-pickup conductors, implement the skin effect, and define a computational two-port network needs to be developed. These design details are discussed in the sections to follow.

4.5 Two-Port analysis approach

One outcome of this thesis is to measure the transfer impedance of non-magnetic cable trays with an *ANA*. The procedure is automatic and measurements at numerous frequency points can be accomplished with great accuracy. Figure 4.5 depicts a two-port network with incident and reflected waves.

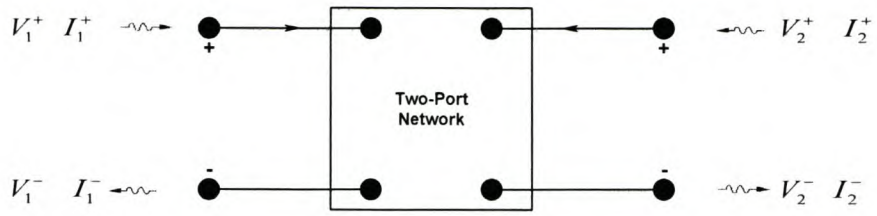

Figure 4.5: *Two-port network.*

S-parameters are defined in terms of these waves as follows:

$$S_{ij} = \left.\frac{V_i^-}{V_j^+}\right|_{V_k^+ = 0 \text{ for } k \neq j} \tag{4.3}$$

S_{ij} is found by driving port j with an incident voltage wave V_j^+, and measuring the reflected voltage wave V_i^-, coming out of port i. The incident waves on all ports except the jth port are set to zero, which means that all the ports should be terminated in matched loads to avoid reflections. Thus, S_{ii} is the reflection seen looking into port i when all other ports are terminated with matched loads, and S_{ij} is the transmission coefficient from port j to port i when all other ports are terminated in matched loads [10].

Two ports need to be defined. A common mode current $I_1 = I_{CM}$ is generated at port one and the resulting differential mode voltage $V_2 = V_{DM}$ measured at port two. Arbitrary two-port networks can also be described in terms of impedance parameters [10]. This is accomplished by conversion of the *S*-parameters to impedance parameters or *Z*-parameters. The impedance parameters are related to the voltages and currents at the two ports as:

$$V_1 = Z_{11}I_1 + Z_{12}I_2 \tag{4.4}$$

$$V_2 = Z_{21}I_1 + Z_{22}I_2 \tag{4.5}$$

The transfer impedance is then defined as:

$$Z_t = \left.\frac{V_2}{I_1}\right|_{I_2=0} = \left.\frac{V_{DM}}{I_{CM}}\right|_{I_2=0} = Z_{21}/l \ [\Omega/\text{m}] \tag{4.6}$$

In the case of a passive linear two-port network, the reciprocity theorem holds and:

$$Z_{21} = Z_{12} \tag{4.7}$$

The advantage of this method is the fact that the acquired *S*-parameter set can be converted to *Z*-parameters with ease in order to attain the transfer impedance from *ANA* measurements.

4.6 Current injection technique: Port 1

If the internal region of the cable tray was to be protected from external fields, originating from current flowing on the outer region of the conduit, it makes sense to force the flow of current on the exterior surface only. This would only be possible if eddy current shielding is assumed. The amplitude of the disturbance current must be at a sufficient frequency for meaningful skin effect as discussed in chapter 2. Although plane wave shielding is an effective method to protect the inner region from unwanted interference, it is a far field approach to the problem. We assume here that the interior is protected by means of near-field magnetic shielding and that the magnetic fields are generated by current flowing symmetrically through the conduit generated by a local source. Current flow through the tray can also be induced by a plane wave in practice; however, this approach is not followed here. Instead, current will be injected by means of a voltage source.

From the previous discussion, the current distribution over the surface of the tray should have a symmetrical distribution in the *xz* plane. Furthermore, current flow in the interior region should be minimized as far as possible. For the current to be symmetrical around the xz plane an injection point should be chosen on the $x = 0$ axis of Figure 3.1. The next step is to guarantee that current flow in the inner region of the tray is kept to a minimum. This is established by closing the two boundaries in the *yz* plane at the ends of the tray by defining metallic plates at the ends.

This creates a path of high impedance if current is injected at the lowest point of the cable tray at $x = 0$. The current will then flow along the exterior floor and sides of the cable tray at high frequencies. An injection point is defined at $x = 0$ at the bottom of one of the ends on the exterior of the conduit as depicted in Figure 4.6.

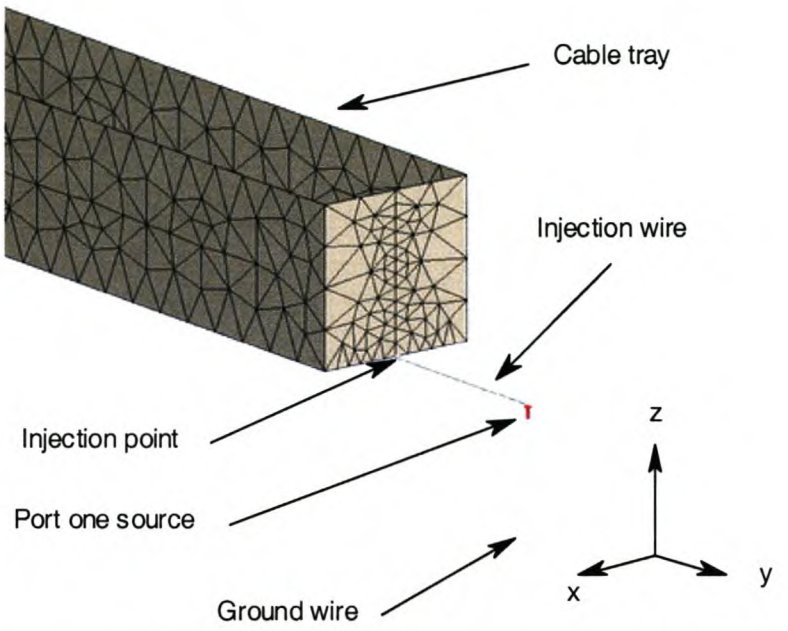

Figure 4.6: *View of cable tray to illustrate the current injection feed point, representing port one of a two- port network.*

A wire is defined by means of the *BL* geometry card and attached to this point. Consequently, the wire is connected to ground via additional wire segments. One segment contains the source produced with an A_1 control card, which adds a voltage source to a segment. This specific segment of our model represents port one of an *ANA*. The magnitude and phase of the voltage can be defined together with the *S*-parameter impedance, which is elected to be *50 ohm*. A section of the cable tray and injection wire together with the source and ground wire is illustrated in Figure 4.6.

4.7 Pickup Loop: Port 2

A practical approach to measure the magnetic field within the cable tray is to design a magnetic field probe. However, the magnetic field is disturbed by the probe and accurate absolute measurements are rarely possible. Relative measurements are possible with an *ANA*.

The wire described in chapter three serves as a pickup loop, which generates a *DM* voltage due to the *B*-field threading the loop. The pickup loop is created by defining wire segments in the interior region of the tray.

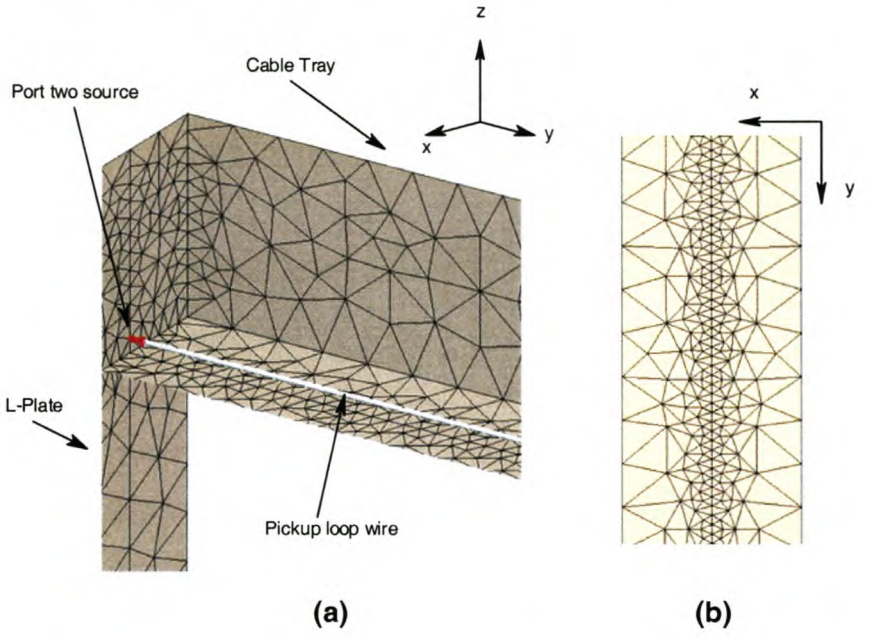

Figure 4.7: *Cutplane view of (a) cable tray to illustrate the pickup loop feed point, representing port two of a two-port network and (b) the discretization below the pickup loop.*

One end of the wire is connected to the floor of the tray and the other end to the side (Figure 4.7(a) and 4.8). The segment connected to the side of the tray serves as the source for port two. Note that the discretization below the pickup wire (Figure 4.7(b)) is smaller compared to the rest of the tray. The *FEKO*® user manual [9] suggests that 8-10 wire segments or surface patch (triangles) per wavelength be used.

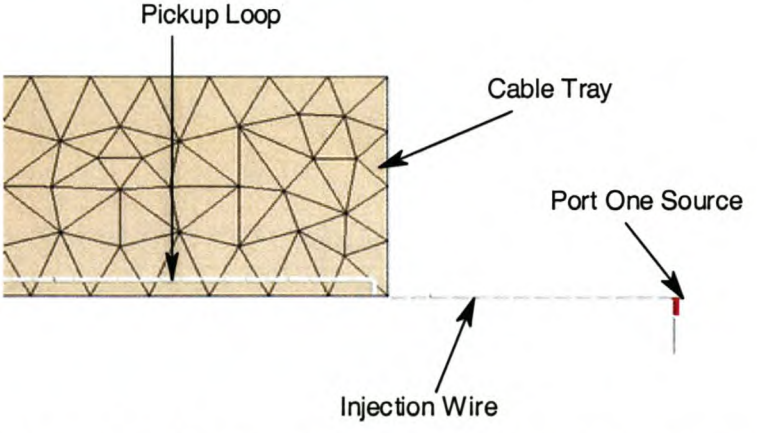

Figure 4.8: *Cutplane view of cable tray to illustrate the termination point of the pickup loop on the floor of the cable tray.*

For geometrical small structure parts like holes, apertures, wires over discretized ground, antenna feed points etc. where wavelength related mesh is not sufficient, special rules have to be applied which take into account the spatial variation of the current. If the pickup wire is close to the surface of the tray, the distance of the wire above the tray should be at least twice the mesh size beneath the pickup wire to produce accurate results. The xz position of the pickup loop can be varied in order to determine Z_t at any coordinate in the xz plane.

4.8 The return conductor

Two conductors of a three-wire system have numerically been defined in the previous sections; the next step is to define the return conductor. The return conductor should have little or no influence on the transfer impedance and this conductor should be as far as possible from the other two. It is also evident from the theory of the mutual inductance that this distance should be maximized. The main reason for this is to reduce any coupling introduced from this conductor. It merely serves as a mechanism to ensure a closed loop for current flow. Several techniques support this specification. Metallic foil can be used which "stretches" the fields and therefore ensures that the field is concentrated at the surface of the foil. Alternatively, a conductor can be used with a far away return path. The latter is neither always achievable nor practical. A well-defined flat surface (electrically conducting ground plane) is a viable option.

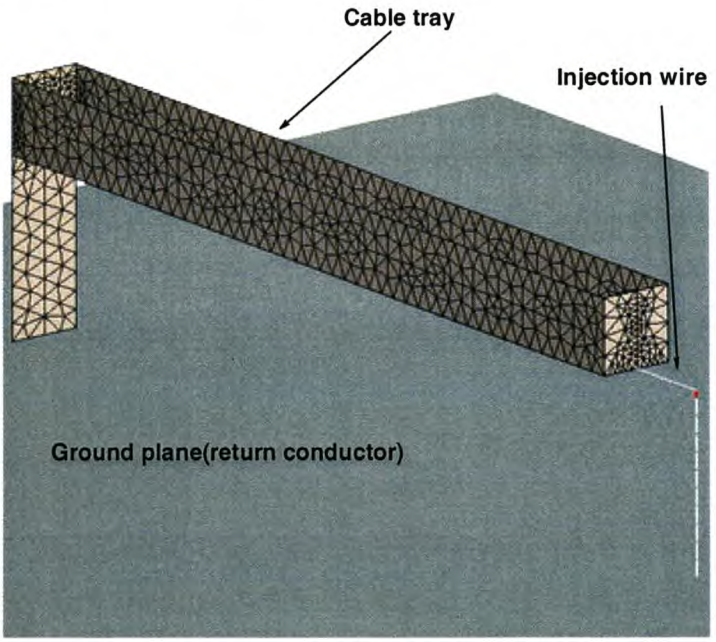

Figure 4.9: *Complete numerical model of a non-magnetic cable tray.*

A perfect electric conducting ground plane can be defined in *FEKO*® with the *BO* card. The next step is to connect the cable tray to the ground plane. This is done by defining a metal plate connecting the conduit to the ground plane. A wire could also possibly be used, but from a practical point of view, a plate would offer mechanical stability during a measurement procedure. Figure 4.9 illustrates the complete geometry of the numerical model for a cable tray.

4.9 Skin effect

Skin effect has to be included in the numerical calculation, as this is an eddy current shielding problem. This is accomplished by adding finite conductivity to all the surface triangles and wire segments previously defined to create the cable tray. The skin effect is implemented in *FEKO*® by using the *SK* card and defining the thickness of the metal, conductivity, and relative permeability.

4.10 Cable Tray Properties

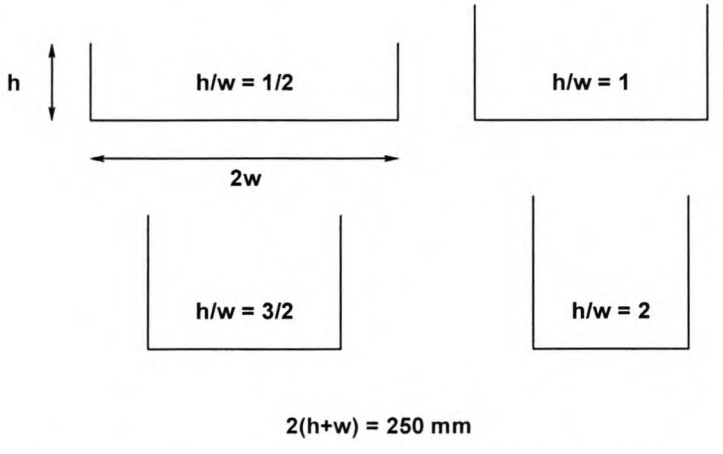

Figure 4.10: *Cross-sectional view of the four cable trays under investigation.*

Four cable trays each with a total cross-sectional length of *250 mm*, length of *1 m* and different height-to-width ratios were simulated. The choice of metal for the cable trays was based on availability, cost, and practical implementation. Brass was chosen and is easy to bend and maintains its shape. The specific compound chosen consists of *70%* Copper and *30%* Zinc (*Cu70Zn30*) and has a conductivity of $\sigma = 1.74 \times 10^7$ $[S/m]$ [11].

The thickness $t = 0.56\ mm$. The conductivity is lower than copper and will result in a shift in the crossover frequencies described in chapter 3. These frequencies are not important here as the *ANA* utilized for measurement starts its frequency sweep at *300 kHz* and the numerical model is developed accordingly.

4.11 Scattering Parameters

The *FR* card is used to specify the frequency points for the *S*-parameter analysis. The bandwidth defined is *300 kHz – 30 MHz* with *200* discrete points. Figure 4.11 contains a comparison of the magnitude and phase of the simulated S_{21} for the four trays. S_{21} is displayed as it gives the ratio of the incident voltage at port one to the reflected voltage at port two. Of interest is the *Z*-parameter Z_{21}, which relates the reflected voltage at port two to the current at port one, and hence the transfer impedance.

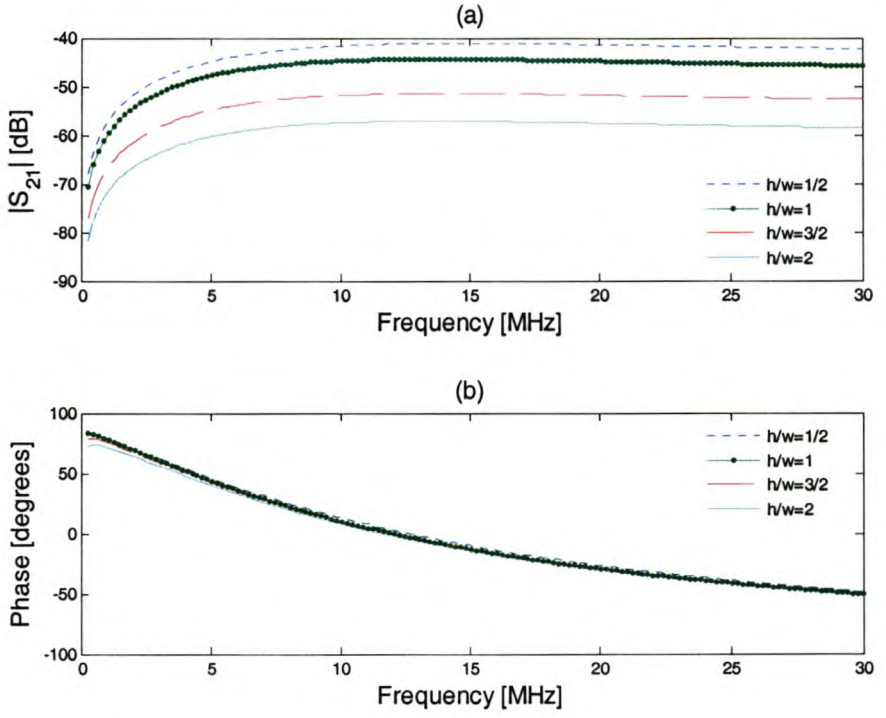

Figure 4.11: *Simulated (a) Magnitude and (b) Phase of S_{21} for four different cable trays with the pickup loop at 5 mm above x = 0.*

The *Z*-parameter set is presented in the following chapter where a comparison is made between the theoretical, numerical, and physical parameters. The magnitude of S_{21} decreases with an increase in height-to-width ratio with a difference of approximately *20 dB* between the deepest tray (*h/w = 2*) and shallow tray (*h/w = 1/2*).

The pickup loop is positioned at $z = 5, 25$ mm as well as the top of each tray above the central ($x = 0$) and side ($x = w - 10$ mm) of each tray. If data obtained at these positions, agree with measurements it is reasonable to assume that the transfer impedance can be calculated at any xz position with our numerical model. From the theory presented in chapter two, we expect Z_t to be a maximum at the top centre and a minimum in the bottom corner positions.

4.12 Magnetic field

In the xz-plane, the resultant magnetic field consists of two field vectors components, namely H_x and H_z as depicted in Figure 4.12. The main source of interference or magnetic field coupling, to the pickup loop (in reality this represents an interior wire/cable to be protected), would be produced by the x-component of the field. This is the only component of the field that threads the surface formed by the floor of the tray and pickup loop perpendicularly.

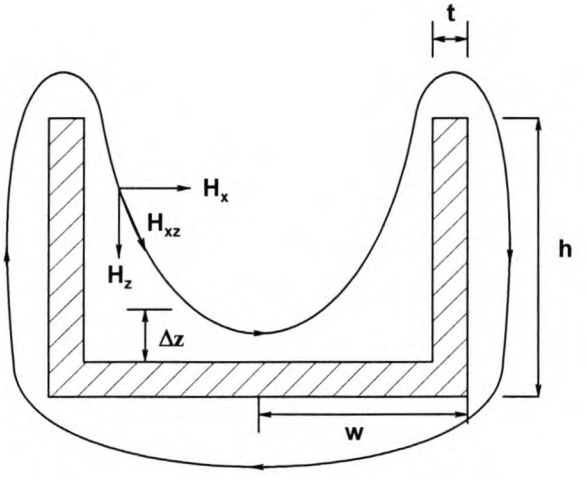

Figure 4.12: *Cross-sectional view of a cable tray to indicate the vector components of the interior H-field.*

The model created in order to determine the S-parameters is in this specific case no longer valid. When the pickup loop is exposed to the B-field, the pickup loop itself conducts current, which in turn generates a B-field, distorting the original field produced by the tray. We are interested in the B-fields in the interior and exterior regions with no conductors

present; the pickup loop can thus be removed. In order to deduce sensible and accurate results, the discretization needs to be adjusted for the calculation of the magnetic field.

The magnetic field in the entire interior region is of interest. Calculations need to be performed as close to the metallic surface as possible in order to maximize the total cross-sectional area to be examined. The only way of achieving this goal is to reduce the mesh size. This gives a good indication of the spatial variation of the current at the floor of the tray. The problem with such an approach is that the number of unknowns increases significantly, which coincides with an increase in computation time and memory resource demand. A solution to this setback is to define a region with fine meshing in the middle of the tray along the *y*-axis at $y = 0$ far away from the closed ends.

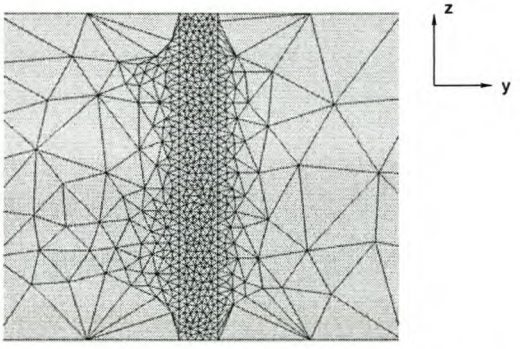

Figure 4.13: *Discretization for the magnetic field calculation.*

Only a small region needs to be defined and the rest of the discretization stays the same as in the *S*-parameter computation. The magnetic field is calculated in Cartesian coordinates throughout the entire cross-section in the *xz*-plane by selecting the *FE* card in *PREFEKO*. Figure 4.13 depicts the meshing implemented in order to calculate the magnetic field interiorly as well as exteriorly as close to the tray surface as possible.

4.13 Shielding effectiveness

Kodali [12] defines shielding effectiveness as:

$$SE_{dB} = 20\log_{10}\left(\frac{H_e}{H_i}\right) \quad [dB] \tag{4.8}$$

The term H_e, represents the field strength without a shield and H_i the field strength with a shield. If we define the field directly below the tray as H_e and the interior field as H_i, we can compare the field strength of the entire inner region to the field directly below the tray. The magnetic near fields are calculated below the tray as well as in the total interior region by applying a source voltage $|V_s| = 50\ V$, and source impedance $Z_s = 50$ ohm at $10\ MHz$. The fields, $4\ mm$ below and $4\ mm$ above the floor of the trays, are plotted in Figure 4.14(a).

The x-axis is normalised to x/w for all trays. The fields below the floor differ slightly in magnitude in the centre and have the same magnitude at the bottom edges. The magnitude of the interior field at $z = 4\ mm$ is smaller for trays with a bigger height-to-width ratio. Figure 4.14(b) depicts the attenuation (SE) of the fields $4\ mm$ above the tray floor. Accordingly, there is a difference in attenuation presented by the different cable trays. The minimum attenuation occurs at the centre of the tray and increases exponentially towards the sidewalls. Table III contains the SE in dB for the four trays at the centre ($x = 0$) and sidewalls ($x = w - 10\ mm$).

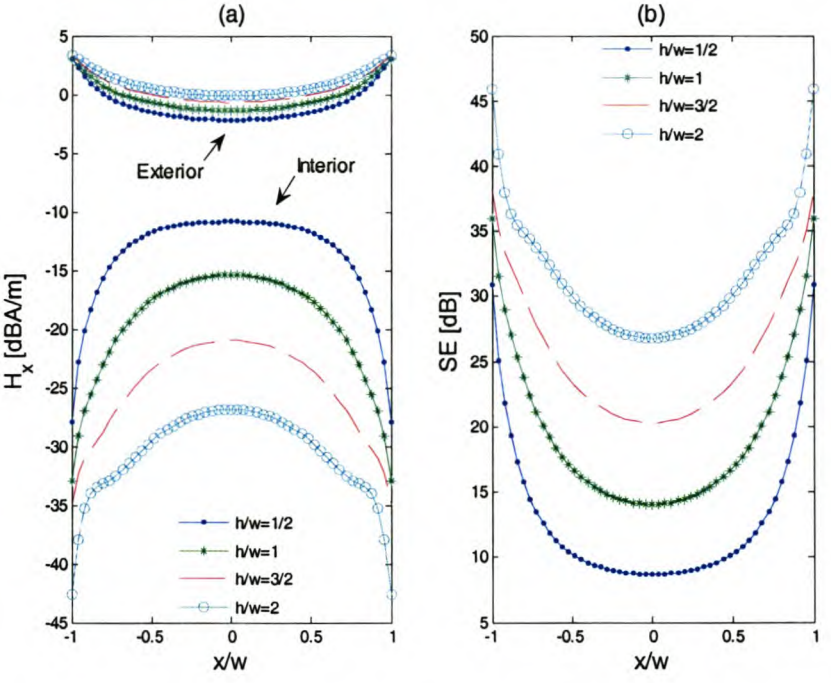

Figure 4.14: *(a) Interior and exterior magnetic fields for four cable trays, of different h/w, at 4 mm below and above the tray floor (b) Shielding effectiveness as defined in equation 4.8.*

Table III: *SE of four cable trays at the centre and sidewalls, 4 mm above the tray floor.*

h/w	*SE [dB] - Centre*	*SE [dB] - Sidewalls*
1/2	*8.7*	*30.9*
1	*14*	*35*
3/2	*20.3*	*38.1*
2	*26.7*	*45.9*

From Figure 4.14 (b) we see that the tray with $h/w = 1/2$ has a *SE* of less than *10 dB* for more than *50%* of the width of the tray. The trays with higher height-to-width ratios attenuate the fields by more than *14 dB* over the entire cross-section above the tray floor at $z = 4$ *mm*. The *SE* in the entire interior region is calculated in the same fashion as described above and is depicted in Figure 4.15. Plots of constant field lines for H_x are displayed in appendix D. It can be seen that the *SE* is a maximum in the bottom inside corners for all trays and increases towards $x = 0$ and $z = h$.

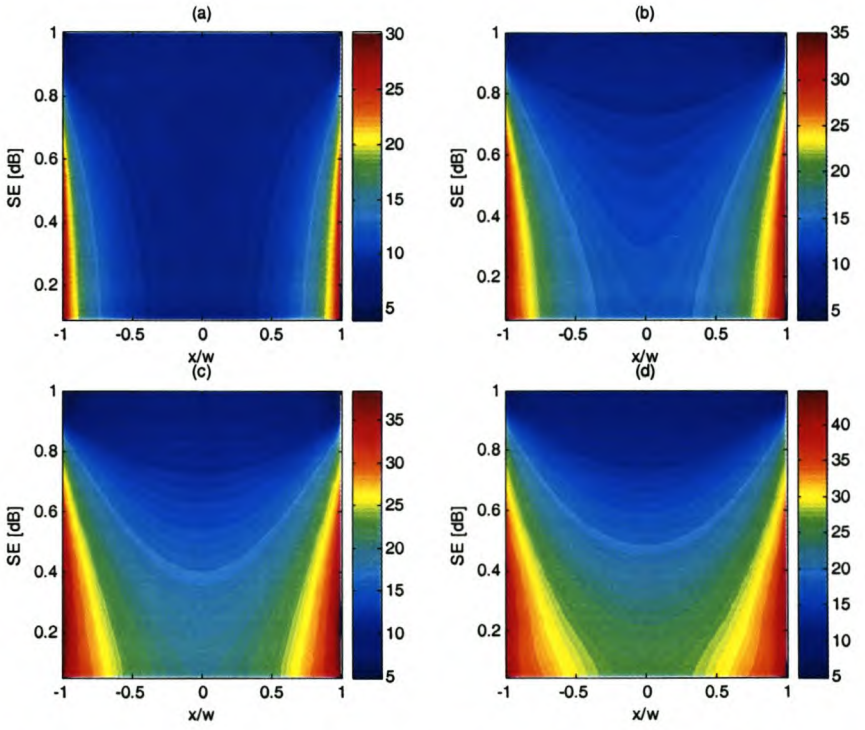

Figure 4.15: *Shielding effectiveness of the four trays (a) h/w = 1/2 (b) h/w = 1 (c) h/w = 3/2 (d) h/w = 2.*

However, cable trays with $h/w > 1$ exhibit a *SE* of more than *10 dB* from *10 %* below the top rim of the tray. It can also be seen that the total cross-sectional area that has a *SE* of *20 dB* or higher increases with an increase in *h/w*.

The magnetic fields are also calculated exteriorly as depicted in Figure 4.16. We can see that the fields are a maximum at the outer top and bottom corner edges. This confirms the theory presented in chapter 3, where the current density decreases at the centre of the tray for frequencies above f_3, and is redistributed towards the edges. The regions where the fields are a maximum indicate where the maximum current flows. Figure 4.15 and 4.16 provide more insight into the shielding mechanism of cable trays. It becomes apparent that the height of the sidewalls determine the total cross-sectional area to be shielded from fields generated by the currents flowing at the bottom edges. Let us assume the currents at the edges are line currents and that the current on the flat surfaces away from the edges are negligible and that the penetration of the *B*-fields into the structure is reduced to a few multiples of a skin depth. The fields generated by a line current decrease with *1/r* as given by equation 2.11. The minimum radius, for the fields generated at the bottom edges, to enter the interior region is equal to the sidewall height (h) of the tray.

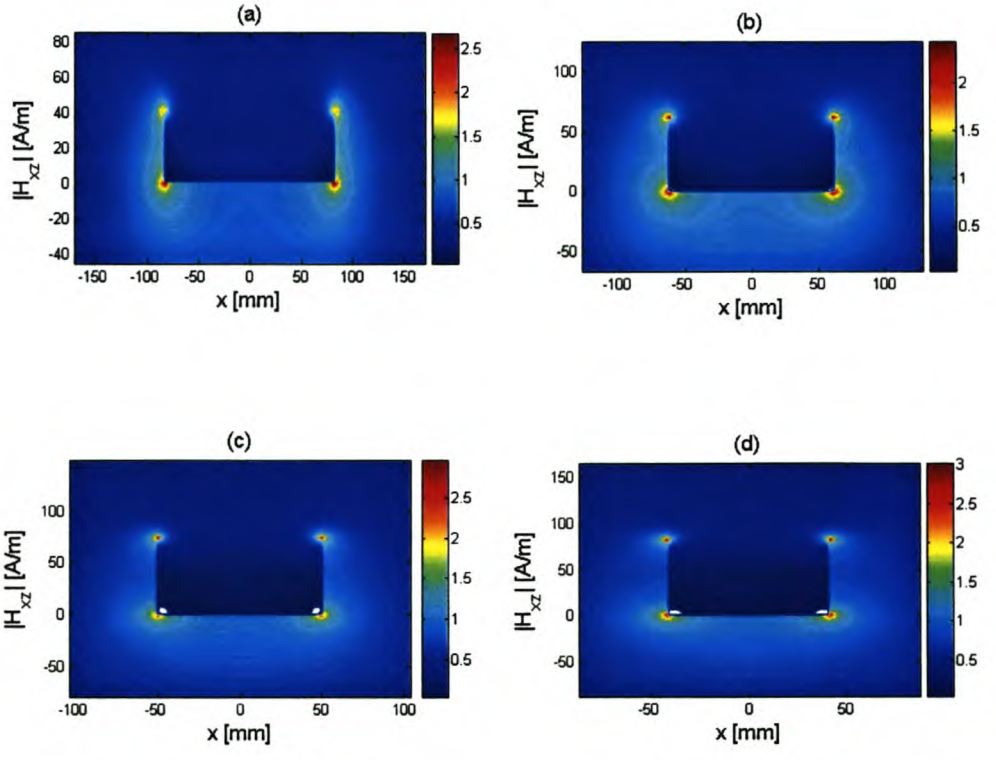

Figure 4.16: *Surface plots of the interior and exterior H_{xz} for the four cable trays (a) h/w = 1/2 (b) h/w = 1 (c) h/w = 3/2 (d) h/w = 2.*

By increasing the height of a tray, the field strength of fields produced by the bottom edges in the interior region of a tray is reduced. When $h/w > 1$, overlapping occurs (Figure

4.17(c)) and the total cross-sectional shielded area increases accordingly. This explains the increase in the total shielded area seen in Figure 4.15.

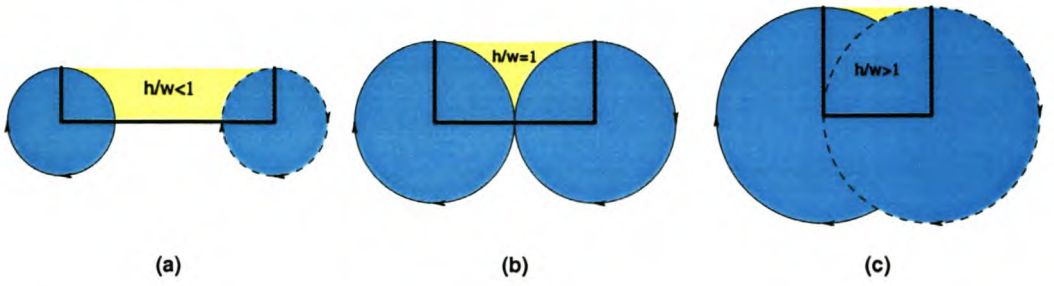

Figure 4.17: *Simplified illustration of the field lines generated by the currents at the bottom edges for (a) h/w < 1 (b) h/w = 1 (c) h/w > 1.*

Shallow trays ($h/w \leq 1$) therefore only have an area close to the sidewalls that are effectively shielded.

4.14 Mutual inductance

Figure 4.18 depicts lines of constant mutual inductance when no conductors are present in the interior region of the four trays. The x and z-axes are normalised.

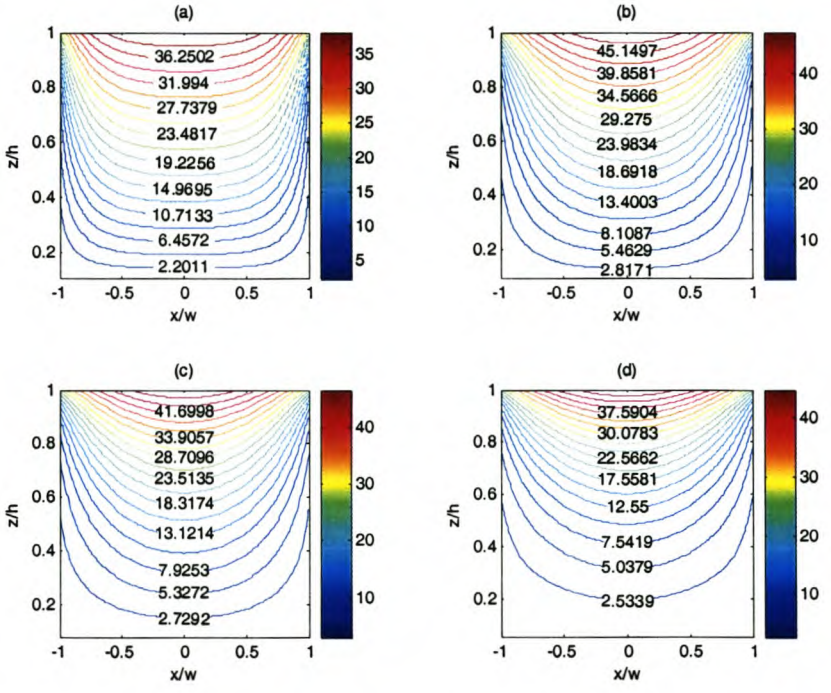

Figure 4.18: *Lines of constant mutual inductance M(x,z) (nH/m); (a) h/w = 1/2 (b) h/w = 1 (c) h/w = 3/2 (d) h/w = 2.*

The mutual inductance is deduced by first calculating the magnitude of the magnetic field in the inner region of the tray with *FEKO®*. Once the magnitude of the numerical x-component of the magnetic field at defined coordinates is calculated, it is processed in *MATLAB®*, with written routines, to acquire M by a trapezoidal integration of the x-component, $H_x(x,z)$, perpendicular to the surface of the floor of the tray. This integration is performed throughout the entire cross-section of the interior region. The following equation was applied in order to calculate M [7]:

$$M(x,z) = \frac{\mu_0 \int_{z_1}^{z_2} \boldsymbol{H}_x(x,z)dz}{I} \quad [H/m] \tag{4.9}$$

The magnitude of I cannot be assumed, as it would result in incorrect results for the mutual inductance M. A source voltage, $|V_s| = 50\ V$, and source impedance $Z_s = 50$ ohm at $10\ MHz$ was defined in *FEKO®*, and it was considered good practice to confirm the magnitude of the injected current $|I|$, because the defined source voltage is an open circuit voltage. The magnitude of the current is calculated with the cable tray included as a load and is depicted by the equivalent circuit in Figure 4.19.

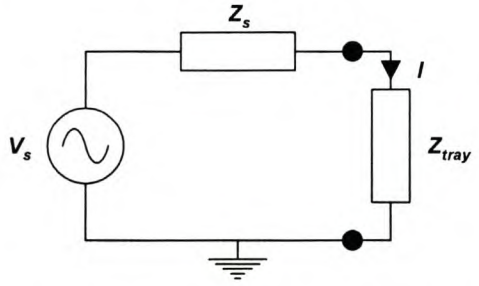

Figure 4.19: *Equivalent circuit of source and cable tray.*

The total current in the circuit is defined as:

$$|I| = \frac{|V_s|}{|Z_{tot}|} = \frac{|V_s|}{|Z_s + Z_{tray}|} \quad [A] \tag{4.10}$$

The current $|I|$ and impedance Z_{tray} were obtained by setting the *OS* control card in *FEKO®*, which allows the calculation of the current through selected wire segments. The

wire segment of the injection wire connected to the cable tray was selected and the calculated currents and cable tray impedances from the *FEKO*® output file appear in Table V. The values of the currents were used in conjunction with equation 4.10 to calculate the mutual inductance and generate plots of constant M throughout the normalised cross-section of all cable trays. The general shape of the contour plots in Figure 4.18 agrees well with the theoretical mutual inductance plotted in Figure 3.6.

Table IV: *Numerically calculated tray impedance and injection current at 10 MHz.*

h/w	Z_{tray} *[ohm]*	*I [A]*
1/2	*0.09 + j50.152*	*0.705*
1	*0.092 + j52.359*	*0.690*
3/2	*0.092 + j54.13*	*0.678*
2	*0.092 + j55.5516*	*0.669*

We assume that the simulated version is the most accurate as the theoretical approach makes use of boundary conditions to calculate M. It is noted anew that the mutual inductance is constant for more than *50%* along the width of a shallow tray ($h/w = 1/2$). This behaviour is not true for trays with a height-to-width ratio $h/w \geq 1$. For deeper trays, the mutual inductance is small over a larger area in the bottom region of a tray. Generally, the mutual inductance increases toward the top rim of a tray and decreases toward the sidewalls. The lines of mutual inductance in Figure 4.18 prove that the mutual inductance M in deeper trays is less than shallow trays and that M is h/w dependant.

4.15 Conclusions

This chapter presented the development of a computational model for cable trays. A two-port network model was developed in order to calculate the S-parameters for four different trays. S-parameters are readily converted to Z-parameters, which gives the ratio of the *DM* voltage to the injected current in terms of Z_{21}, at different xz positions within the tray. The interior and exterior magnetic fields were also calculated for the four trays and compared in terms of shielding effectiveness. Valuable insight was gained concerning the shielding mechanism of a cable tray and the geometrical properties that determine the shielding effectiveness in the interior region within the tray. Lines of constant mutual inductance

were also deduced from the numerically calculated x-component of the magnetic field. The two-port model together with values of M from the data presented in Figure 4.18 can be compared to measurements in order to validate the numerical non-magnetic cable tray model.

Chapter 5

Measurements and Model Validation

5.1 Introduction

Modelling validation in computational electromagnetics can require considerable attention to detail. There are different levels of validation, and care should be taken to understand which level is necessary for a given problem. Validation of a specific software model can occur with the following techniques [12], [13], and [14]:

- Individual Software Code Implementation Validation
- Model validation using measurements
- Model validation using multiple simulation techniques
- Model validation using intermediate results

All techniques have their advantages and disadvantages. Acquiring two or more simulation software packages is expensive and using different packages can be time consuming. Simulation models usually adopt an ideal approach. In other words, parameters like temperature, humidity, reflections, connectors, cables etc. are not always taken into account and imperfections in the real world scenario could render simulation results invalid.

Most often, validation should occur at the specific model level. This ensures that the model correctly represents the important physical parameters for the real-world problem. In addition, not every problem needs to be independently validated. Models are typically validated with a test case, then the model is modified for a number of "what if" cases if the need arises.

One outcome of this project was to measure the transfer impedance of four different cable trays on an ANA, not only for simplicity reasons but also because little or no information is available on the accuracy of results obtained with this technique. Measurements conducted with an *ANA* offer numerous advantages, some include:

- Increased dynamic range
- Measurements are automated over a wide bandwidth
- Simple *S* to *Z*-Parameter conversion

Before measurements are conducted with an *ANA*, it is important to identify the measurement errors, measurement device calibration, circuit, or device under test, test environment, and experimental setup. Therefore, a well thought through measurement procedure should be formulated in order to achieve accurate and repeatable results. The rest of this chapter describes the measurement of the transfer impedance of four different cable trays with *h/w* as described in chapter 4. The measured results are used to compare to the theory and *MoM* simulations.

5.2 Measurement errors

Although an *ANA* is considered a very accurate and trustworthy measurement device, limitations do exist. These arise from errors created internally, by the *ANA*, and externally due to certain factors that influence the repeatability of measurements. Limitations on *ANA* measurement accuracy result from three categories of errors, namely; systematic errors, random errors and drift errors.

Detailed information on these errors can be found in the literature and is not presented here. Systematic errors are compensated for by *ANA* calibration. Calibration, although useful in removing the effects of systematic errors, always results in some residual errors. The magnitude of these residual errors could have an impact on the *DUT/CUT* measurements depending on the magnitude of the *DUT/CUT* parameters, the type of measurement and the extent of the calibration.

Random errors cannot be removed by calibration. Certain techniques to minimize these errors do exist, and are discussed in the sections to follow. Lastly, drift errors are due to the instrument or test system performance after calibration has been performed. These errors can be compensated for by ensuring a stable ambient temperature and additional calibration at regular intervals if required. It is sensible to switch an *ANA* on long before any measurement. This ensures that the device warms up and stabilizes before any measurements are conducted.

5.3 Measurement environment

The measurement environment in which an *EMC* measurement is conducted plays an important role in the accuracy and validity of the measurement. Unwanted external *EMI* from a number of sources can have an influence on results if they fall within the same frequency spectrum in which an experiment is conducted. Due to the nature of this experiment, it was decided to conduct all measurements within a well-characterized and shielded *EMC* chamber (screened room). The chamber consists of a sufficiently thick aluminium wall with a sealable door lined with a copper gasket. As well as for *RF* immunity tests, screened rooms are useful for other *EMC* tests as it establishes a good ground reference plane and an *EM* quiet zone.

5.4 Experimental setup

Figure 5.1 represents the experimental setup devised to determine the transfer impedance of a cable tray. The physical setup of the experiment took place in a screened *EMC* chamber.

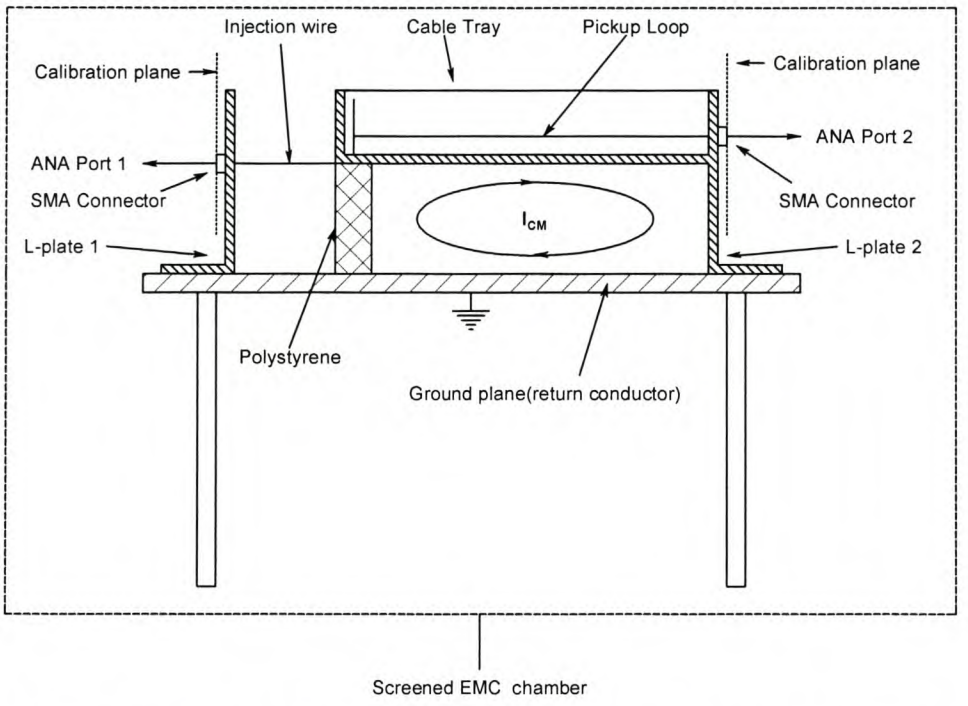

Figure 5.1: *Cross-sectional view of the experimental setup to inject a common mode current into a cable tray with a far away return conductor (tabletop). The differential mode voltage is measured in a shielded EMC-cabinet in order to determine the transfer impedance.*

Current is injected at port 1 and the resulting *DM* voltage measured at port two of an *ANA*. One end of the cable tray is clamped to a table, with a good conducting copper top (return conductor), via *L*-plate 2 as depicted in Figure 5.2.

Figure 5.2: *Photograph of the back end of a cable tray connected to port two of an ANA with a co-axial cable.*

The four cable trays under investigation are constructed by bending the sides of flat brass plates upward. The ends of the trays were closed off by soldering fitted brass plates to the ends. Blocks of polystyrene support the tray at one end as well as the pickup wire along the length of the tray at three intervals. *L*-plate *1* is also tightly clamped to the tabletop (ground plane) to ensure good galvanic contact, as seen in Figure 5.2. Holes were drilled in the end plates to enable the measurement of the magnetic field at different height positions above the centre and sides of the internal region. Figure 5.2 depicts a photograph taken of the experimental setup from the measurement side.

5.4.1 Pickup loop

The pickup loop in Figure 5.1 consists of a *SMA* connector attached to *2 mm* diameter wire, which in turn is terminated in a male Huber and Suhner *MMCX* connector. The male connector has female counter parts, which are soldered to a thin plate at different height positions as depicted in Figure 5.3. Both male and female connectors have a frequency

range of *0 – 6 GHz*. This configuration provides a simple, but effective, method of varying the height of the pickup loop above the tray floor.

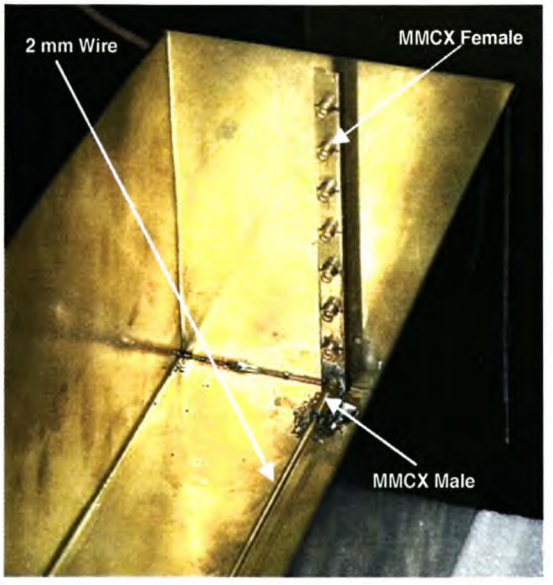

Figure 5.3: *Photograph of the pickup loop terminated in MMCX connectors.*

It also eliminates time consumption if the pickup loop were to be soldered and de-soldered for every measurement. Moreover, it establishes a convenient way to ensure that the same pickup loop can be used for all cable tray measurements. Measurements can also be conducted at the exact same heights above the tray floor.

5.4.2 Injection wire

Little as possible interference to the physical setup should be made to achieve repeatability. The *L*-plate on the left hand side of Figure 5.1 is fixed to a table (ground plane) at all times. It not only serves as mechanical stability but also as a valuable mechanism to divert any *CM* currents that may flow on the cable tray other to the injected current. The only physical aspect of the setup that is changed during measurement is the replacement of the four different cable trays. This is made possible by a male *MMCX* connector soldered to the end of the injection wire. This connector clips into a female *MMCX* connector (Figure 5.4), which is soldered to the bottom centre of the cable tray. This additionally adds to the repeatability of the experiment as the same *L*-plate and injection wire is used for all measurements. The opposite end of the injection wire is soldered to the centre conductor of a *SMA* connector. Both *SMA* connectors illustrated in Figure 5.1 are fitted to the cable tray and *L*-plate via screws.

Figure 5.4: *Photograph of the injection wire.*

5.5 Pre-measurement procedure

Before measurements, certain factors needed consideration to guarantee measurement repeatability. The *ANA* should be switched on prior to calibration to ensure thermal stability and to reduce drift errors. This was done at least *45* minutes before measurements. All cable and *SMA* connectors were cleaned with n-butyl acetate and dried with compressed air before being connected. The connectors were all tightened with a calibrated torque wrench, which contributes to repeatability and prevents over-tightening of connectors.

Measurement cables were orientated in a manner to reduce any stress and any possible mismatches, the same cables were used for every measurement. Mismatches occur if cables are bent excessively, because the centre conductor of the co-axial cable is closer to the outer braid on one side and the characteristic impedance of the cable is altered at this point. The radii of all cables were therefore kept large.

Handling of the cables should also be kept to a minimum to reduce thermal drift. The semi-rigid cables leading to the *SMA* connectors were bent slightly and appropriately aligned to reduce stresses at the calibration planes. The contact points at the *MMCX* connectors were double-checked to confirm good galvanic contact. Co-axial cables can

conduct *CM* currents generated by external sources, which reduce the accuracy of measurements. Therefore, common mode chokes were clipped around all the measurement cables (co-axial and semi-rigid) to observe the response on the *ANA*. A *CM* choke consists of ferromagnetic material and creates a high impedance path for *CM* currents that could enter sensitive instrumentation via the outer braid of a co-axial cable. If the response varies, *CM* currents are present and additional *CM* chokes should be placed around the cables until no change is observed.

No significant response was found, due to the good quality of the cables and the fact that the test setup was inside a protected *EMC* chamber. The clamps were tightened securely to also assure good galvanic contact between the tabletop (return conductor) and *L*-plates. By inspecting all these factors random errors can be reduced, which further contribute to the repeatability and accuracy of the experiment. Systematic errors are removed by calibration of an *ANA*. A full two-port calibration was performed by using known short, open and load standards. The calibration was performed with the following *ANA* settings:

- Calibration start frequency = *300 kHz*
- Calibration stop frequency = *30 MHz*
- Number of points = *201*
- Output Power = *20 dBm*
- Averaging factor = 4, the noise floor improves by $1/\sqrt{Averaging}$
- IF BW = *30 Hz*

By using averaging and setting the *IF BW* to a small number the dynamic range of the *ANA* is increased. The calibration should be checked at regular intervals to confirm that the calibration has not changed. This is done by comparing identical measurements at different time intervals. If a change in magnitude of the *S*-parameters exists, drift has occurred and the *ANA* should be re-calibrated.

5.6 Measurement procedure

With the *ANA* calibration complete, as described in the previous section, the door of the *EMC* chamber is closed and the two-port *S*-parameter set of the system is obtained by

utilizing a *PC* to control the *ANA* via a general purpose interface bus (*GPIB)* and store the *S*-parameter set on a hard drive. Regular checks were made on the state and stability of the calibration as well as the condition off all connectors. The pickup loop was positioned at points *A, B, C, D, E,* and *F* as shown in Figure 5.5 for all four trays. Verification of results obtained from simulations, does not require measurements throughout the whole cross-section.

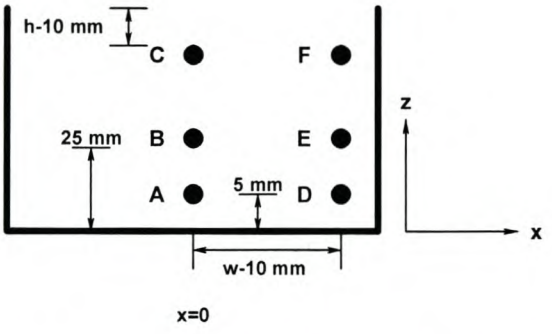

Figure 5.5: *Measurement positions within the cable tray.*

Once the *S*-parameters are acquired, they are transformed to *Z*-parameters to obtain Z_{21}, the transfer impedance at the specific *xz* coordinate where the pickup loop is placed. The following section describes the *S* to *Z*-parameter conversion.

5.7 S-to- Z-parameter conversion

The measured *S*-parameters are converted to *Z*-parameters by applying the following formula [10]:

$$Z = (I - S)^{-1}(I + S)Z_0 \tag{5.1}$$

where *I* is the identity matrix with the same dimensions as the *S*-parameter matrix and Z_0 equals the characteristic impedance of the system and is generally *50 ohm*.

This transformation is performed and plotted with the use of *MATLAB*® in order to compare and interpret the measured and simulated results.

5.8 Measurement and simulation results

Figure 5.6 presents a comparison of the measured and simulated results for the pickup loop at point B for the four trays. We can see that the transfer impedance at a fixed position above the tray floor generally decreases for an increase in height-to-width ratio.

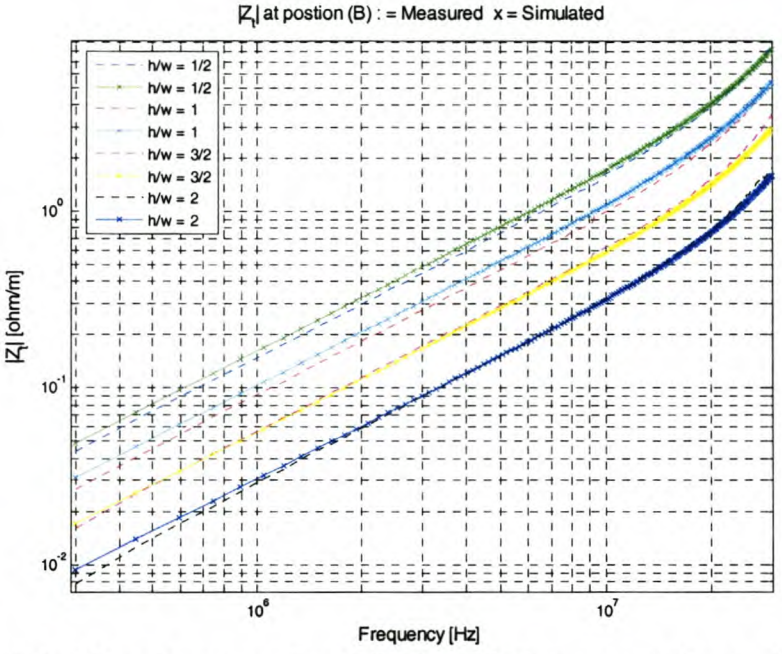

Figure 5.6: *Plot of measured and simulated $|Z_t|$ at point B for the four trays.*

Graphs for the measured and numerical Z_t at points *A, C-F* appear for reference in appendix E as they exhibit similar behaviour. Non-linear behaviour of Z_t is observed for $f > 15$ *MHz*. Even though quasi-static rules were adhered to during the design of the cable trays, the trays are not short enough to support the full measurement frequency range, especially above *15 MHz*. The trays would need to be shortened if a higher frequency limit is sought.

The restriction in making a tray too short is that the total surface area enclosed by the loop and tray floor decreases, which limits the minimum detectable signal at lower frequencies. The induced voltage at port two is a function of *h/w*, the total enclosed surface area between the pickup loop and tray floor, and frequency. There is a trade-off between these factors. However, we are interested in the mutual inductance M at the different positions of the trays in order to form a comparison between the data in Figure 4.18 and the two port numerical and measured data. M can be obtained from the imaginary part of Z_t because the

second part of equation 3.1 is mainly a function frequency and relates directly to M. We can use the magnitude too, as the real part of the Z_t is negligibly small.

In order to calculate the mutual inductance, at the different positions from Z_t, we use:

$$M(x,z) = \frac{\mathrm{Im}[Z_t(x,z,f)]}{2\pi f l} \quad [H/m] \tag{5.2}$$

The values for M, calculated for no wire present, cannot be obtained from the graphs in Figure 4.20 accurately and the data is obtained by accessing the data processed with *MATLAB* manually at the correct coordinates. All values, simulated and measured, for M at positions *A-F* are contained in Table V. Data for the different techniques in Table V agree well, with a maximum error of *55.19%* at point *F* for *h/w = 1/2* and a minimum error of *2.2 %* at point *B* for *h/w = 2*. The errors are discussed in the following section.

Table V: *Measured and simulated mutual inductance M (nH/m) at positions A-F.*

h/w	*Data Type*	*M (nH/m)*					
		Centre (x = 0)			*Side (x = w - 10)*		
		A	*B*	*C*	*D*	*E*	*F*
1/2	*Measured*	6.14	24.01	33.17	1.28	7.31	14.61
	Simulated (wire)	5.32	26.13	36.65	1.82	10.19	17.91
	Simulated (no wire)	5.03	24.73	32.91	1.63	10.91	16.84
1	*Measured*	3.35	14.83	37.91	0.91	3.96	24.39
	Simulated (wire)	3.88	16.66	42.60	1.03	4.71	21.51
	Simulated (no wire)	3.13	14.41	40.84	0.89	4.26	19.65
3/2	*Measured*	1.72	9.31	31.21	0.47	2.58	12.26
	Simulated (wire)	1.75	9.03	36.61	0.64	2.91	18.93
	Simulated (no wire)	1.71	8.21	36.98	0.59	2.76	16.37
2	*Measured*	1.05	4.81	32.45	0.34	1.72	17.08
	Simulated (wire)	0.94	4.89	35.37	0.40	1.82	20.64
	Simulated (no wire)	0.89	4.52	36.18	0.41	1.91	17.95

From the data in Table 4 we confirm that the transfer impedance is smallest in the bottom corners of a tray near the sidewalls (*D*) and largest near the top edge in the centre(*C*).

Values for M at positions *A, B, D, and E* decrease with an increase in h/w. The values for M near the top edge remain constant regardless of the height-to-width ratio. This can be explained by Figure 4.15, it can be seen that the *SE* remains constant above approximately $0.8h$ for all the trays. The total shielded surface area below a line $z = 0.8h$ also increases with an increase in h/w. This can be seen in the good reduction of M for $z < 0.8h$. The data obtained by the technique discussed in section 4.14 correlates well with our measured and simulated data. The lines of constant M in Figure 4.18 are therefore validated and can be used as an accurate approximation when dealing with non-magnetic cable trays with the height-to-width ratios presented here.

Trays with different height-to-with ratios can also accurately be analysed by adjusting the parameters in the *CEM* model. The results obtained illustrate that the transfer impedance $Z_t(x,z)$ is a function of the height-to-width ratio of a cable tray together with the position in the interior region of the tray. The deeper a tray is, the smaller $Z_t(x,z)$ and $M(x,z)$ will be at the same height above the tray as a shallow tray provided that $z \leq 0.8h$.

Table VI compares the theoretical values of M from equation 3.19 with data obtained from simulations.

Table VI: *Theoretical and simulated mutual inductance M (nH/m) at positions A-F.*

h/w	*Data Type*	*M [nH/m]*					
		Centre (x = 0)			*Side (x = w - 10)*		
		A	*B*	*C*	*D*	*E*	*F*
1/2	Simulated	5.03	24.73	32.91	1.63	10.91	16.84
	Theoretical	6.73	34.85	50.53	1.14	5.89	8.53
1	Simulated	3.13	14.41	40.84	0.89	4.26	18.65
	Theoretical	4.09	21.77	60.60	0.92	4.88	13.59
3/2	Simulated	1.71	8.21	36.98	0.59	2.76	16.37
	Theoretical	2.08	11.50	50.16	0.58	3.20	13.99
2	Simulated	0.89	4.52	36.18	0.41	1.91	17.95
	Theoretical	1.04	6.01	46.46	0.34	1.99	15.46

The values for M differ more at positions near the top edges and less closer to the floor. Boundary conditions are imposed in theory and values for M further away from the tray floor will be incorrect. Additionally, theory does not take the spatial distribution of the current into consideration. It is therefore recommended that the engineering expression only be used as an approximation when calculating M close to the tray floor for deep trays ($h/w > 1$).

5.8.1 Measurement Error

Table VII presents the measurement error at the different xz coordinates of the four trays. Models are used to predict reality and therefore we can assume that our measurements represent the correct values. To calculate the percentage mean error, the following equation is used:

$$Mean\ Error(\%) = mean\left[\frac{\left|Z_{t\_measured}(x,z,f) - Z_{t\_simulated}(x,z,f)\right|}{Z_{t\_measured}(x,z,f)}\right] \times 100\% \qquad (5.3)$$

Data from the simulation model is subtracted from the measured data and then divided by the measured data at each frequency point to from a vector. The mean value of this vector is then calculated and expressed as a percentage. We can see that the error is generally larger at the tray floor and bottom corners and becomes smaller as we move towards the top edge of the tray.

Table VII: *Percentage measurement error at points A-F.*

h/w	Error [%]					
	Centre			Sidewall		
	A	B	C	D	E	F
1/2	13.00	9.36	10.99	42.18	40.06	50.58
1	16.35	12.86	12.94	15.07	19.55	11.43
3/2	3.61	2.69	17.84	39.81	13.40	55.19
2	15.39	2.22	9.6	25	7.06	21.44

The large difference in the errors observed can be explained by Figure 5.7. The pickup wire defined in the simulation model is parallel to the floor and sidewalls along the total length of the tray. However, in the practical experimental setup the wire is not rigid and is only supported at three intersections along the length of the tray. The wire bends in both the *x* and *z* directions as it hangs above the floor of the tray.

This means that the distance from the tray floor and sidewalls differs along the length as compared to a constant distance in the simulation model. This deviation in height will influence the total area of the pickup loop. At the floor, the percentage deviation will be greater than at higher positions. If we assume that the height of the wire deviates with dz_1 at the bottom and at higher positions, we can see that the ratio of the surface areas have the following relationship $S_1/(S_1+S_2) > S_1/(S_1+S_3)$.

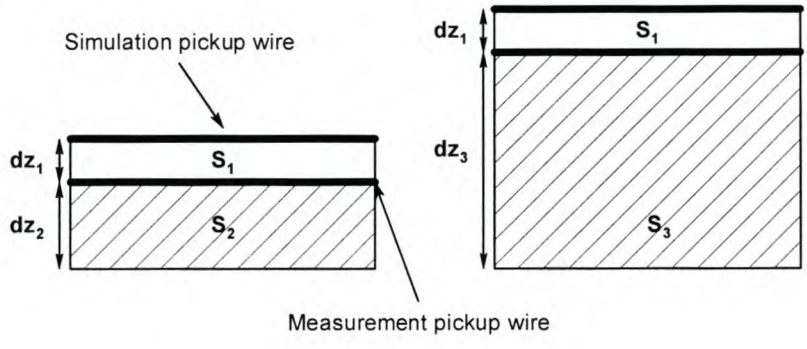

Figure 5.7: *Illustration of practical height variations versus fixed simulation height.*

If the pickup loop is to be positioned *5 mm* above the tray of the floor and the average height is *1 mm* less than specified, the total surface area is reduced by *20 %*, resulting in a smaller induced voltage. However, if the loop is positioned at *25 mm* above the tray floor and a *1mm* difference occurs, the total surface area is only *4 %* smaller.

Therefore, larger measurement errors can occur close to the tray floor. Additionally, we see in Figure 4.18 that the lines of constant mutual inductance tend to concentrate at the top part of a tray. This is because we move closer to the non-shielded area. If the positioning of the pickup wire at distances close to the rim varies slightly, large errors may result. Collectively, this explains the large differences in error at the top and bottom. The

pickup loop is thus the main factor that influences the repeatability of our measurement scheme.

5.9 Conclusions

The transfer impedance of non-magnetic cable trays have been measured and compared against its numerically calculated counterpart. The results agree well and the maximum errors are well within indicated tolerable limits. We have seen that the transfer impedance decreases with an increase in h/w, which proves that deep trays ($h/w > 1$) have better shielding characteristics than shallow trays. Not only does h/w influence Z_t, but also the xz position within a cable tray. The minimum transfer impedance is in the bottom corners whereas the maximum is at the top of the tray at $x = 0$ and $z = h$. The computational model has been validated by data obtained from measurements and can be applied to any non-magnetic cable tray with a specified height-to-width-ratio.

Chapter 6

Cable Tray Installation Guidelines

6.1 Introduction

The preceding chapters equip us with the necessary knowledge and insight to formulate general practical cable tray and cable installation guidelines. Holes or slots are often made in cable trays to enable easy attachment of cables and to secure the trays to mechanical support structures like metal beams or concrete walls. It is therefore important to know where and how these slots or holes can be made. Additionally, placement of cables within the tray is another important factor to consider. Most often cables responsible for transporting different signals are present within the same environment. Cable placement within a cable tray will differ according to the amount of shielding required. The following sections highlight the most important factors to be considered and applied when installing cable trays and cables.

6.2 Slot and hole positions

As mentioned previously, cable trays often have holes or slots present in order to ensure easy attachment of cables. Figure 6.1 illustrates a cable tray with several slots of different dimensions and orientations with respect to a cable tray.

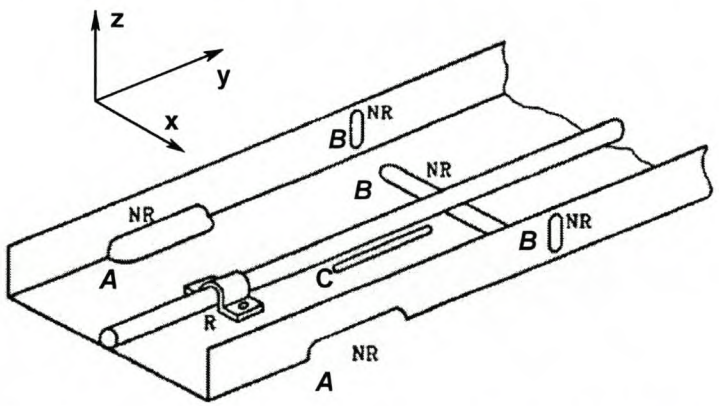

Figure 6.1: *Possible slot and hole positions and orientations in a cable tray (after [6]).*

In chapter 4 we noted that the magnitude of the current is a maximum at the outer top and bottom edges. Long slots, parallel to the *y*-axis, in the corners should be avoided as indicated by *A* in Figure 6.1. The magnetic field will enter the internal region of the tray and couple to the closed surfaces formed by cables and the tray floor. Cables can also be attached to the floor with clamps that are securely screwed to the tray via small holes.

Slots perpendicular to the *y*-axis are not recommended, as slots of this nature would distort the current flow and produce strong coupling through the openings. Figure 6.2 illustrates this principle. When a slot perpendicular to the *y*-axis is present, the current flowing perpendicular to the slot has to find an alternative route. This route would normally be out toward the edges and back towards it normal path again. The total current around the edges denoted *B* would be greater than the current at edges *C* as depicted in Figure 6.2.

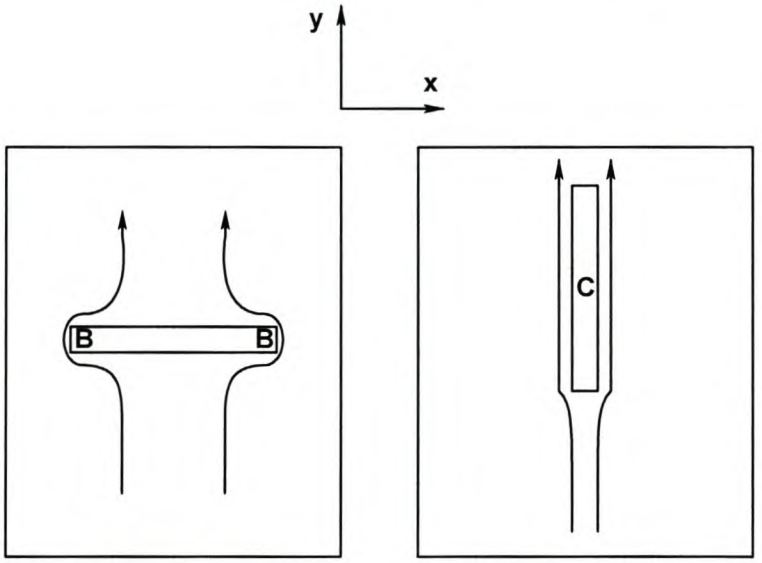

Figure 6.2: *Current paths around slots.*

In the first case, *B*, the magnitude of the current is larger at the small edges parallel to the *y*-axis but the surface area, along the length of the tray, threaded by the magnetic field generated by this current is small. The direct opposite is true for currents flowing around the edges at *C*, where the magnitude is smaller, but the total surface area threaded by the magnetic field is large. Therefore, if slots with these properties need to be made, it should be some distance from cables in the tray, and their dimensions should be kept to a minimum. The most suitable position for a slit parallel to the *y*-axis, in the tray floor,

would be in the centre of the tray at $x = 0$, where the magnitude of the current on the outside edge is a minimum.

6.3 Cable tray length

A cable tray should form a continuous metallic structure over its entire length. If a tray is constructed using several shorter parts, care should be taken to ensure this continuity by correct bonding between the different parts. The cross-sections should overlap and be soldered or riveted together across the entire cross-section in order to eliminate any current from leaking into the interior region. These contact surfaces should additionally be free of any non-conducting material and treated accordingly to prevent corrosion.

A cable tray serves as a shield by diverting unwanted *CM* currents away from sensitive cables in the interior and the flow of current is only possible if there is a closed loop. Cables are connected between instrumentation and cabinets. It is thus imperative to ensure that the ends of the tray are connected to the cabinet over its entire cross-section and well grounded at both ends to establish a closed loop.

If one end is left open, parasitic capacitances could close the loop at high frequencies as discussed previously in Figure 2.7(c). These capacitances may resonate with the self-inductance of the *CM* loop at certain frequencies and cause large currents and *DM* voltages over the terminals of the load. Besides this essential point, if the ends are not securely grounded the shielding efficiency may be rendered useless. If a short, single pigtail is used as a connection point at the ends, a local high Z_t is produced which degrades the overall *EMC* performance for all cables in a tray and is not recommended.

The length of cable trays can be very long and since the transfer impedance is a per metre quantity, it would make sense to keep the distance between ports to a minimum. For long distances, additional connections of the tray to the grounding system are recommended at regular intervals between apparatus [6]. These extra connections provide an early return path for *CM* currents. Moreover, these connections should be made on the outside of the tray to preserve the separation from the interior region.

6.4 Distance between cable trays

Several cable trays can be stacked together and may run parallel over a certain distance. The *DM – DM* cross talk between the trays may become important [6]. The recommended distance between the trays depends on two factors, first on their quality as a *PEC* with a low Z_t in mind. Secondly, on the *DM – DM* cross talk between the trays.

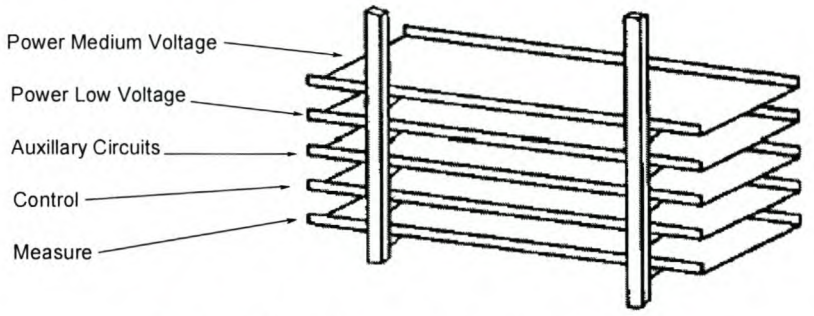

Figure 6.3: *Cable tray stacking (after [6]).*

Van Deursen [6] suggests the stacking order for cable trays as depicted in Figure 6.3. If shallow (*h/w < 1*) trays are used, the distance between the trays should be a certain minimum distance. The separation distance between the trays would reduce the *DM-DM* cross talk between them. Distances between different trays should be at least *0.15* metres in the vertical as well as horizontal directions [6]. Trays containing sensitive measuring cables should be covered when it is at a distance of less than *1* metre from the high-current power cables. Trays stacked together should be electrically connected at the vertical supports as seen in Figure 6.3. Sensitive cables are carried in trays closest to ground. This would ensure that the surface exposed to *B*-fields would be smaller.

Cables of different categories should never be bundled together and each category should be placed in its own cable tray. Van Deursen [6] differentiates between the following cable categories:

- Very sensitive: Cable that carries low-voltage or low current signals from sensors
- Sensitive: Signal cable with *V <= 24 V*, or flat cable for parallel data transfer
- Indifferent: *AC* power(*230 V*), depending on the *EMC* properties of apparatus connected

- Noisy: *AC* and *DC* relay feed line without protection measures as filters or diodes
- Very noisy: Leads to *DC* motor with brushes, switched power lines, cables and earth wires in high-voltage switchyard etc

Cables can have their own shield, for instance the co-axial cable. If no shield is present, it should be ensured that these cables have a distance of at least ten times the largest lead cross-section between them. Braided shields seldom provide protection at powerline frequencies, and should be placed in a cable tray to ensure protection. The wall thickness of such a tray becomes important as it influences the crossover frequency from *DC* to *HF*.

6.5 Cable placement within a cable tray

From the simulations presented in chapter 4 and the measurements in chapter 5, the most obvious position for a cable with in a tray would be in the two bottom corners. At the floor of the tray, the surface area exposed to a *B*-field is small and the *x*-component of the *B*-field ceases to exist at the walls of a tray.

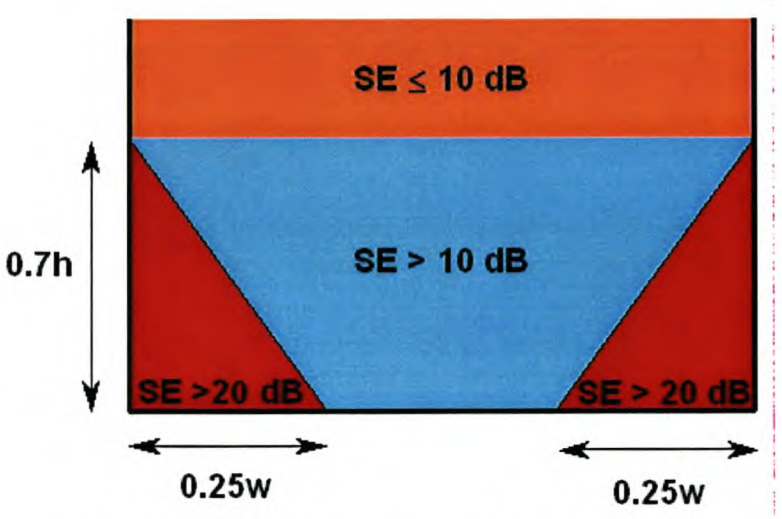

Figure 6.4: *Areas within the cross-section of a cable tray and the minimum attenuation with a tray h/w = 1 as reference.*

With Figure 4.15 as reference, we can draw a generalized cross-section of a cable tray and indicate the areas where the attenuation is below or above certain values. For effective shielding, it is recommended to use cable trays with a height-to-width ratio *h/w > 1*. If we use Figure 4.15(b) as reference, four main areas with similar characteristics become

evident. The triangular areas in red are the regions where the *SE* is a maximum with a minimum value of *20 dB* attenuation below the diagonal line. The *SE* increases toward the sidewalls and tray floor. The blue parallelogram indicates an area where the *SE* is a minimum of *10 dB* below the horizontal line, *0.7h* from the top rim, and *20 dB* above the diagonal lines.

The height *0.7h* seems to be universal for all the cable trays analysed. Note that the values of *SE* are exact for a cable tray with *h/w = 1*. These figures will increase with an increase in *h/w*. The orange area indicates the region where the *SE* is below *10 dB*. This makes sense, as it is high above the tray floor and near the top edges where current flows. Cables should not be stacked higher than *0.7h* within the cable tray. The safest positions are near the bottom corners and the area indicated in blue. If cables transporting different signals have to be accommodated in the same cable tray, the most sensitive cables should be placed in the regions indicated in red and the less sensitive cables in the blue area. As mentioned before, it is not recommended to place cables of different categories in the same tray.

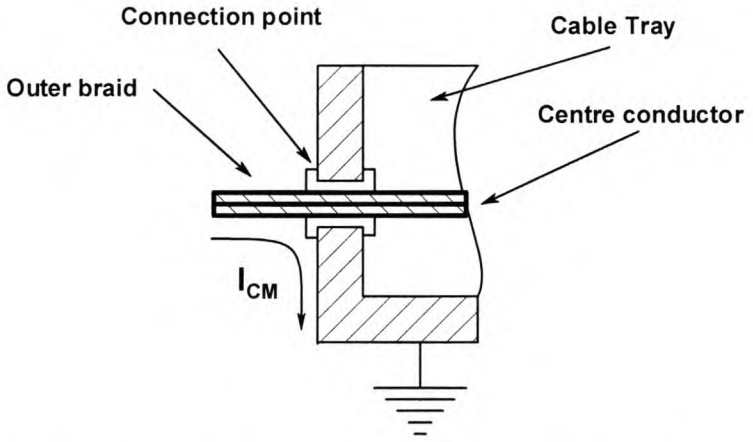

Figure 6.5: *Cable entrance point into a tray should consist of a good connection in order to divert CM currents flowing on the outer braid of a co-axial cable away from the interior region of the tray.*

All shields and other *PEC's* that enter a cable tray should be properly connected to the tray at its point of entrance as depicted in Figure 6.5. This would allow an exchange of *CM* currents between the tray and cables. Because the arriving *CM* current flows in a circuit

closing outside the tray, this current tends to flow on the outside rather than enter the interior of the cable tray, as seen in Figure 6.5.

Chapter 7

Conclusions and Recommendations

7.1 Conclusions

This thesis presented the development of a numerical model and measurement scheme in order to determine the transfer impedance of non-magnetic cable trays. The numerical results are in good agreement with measurements. The theory presented by [1] is only accurate within a certain region inside a cable tray and based on certain approximations. Z_t is mainly a function of M at HF and equal to the DC resistance at LF. The transfer impedance and mutual inductance within the interior region of a cable tray increases from bottom to top and from the sidewalls toward the centre. The numerical model developed in this thesis can be applied to any U-shaped cable tray in order to determine the transfer impedance at a certain xz position in the cross-section.

The transfer impedance is mainly a function of the mutual inductance at high frequencies and the transfer impedance is mainly a function of the height-to-width ratio and not material properties at HF. Trays with $h/w > 1$ offer better shielding characteristics than shallow trays. If sensitive cables were to be placed in a cable tray, the bottom corners would be best suited for optimal shielding. Current flow is a maximum at the bottom and top corners of a tray at HF and certain rules need to be adhered to when installing cable trays as discussed in chapter 6.

7.2 Recommendations

The model developed in this thesis applies to non-magnetic cable trays. However, the CEM model can easily be adapted to include a relative permeability of greater than one. Magnetic cable trays can therefore also be modelled and the transfer impedance measured. The advantage of magnetic cable trays is that shielding can be implemented at low frequencies. The shielding effectiveness of magnetic cable trays should be better than non-magnetic trays and this could be investigated.

Cables are placed in the interior region of a cable tray. The stacking order of cables could influence the transfer impedance and the numbers obtained in chapter 5 could possibly change. It is therefore recommended that simulations and measurements be conducted in order to determine the change in transfer impedance when several conductors are present within a cable tray.

Cable trays do not always form a continuous structure over its length and interconnects exist to connect the different sections of the tray together. The influence on the transfer impedance by these interconnections could also be studied and verified to propose a suggested topology for these connections. The redistribution of the current toward the edges could additionally be verified by designing a magnetic field probe to measure the magnetic field on the outside surface of the cable tray.

The sensitivity of Z_t for variations in the measured and simulated S-parameters can also be investigated. Lastly, the effect of the terminal boundaries on Z_t can be investigated by implementing a shorter pickup loop inside a longer tray with end plates.

Bibliography

[1] M.J.A.M. van Helvoort, "*Grounding structures for the EMC protection of cabling and wiring*", "Universiteits Drukkerij, Technicshe Universiteit Eindhoven", November 1995.

[2] A.P.J van Deursen, FBM van Horck, MJAM van Helvoort, PCT van der Laan, "*Transfer Impedance of Non-magnetic Conduits of Various Shapes*", IEEE Transactions on Electromagnetic Compatibility, Vol. 43, No1, February 2001.

[3] M.J.A.M van Helvoort, A.P.J van Deursen, PCT van der Laan, "*The Transfer Impedance of cables with a return conductor and a noncentral inner conductor*", IEEE Transactions on Electromagnetic Compatibility, Vol. 37, No. 2, May 1995.

[4] Frederick M. Tesche, Michel V. Ianoz and Torbjorn Karlsson,"*EMC Analysis Methods and Computational Models*", John Wiley & Sons Inc., 1997.

[5] Kenneth L. Kaiser, "*Electromagnetic Compatibility Handbook*", CRC Press, 2005.

[6] A.P.J van Deursen, "*Electromagnetic compatibility Part 5, Installation and mitigation guidelines. Section 3, Cabling and wiring*", Research Report, Eindhoven University of Technology, July 1993.

[7] Herman A. Haus, James R. Melcher, "*Electromagnetic Fields and Energy, Volume 1*", Prentice-Hall Inc., 1989.

[8] Herman A. Haus, James R. Melcher, "*Electromagnetic Fields and Energy, Volume 2*", Prentice-Hall Inc., 1989.

[9] FEKO® user manual.

[10] D.M. Pozar, "*Microwave Engineering*", John Wiley & Sons Inc., 2nd edition, 1998.

[11] V. Prasad Kodali, "*Engineering Electromagnetic Compatibility: Principles, Measurements, and Technologies*", IEEE Press, 1996.

[12] Heinz D. Brüns, Herman L. Singer, "*Validation of MoM Simulation Results*", IEEE Symposium on Electromagnetic Compatibility, Boston, August 18-22, 2003.

[13] Bruce Archambeault, "*Concerns and Approaches for Accurate EMC simulation Validation*", IEEE Symposium on Electromagnetic Compatibility, Boston, August 18-22, 2003.

[14] Andrew L. Drozd, "*Progress on the Development of Standards and Recommended Practices for CEM Computer Modelling and Code Validation*", IEEE Symposium on Electromagnetic Compatibility, Boston, August 18-22, 2003.

Appendix A

Skin depth of metals relative to copper

If the formula for the sin depth is given as:

$$\delta = \frac{66.1 \times k}{\sqrt{f}} \tag{A.1}$$

where k is a function of the material with copper as the reference $k=1$. Table A.1 contains values for several metals.

Table A.1: Skin depth of metals referred to Copper as reference

Material	*k*
Aluminium	*1.26*
Copper	*1*
Lead	*3.52*
Silver	*0.94*
Tin	*2.55*
Tungsten	*1.76*
Brass	*1.99 (Depends on alloy)*
Phos-bronze	*2.1*
Bronze	*3.1*

Appendix B

Cable Tray Transfer Impedance Derivation

B.1 DC approximation [1]

At low frequencies, the current distribution in a tray is homogenous. For non-magnetic trays ($\mu_r = 1$) the magnetic field cab be calculated with a superposition of the vector potential $\boldsymbol{B} = \nabla \times \boldsymbol{A}$ contributions from an infinite number of line currents i. If an infinitely long tray is considered over which a current in the y-direction is flowing the problem reduces to two dimensions: $\boldsymbol{A}$ has only a y-component. For each line current i one obtains:

$$A_y = \frac{\mu_0}{2\pi} i \ln(r) \tag{B.1}$$

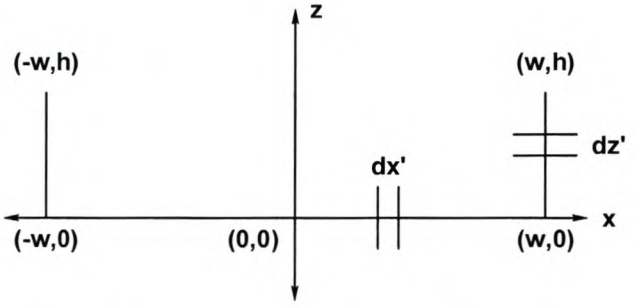

Figure B.1: *Two-dimensional representation of geometric parameters to determine the magnetic field inside a cable tray with height = h and width = w*

We can further simplify the calculation because we consider the thickness of the metal much smaller than its width. The current can now be approximated by a sheet current. With a total current I through the tray the small line current dI (Figure B.1) through a narrow strip with width dx' (or dz') is:

$$dI = \begin{cases} \dfrac{I_{cm}}{2(h+w)} dx' & \text{for tray floor} \\ \dfrac{I_{cm}}{2(h+w)} dz' & \text{for side walls} \end{cases} \tag{B.2}$$

With the geometrical parameters give in Figure B.1 the vector potential at point (x,z) can be calculated as:

$$A_y(x,z) = \frac{u_0 I_{cm}}{8\pi(h+w)} \left\{ \int_{-w}^{w} \ln((x'-x)^2 + z^2)dx' + \int_{0}^{h} \ln((-w-x)^2 + (z'-z)^2)dz' + \int_{0}^{h} \ln((w-x)^2 + (z'-z)^2)dz' \right\} \quad \text{(B.3)}$$

The integrals in equation B.3 can be found in standard integral tables or are solved analytically by an algebraic computer program. The magnetic field can be derived from A_y. For the x-component, one finds:

$$H_x(x,z) = \frac{1}{u_0}\frac{\partial A}{\partial z} = \frac{I_{cm}}{8\pi(h+w)} \left\{ 2\tan^{-1}\left(\frac{x+w}{z}\right) - 2\tan^{-1}\left(\frac{x-w}{z}\right) - \ln\left[\frac{(x+w)^2 + (z-h)^2}{(x+w)^2 + z^2}\right] - \ln\left[\frac{(x-w)^2 + (z-h)^2}{(x-w)^2 + z^2}\right] \right\} \quad \text{(B.4)}$$

To find the H_x-field at (0,0), just above the metal, we substitute $x = 0$ and calculate $\lim_{y\to 0} H_x$:

$$H_x(0,0) = \frac{I_{cm}}{4(h+w)} + \frac{I_{cm}}{4\pi(h+w)} \ln\left(\frac{w^2}{w^2+h^2}\right) \quad \text{(B.5)}$$

The flux through the loop formed by the conductor above the central line of the tray at a height Δz is given by:

$$\Phi = \mu_0 \lim_{a \to 0} \int_{a}^{\Delta z} H_x(0,z')dz' \approx \mu_0 H_x(0,0)\Delta z \quad \text{(B.6)}$$

For trays with $h/w \leq 2$ the latter approximation is valid to within *10%* for $\Delta y \leq (h+w)/10$ [1].

For low frequencies $H_{x,DC}(0,0)$ is:

$$H_{x,DC}(0,0) = \frac{I_{CM}}{4(h+w)}\left\{1-\frac{1}{\pi}\ln(1+(\frac{h}{w})^2)\right\} \tag{B.7}$$

For low frequencies, the transfer impedance then becomes:

$$Z_t(0,\Delta z) = \frac{1}{2\sigma(h+w)t} + j\omega\frac{\Delta z}{4(h+w)}\left\{1-\frac{1}{\pi}\ln[1+(\frac{h}{w})^2]\right\} \tag{B.8}$$

The second term in equation B.8 is negligible at *LF* and B.8 reduces to:

$$Z_t(0,\Delta z) = \frac{1}{2\sigma(h+w)t} \tag{B.9}$$

The transfer impedance above the central line of the tray is equal to the DC resistance of the tray.

B.2 High frequency approximation [1]

At high frequencies ($\delta << t$), the skin depth is small compared to the thickness of the tray. For $f > f_3$ it is sufficient to assume surface currents on the tray floor and sidewalls. The magnetic fields outside any metallic regions can then be calculated by solving the scalar Laplace equation in two dimensions [1]:

$$\nabla^2\varphi(x,z) = \frac{\partial^2\varphi(x,z)}{\partial x^2} + \frac{\partial^2\varphi(x,z)}{\partial z^2} = 0 \tag{B.10}$$

If $\varphi(x,z) = X(x)Z(z)$, thus a function of x and z, and substituted into B.10 gives:

$$Z(z)\frac{\partial^2 X(x)}{\partial x^2}+X(x)\frac{\partial^2 Z(z)}{\partial z^2}=0 \tag{B.11}$$

By dividing equation B.9 through with *X(x)Z(z)* the following equation arises which can be solved by separation of variables.

$$\frac{1}{X(x)}\frac{\partial^2 X(x)}{\partial x^2}+\frac{1}{Z(z)}\frac{\partial^2 Z(z)}{\partial z^2}=\frac{X''}{X}+\frac{Z''}{Z}=0 \tag{B.12}$$

$$\frac{X''}{X}=-\frac{Z''}{Z}=-\alpha^2 \tag{B.13}$$

Two differential equations are extracted from equation B.9 that needs to be solved. The equations have the form as given in equations B.14a-B.14b

$$X''+\alpha^2 X=0 \tag{B.14a}$$

$$Z''-\alpha^2 Z=0 \tag{B.14b}$$

The solutions to equations B.14a-B.14b are given as:

$$X=c_1\sin(\alpha x)+c_2\cos(\alpha x) \tag{B.15a}$$

$$Z=c_3\sinh(\alpha z)+c_4\cosh(\alpha z) \tag{B.15b}$$

In order to solve coefficients c_1, c_2, c_3 *and* c_4, the boundary conditions are imposed on the rectangular area as depicted in Figure B.1. The magnetic field is under investigation in the two-dimensional region within the rectangular area. The boundary conditions are implemented at the floor of the tray where $z = 0$ and at $x = w, -w$ where the two sides of the tray exist.

At $z = 0$, the following condition is true:

$$H_z=0 \quad\Rightarrow\quad \left.\frac{d\varphi}{dz}\right|_{z=0}=0 \quad\Rightarrow\quad c_3=0 \tag{B.16}$$

At the sidewalls:

$$H_x = 0 \quad \Rightarrow \quad \left.\frac{d\varphi}{dx}\right|_{x=w,-w} = 0 \quad \Rightarrow \quad c_2 = 0 \tag{B.17}$$

The solution to B.10 is:

$$\varphi(x,z) = \sum_{n=1}^{\infty} C_n \cosh\left(\frac{\pi(2n-1)}{2w} z\right) \sin\left(\frac{\pi(2n-1)}{2w} x\right) \tag{B.18}$$

and $m = \dfrac{\pi(2n-1)}{2w}$, $with\ n = 1, 2.....$

The magnetic field is determined by $\boldsymbol{H} = \nabla\varphi$ and given by [1] as:

$$H_x(x,z) = \frac{\pi C_1}{2w} \cosh\left(\frac{\pi z}{2w}\right) \cos\left(\frac{\pi x}{2w}\right) \tag{B.19}$$

Equation B.19 contains a coefficient C_1, this number is cumbersome to determine, as it is a function of the shape of the tray and consequently the height-width ratio. C_1 can be rewritten as a function of the common mode current (I_{cm}) and a shape factor (γ) equation B.19 then becomes:

$$H_x(x,z) = \frac{\gamma\pi I_{cm}}{2w} \cosh\left(\frac{\pi z}{2w}\right) \cos\left(\frac{\pi x}{2w}\right) \quad for\ y \le y_c = h - 0.8w \tag{B.20}$$

$$Z_t(x,z) = \frac{g \cos(\frac{\pi x}{2w}) \left\{ \frac{k}{\sigma} + j\omega\mu_0 \frac{2w}{\pi} \sinh(\frac{\pi z}{2w}) \right\}}{2\pi(h+w)} \tag{B.21}$$

Appendix C

PREFEKO® Simulation Code

C.1 Magnetic field calculation

```
** This file calculates the magnetic field in the interior
** region of a cable tray

** Creator of file: N.W.Ebertsohn
** Date created: 2004
** Date last edited: 20-04-2005

** Define Variables
**   Optional scaling factor (e.g. set to 0.001 if all geometrical
**   coordinates etc. are to be defined in mm instead of metres)
#scaling = 1e-3
**   Frequency and wavelength
#freq = 30e6          ** frequency in Hertz
#lam = #c0/#freq      ** wavelength in metre,  #c0 = speed of light in vacuum
#lam = #lam/#scaling  ** scale the wavelength as desired (e.g. to mm)

**   Other user defined variables
#csl=250                  ** Total cross-sectional length
#hw=2                     ** Height-width ratio
#w=#csl/(2*#hw+2)         ** Width
#h = #hw*#w               ** Height
#or = 200                 ** Origin
#l = 100                  ** Length of tray
#dy1= 8                   ** Height of pickup loop above tray floor
#dy=5
#t = 0.56           ** Thickness of metal (skin effect)
#fmin = 10          ** Minimum frequency (Start)
#fmax = 30e6        ** Maximum frequency (Stop)
#nf= 200            ** Number of frequency points
#sig = 1.45e7       ** Metal Conductivity
#wl=100             ** Injection wire length
#y0 = 0
#hf = #y0+5

** Parameters for segmentation
#seg_r = 1        ** radius of the wire segments
#seg_l = 1.5*#dy1  ** maximum length of wire segments
#tri_l = 2*#dy1    ** maximum edge length for triangular patches

#tL0 = min(#lam/30,#w/2)
```

```
#sL0 = #tL0
#tL1 = min(#lam/30,3*#dy1)
#sL1 = #tL1

IP                  #seg_r   #tL1     #sL0
** Geometry of radiating structure
** A FEMAP model may be included with the IN card
** IN   1  3  "filename.ext"

** Define points for cable tray structure
DP  CT1             0        #l/2     #or
DP  CT2             #w       #l/2     #or
DP  CT3             0        #hf      #or
DP  CT4             #w       #hf      #or
DP  CT5             0        -#hf     #or
DP  CT6             #w       -#hf     #or
DP  CT7             0        -#l/2    #or
DP  CT8             #w       -#l/2    #or
DP  CT9             0        #l/2     #or+#h
DP  CT10            #w       #l/2     #or+#h
DP  CT11            #w       #hf      #or+#h
DP  CT12            #w       -#hf     #or+#h
DP  CT13            #w       -#l/2    #or+#h
DP  CT14            0        -#l/2    #or+#h
DP  CT15            0        -#l/2    0
DP  CT16            #w       -#l/2    0

** Define Points for injection wire
DP  SW1             0        #l/2+#wl  0
DP  SW2             0        #l/2+#wl  #or
DP  SW3             0        #l/2+80   #or

** Cable Tray
LA  1
PM  CT1  CT2  CT4  CT3
2
PM  CT5  CT6  CT8  CT7                                                    2
PM  CT1  CT9  CT10 CT2
PM  CT10 CT2  CT4  CT11
2
PM  CT12 CT6  CT8  CT13                                                    2
PM  CT14 CT7  CT8  CT13
PM  CT15 CT16 CT8  CT7

IP                  #seg_r   2        #sL0
LA  2
PM  CT3  CT4  CT6  CT5                                                    2
2
PM  CT4  CT11 CT12 CT6                                                    2
2
```

```
SY  1   3   0   0
** Create wire segment for source 1 (Port 1)
LA  3
BL  SW2 SW3

LA  4
BL  SW1 SW2
BL  SW3 CT1

** Apply the scaling factor
SF  1                   #scaling
** End of geometric input

EG  1   0   0   0   0

** Create a PEC (Perfect Electric Conducting) Ground Plane
BO  2                   1       0       1       0       0

** Define skin effect for metal plate and wires

** Set the frequency point for simulation
FR  #nf 0               #fmin           #fmax

** Optional loading of segments
LS  3                   50      0       0

** Source 1 (Port 1)
A1  0   3               50      0                               50

** Skin Effect
SK  1   3               #t      1       #sig
SK  2   3               #t      1       #sig
SK  3   3                       1       #sig
SK  4   3                       1       #sig

** Format of output files
DA  0   0   0   0   0   1

** Surface currents for display
** OS  1       1

** Magnetic field inside the tray

#x1 = -#w+2   ** start x
#x0 = #w-2    ** stop x
#nx = 71 ** number of x points
#dx = (#x0-#x1)/(#nx-1) ** x increment


#z1 = #or+1 ** start z
```

```
#z0 = #or+5 ** stop z

#nz = 11 ** number of z points
#dz = (#z0-#z1)/(#nz-1) ** z increment

#ny = 1 ** number of y points
#dy = 1 ** y increment

** Calculate the magnetic near field
FE  2   1   1   1   0   0       0       #or+1    1       1       1

** End of file
EN
```

C.2 S-parameter calculation (centre)

```
** This file attempts to simulate the S-parameters of a
** cable tray in order to determine it's shielding effectiveness
** SE. The height-width ratio can be changed according
** to specification.

** Creator of file: N.W.Ebertsohn
** Date created: 2004
** Date last edited: 20-04-2005

** Define Variables
**   Optional scaling factor (e.g. set to 0.001 if all geometrical
**   coordinates etc. are to be defined in mm instead of metres)
#scaling = 1e-3
**   Frequency and wavelength
#freq = 30e6          ** frequency in Hertz
#lam = #c0/#freq      ** wavelength in metre,  #c0 = speed of light in vacuum
#lam = #lam/#scaling  ** scale the wavelength as desired (e.g. to mm)

**   Other user defined variables
#csl=250              ** Total cross-sectional length
#hw=0.5               ** Heigth-width ratio
#w=#csl/(2*#hw+2)     ** Width
#h = #hw*#w           ** Height
#or = 200             ** Origin
#l = 1000             ** Length of tray
#dy1= 5               ** Height of pickup loop above tray floor
#dy=6
#t = 0.56             ** Thickness of metal(skin effect)
#fmin = 300e3         ** Minimum frequency (Start)
#fmax = 30e6          ** Maximum frequency (Stop)
#nf= 200              ** Number of frequency points
#sig = 1.45e7         ** Metal Conductivity
#wl=100               ** Injection wire length
```

```
** Parameters for segmentation
#seg_r = 1        ** radius of the wire segments
#seg_l = 1.5*#dy1  ** maximum length of wire segments
#tri_l = 2*#dy1    ** maximum edge length for triangular patches

#tL0 = min(#lam/30,#w/2)
#sL0 = #tL0
#tL1 = min(#lam/30,1.5*#dy1)
#sL1 = #tL1

IP                    #seg_r   #tL0     #sL0

** Geometry of radiating structure
** A FEMAP model may be included with the IN card
** IN  1  3  "filename.ext"

** Define points for cable tray structure
DP  CT1               0        #l/2     #or
DP  CT2               #w       #l/2     #or
DP  CT3               #w       -#l/2    #or
DP  CT4               0        -#l/2    #or
DP  CT5               0        #l/2     #or+#h
DP  CT6               #w       #l/2     #or+#h
DP  CT7               #w       -#l/2    #or+#h
DP  CT8               0        -#l/2    #or+#h
** DP  CT9                #w       -#l/2    #or+#dy
DP  CT10              #w       -#l/2    0
DP  CT11              0        -#l/2    0

** Define points for pickup loop
DP  PL1               0        #l/2-5   #or
DP  PL2               0        #l/2-5   #or+#dy
DP  PL3               0        -#l/2    #or+#dy

** Define point for plate with hole
DP  HC                0        -#l/2    #or+#dy
DP  HR                1.5      -#l/2    #or+#dy

** Define points for sources
DP  S1_1              0        #l/2+#wl  #or
DP  S1_2              0        #l/2+#wl  #or-#seg_l
DP  S1_3              0        #l/2+#wl  0
DP  S2_1              0        -#l/2+#sL1#or+#dy
DP  S2_2              0        -#l/2-8   0

LA  1
** Create Cable Tray Structure
** Bottom
PM  CT1  CT2  CT3  CT4      PL1
#tL1            #tL1     #tL1     #tL1
```

```
** Vertical side
PM  CT2  CT3  CT7  CT6
#tL1

** Plate to ground
PM  CT3  CT10 CT11 CT4
#tL1

** Vertical ends
PM  CT1  CT2  CT6  CT5
#tL1                  #tL1
** PM  CT8  CT7  CT9  CT3     CT4     PL3
#tL1    #tL1    #tL1    #tL1
PM  CT4  CT3  CT7  CT8     PL3
#tL1    #tL1           #tL1    #tL1

SY  1   3   0   0

** Create wire segment for source 1 (Port 1)
LA  2
BL  S1_2 S1_1

** Create wires used
LA  3
BL  S1_3 S1_2
IP                  #seg_r          #sL1
BL  S1_1 CT1

** Create Pickup Loop
LA  4
IP                  #seg_r          #sL1
BL  PL1  PL2
BL  PL2  S2_1

** Create wire segment for source 2 (Port 2)
LA  5
BL  PL3  S2_1

** Apply the scaling factor
SF  1               #scaling
** End of geometric input

EG  1   0   0   0   0

** Create a PEC (Perfect Electric Conducting) Ground Plane
BO  2               1       0       1       0       0

** Define skin effect for metal plate and wires
SK  1   3           #t      1       #sig
SK  2   3                   1       #sig
```

```
SK  3  3                    1       #sig
SK  4  3                    1       #sig
SK  5  3                    1       #sig

** Set the frequency point for simulation
FR  #nf 0               #fmin           #fmax

** Voltage gap excitation at a segment

**Source 1 (Port 1)
A1  0   2               1.58    0                       50

**Source 2 (Port 2)
A1  1   5               1.58    0                       50

** Format of output files
DA  0   0   0   0   0   1

** Extract S-parameters
SP                  50

** End
EN
```

C.3 S-parameter calculation (sidewall)

```
** This file attempts to simulate the S-parameters of a
** cable tray in order to determine it's shielding effectiveness
** SE. The height-width ratio can be changed according
** to specification.

** Creator of file: N.W.Ebertsohn
** Date created: 2004
** Date last edited: 20-04-2005

** Define Variables
** Optional scaling factor (e.g. set to 0.001 if all geometrical
** coordinates etc. are to be defined in mm instead of metres)
#scaling = 1e-3
** Frequency and wavelength
#freq = 30e6         ** frequency in Hertz
#lam = #c0/#freq     ** wavelength in metre,  #c0 = speed of light in vacuum
#lam = #lam/#scaling  ** scale the wavelength as desired (e.g. to mm)

** Other user defined variables
#csl=250            ** Total cross-sectional length
#hw=1           ** Heigth-width ratio
#w=#csl/(2*#hw+2)    ** Width
#h = #hw*#w         ** Height
```

```
#or = 200          ** Origin
#l = 1000          ** Length of tray
#ly = 10
#dy1= 3            ** Height of pickup loop above tray floor
#dy=25
#t = 0.56          ** Thickness of metal(skin effect)
#fmin = 300e3      ** Minimum frequency (Start)
#fmax = 30e6       ** Maximum frequency (Stop)
#nf= 200           ** Number of frequency points
#sig = 1.45e7      ** Metal Conductivity
#wl=100            ** Injection wire length

** Parameters for segmentation
#seg_r = 1        ** radius of the wire segments
#seg_l = 1.5*#dy1  ** maximum length of wire segments
#tri_l = 2*#dy1    ** maximum edge length for triangular patches

#tL0 = min(#lam/30,#w/2)
#sL0 = 20.83333
#tL1 = min(#lam/30,1.5*#dy1)
#sL1 = 7.5

IP                  #seg_r   #tL0     #sL0

** Geometry of radiating structure
** A FEMAP model may be included with the IN card
** IN   1  3  "filename.ext"

** Define points for cable tray structure
DP  CT1             #w      #l/2     #or
DP  CT2             #w-#ly   #l/2     #or
DP  CT3             -#w     #l/2     #or
DP  CT4             -#w     -#l/2    #or
DP  CT5             #w-#ly   -#l/2    #or
DP  CT6             #w      -#l/2    #or
DP  CT7             #w      #l/2     #or+#h
DP  CT8             -#w     #l/2     #or+#h
DP  CT9             -#w     -#l/2    #or+#h
DP  CT10            #w      -#l/2    #or+#h

** Define points for pickup loop
DP  PL1             #w-#ly   #l/2-5   #or
DP  PL2             #w-#ly   #l/2-5   #or+#dy
DP  PL3             #w-#ly   -#l/2+5  #or+#dy
DP  PL4             #w-#ly   -#l/2    #or+#dy

** Define points for injection wire
DP  S1              0       #l/2+100  0
DP  S2              0       #l/2+100  #or-5
DP  S3              0       #l/2+100  #or
```

```
DP  S4              0       #l/2    #or
** Define points for return conductor
DP  G1              #w      -#l/2   0
DP  G2              -#w     -#l/2   0

LA  1
** Create Cable Tray Structure
** Bottom
PM  CT1 CT2 PL1 CT5     CT6
#tL1    #tL1    #tL1    #tL1    #tL1
PM  CT2 S4  CT3 CT4     CT5     PL1
#tL1    #tL1

** Vertical sides
PM  CT1 CT6 CT10 CT7
#tL1
PM  CT3 CT4 CT9 CT8

** Plate to ground
PM  G1  G2  CT4 CT5     CT6
#tL1

** Vertical ends
PM  CT1 CT2 S4  CT3     CT8     CT7
#tL1
PM  CT6 CT5 CT4 CT9 1   CT10
#tL1
   PL4

IP              #seg_r          #sL1
** Create wire segment for source 1 (Port 1)
LA  2
BL  S2  S3

** Create wires
LA  3
BL  S3  S4
BL  S1  S2

** Create Pickup Loop
LA  4
IP              #seg_r          #sL1
BL  PL1 PL2
BL  PL2 PL3

** Create wire segment for source 2 (Port 2)
LA  5
BL  PL4 PL3

** Apply the scaling factor
```

```
SF  1                   #scaling
** End of geometric input
EG  1   0   0   0   0

** Create a PEC (Perfect Electric Conducting) Ground Plane
BO  2                   1       0       1       0       0

** Define skin effect for metal plate and wires
SK  1   3               #t      1       #sig
SK  2   3                       1       #sig
SK  3   3                       1       #sig
SK  4   3                       1       #sig
SK  5   3                       1       #sig

** Set the frequency point for simulation
FR  #nf 0               #fmin           #fmax

** Optional loading of segments
** LS  5                 50      0       0
** LS  2                 50      0       0

** Voltage gap excitation at a segment

**Source 1 (Port 1)
A1  0   2               1.58    0                       50

**Source 2 (Port 2)
A1  1   5               1.58    0                       50

** Format of output files
DA  0   0   0   0   0   1

** Extract S-parameters
SP                      50

** End
EN
```

Appendix D

Magnetic Field Line Plots

D.1 Magnetic field calculation for h/w = 1/2

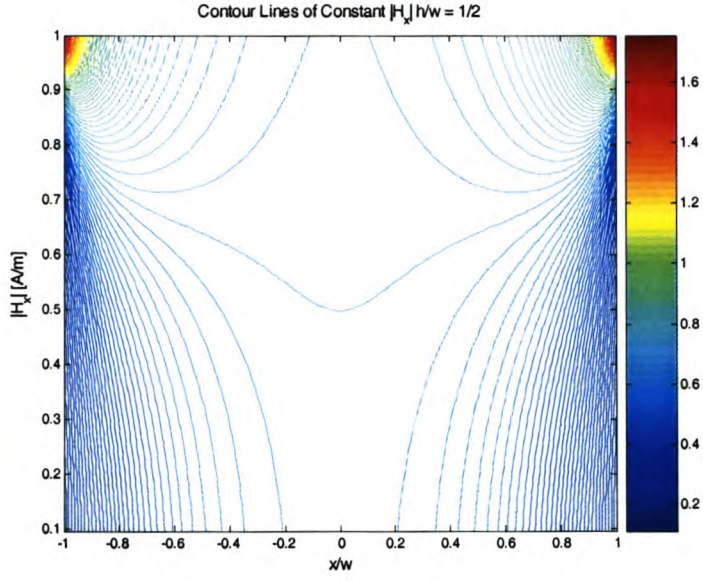

Figure D.1: *Plot of simulated $|H_x|$ of tray with h/w = 1/2*

D.2 Magnetic field calculation for h/w = 1

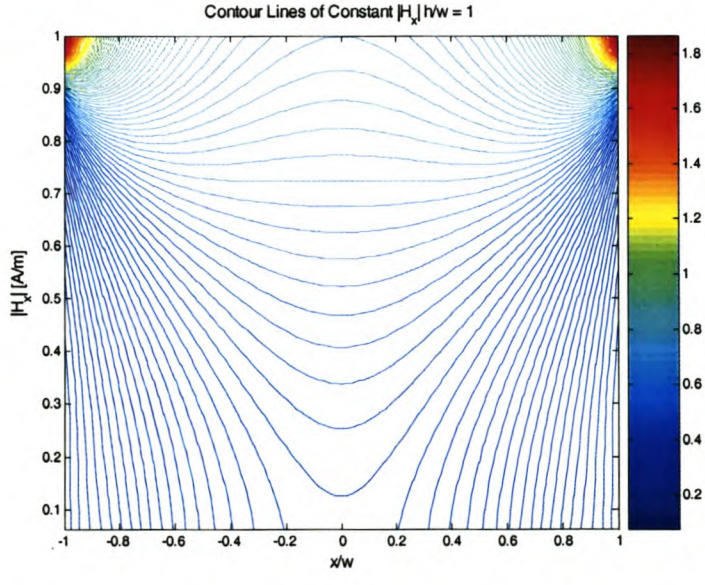

Figure D.2: *Plot of simulated $|H_x|$ of tray with h/w = 1*

D.3 Magnetic field calculation for h/w = 3/2

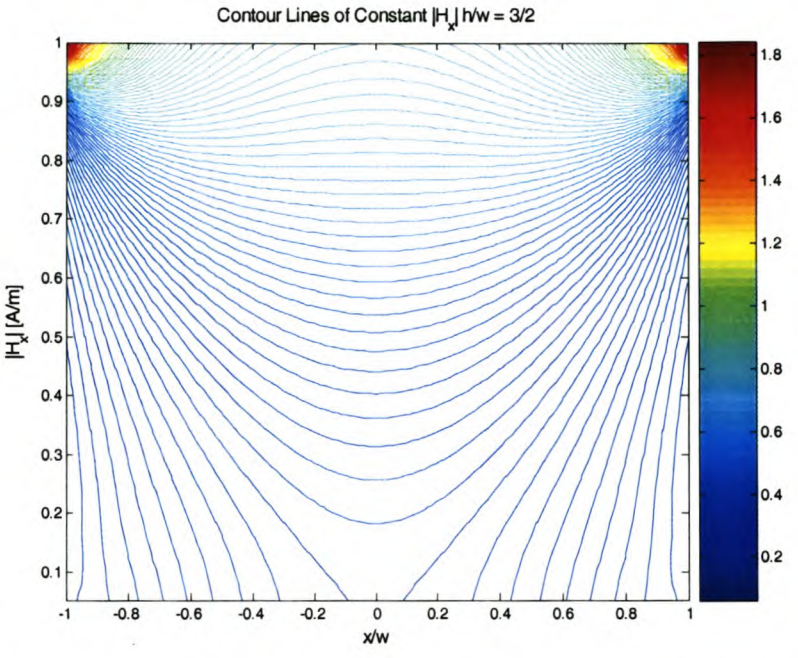

Figure D.3: *Plot of simulated $|H_x|$ of tray with h/w = 3/2*

D.4 Magnetic field calculation for h/w = 2

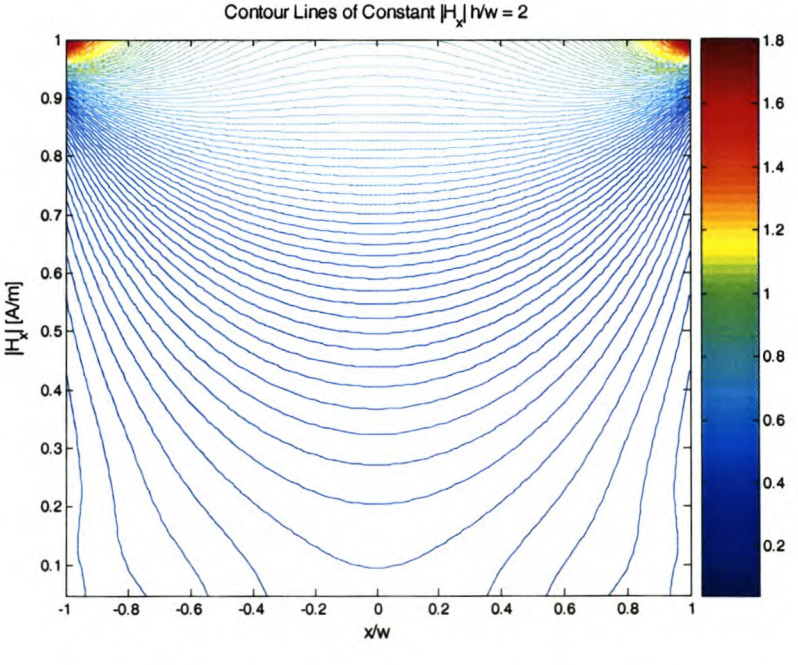

Figure D.4: *Plot of simulated $|H_x|$ of tray with h/w = 2*

Appendix E

Measured and Simulated Data

E.1 $|Z_t|$ at point A

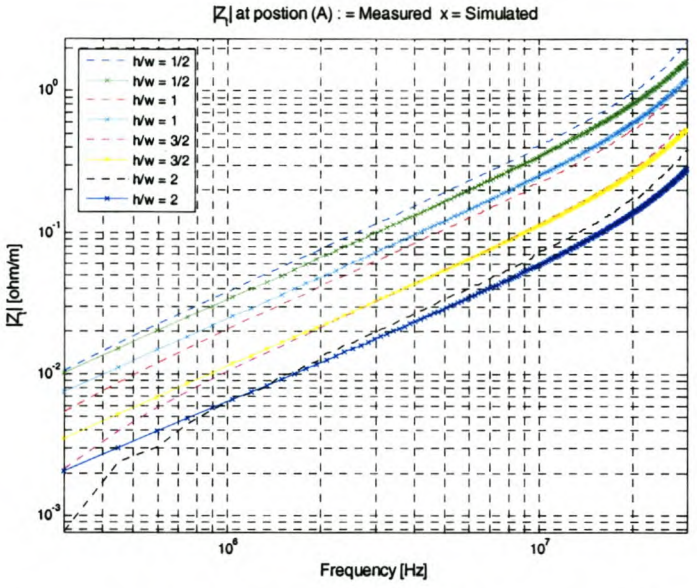

Figure E.1: *Plot of measured and simulated $|Z_t|$ at point A for the four trays*

E.2 $|Z_t|$ at point B

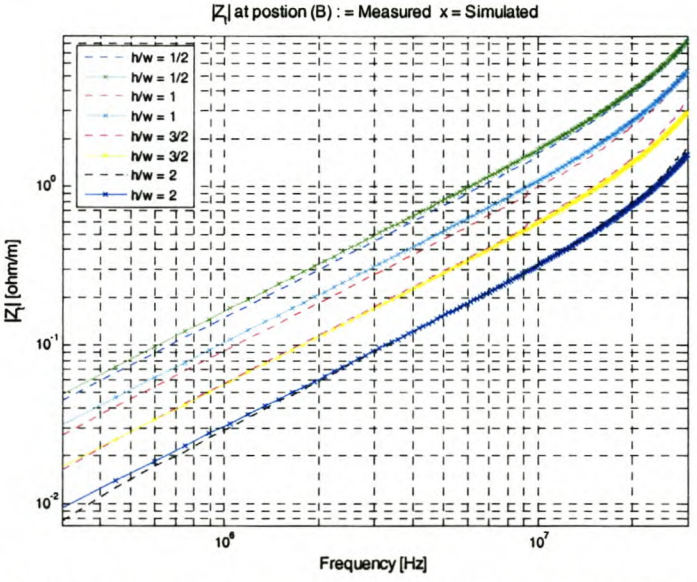

Figure E.2: *Plot of measured and simulated $|Z_t|$ at point B for the four trays*

E.3 $|Z_t|$ at point C

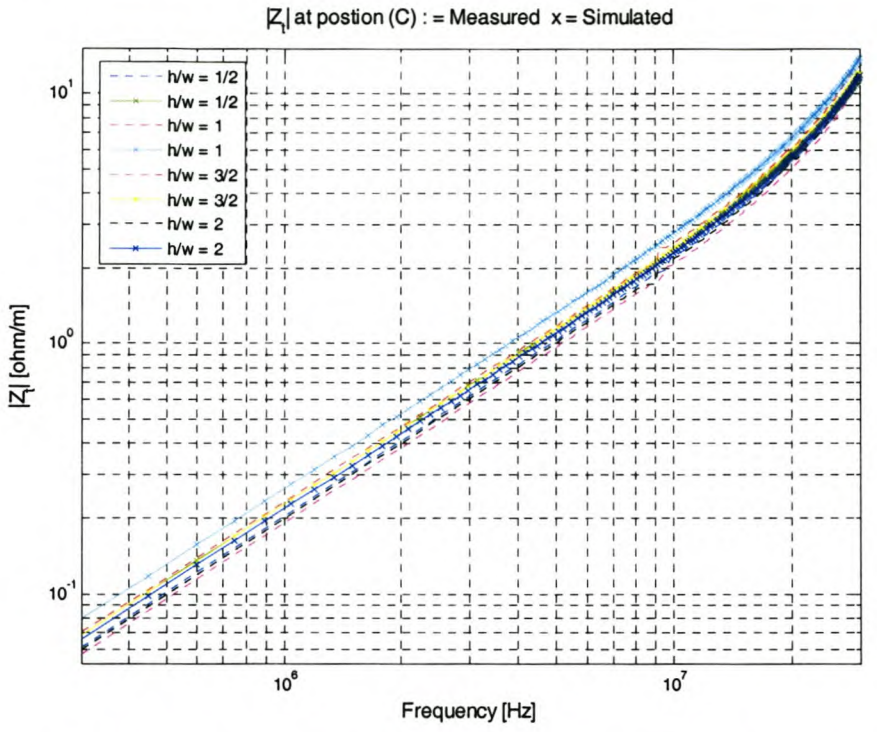

Figure E.3: *Plot of measured and simulated $|Z_t|$ at point C for the four trays*

E.4 $|Z_t|$ at point D

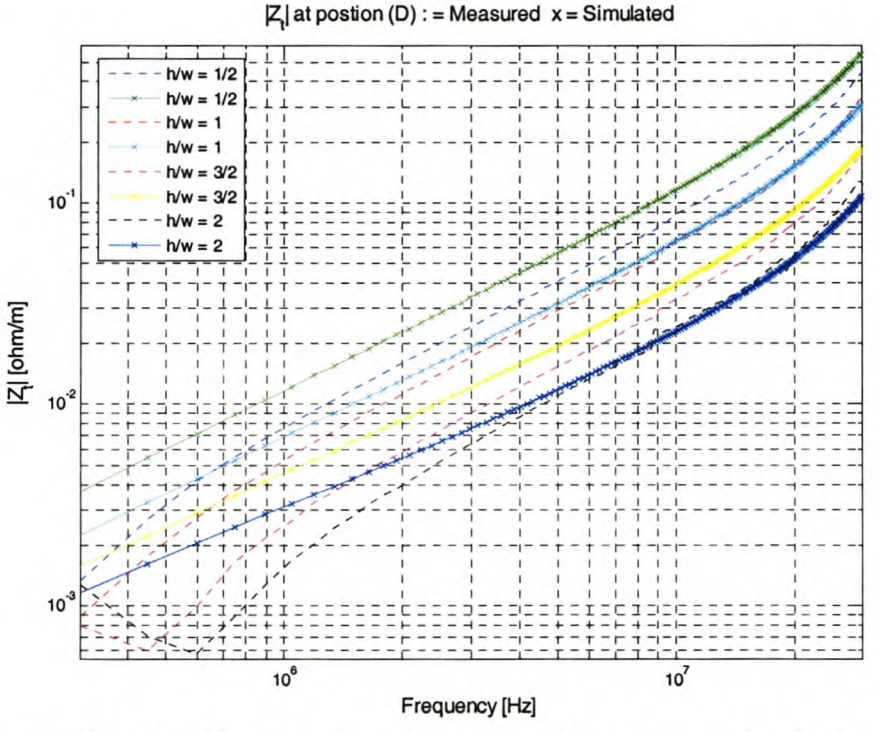

Figure E.4: *Plot of measured and simulated $|Z_t|$ at point D for the four trays*

E.5 $|Z_t|$ at point E

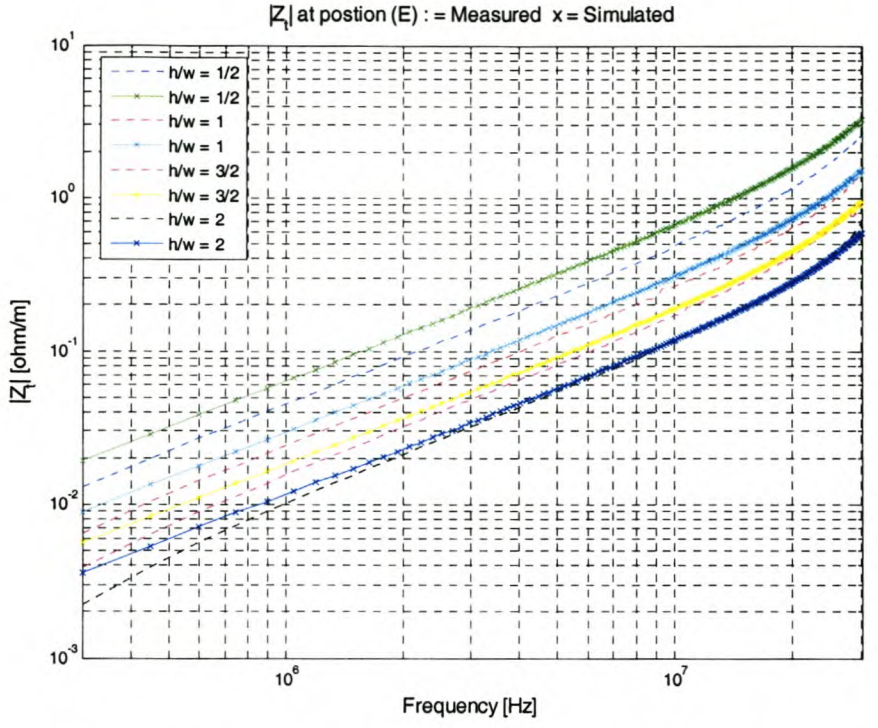

Figure E.5: *Plot of measured and simulated $|Z_t|$ at point E for the four trays*

E.6 $|Z_t|$ at point F

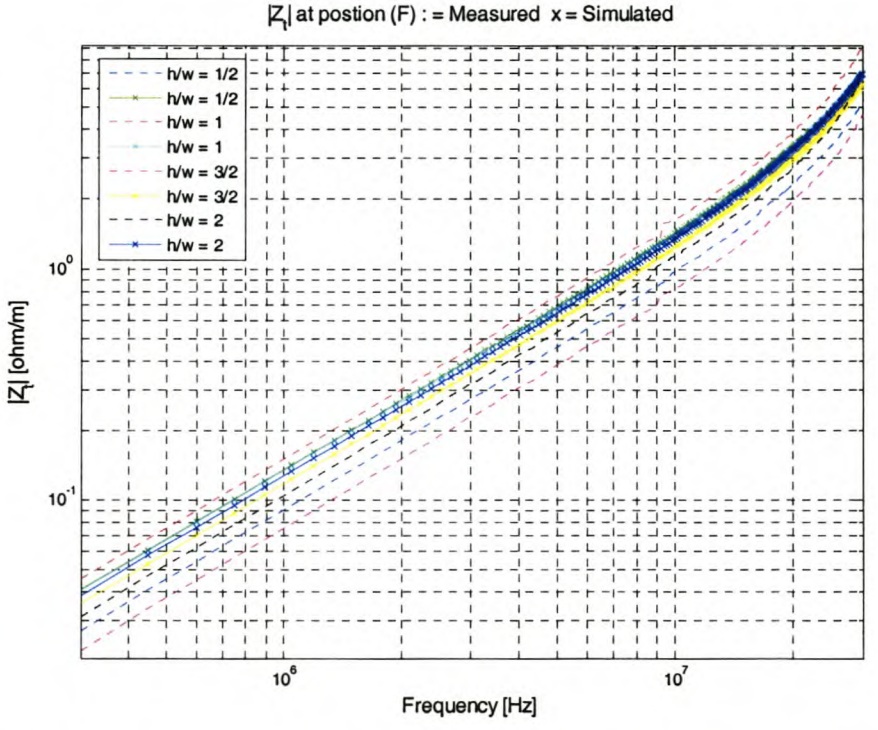

Figure E.6: *Plot of measured and simulated $|Z_t|$ at point F for the four trays*